Isabel Hanghofer, BSc

Investigation of the Forming Reaction of (Ba,Ca)(Zr,Ti)O3 Ceramics

MASTER'S THESIS

to achieve the university degree of

Diplom-Ingenieurin

Master's degree programme: Technical Chemistry

submitted to

Graz University of Technology

Supervisor

Ao.Univ.-Prof. Dipl.-Ing. Dr.techn. Klaus Reichmann

Institute for Chemistry and Technology of Materials

Graz, August 2016

EIDESSTATTLICHE ERKLÄRUNG

Ich erkläre an Eides statt, dass ich die vorliegende Arbeit selbstständig verfasst, andere als die angegebenen Quellen/Hilfsmittel nicht benutzt und die den benutzten Quellen wörtlich und inhaltlich entnommene Stellen als solche kenntlich gemacht habe.

Graz, am …………………………… ………………………………………………..

(Unterschrift)

STATUTORY DECLARATION

I declare that I have authored this thesis independently, that I have not used other than the declared sources / resources, and that I have explicitly marked all material which has been quoted either literally or by content from the used sources.

…………………………… ………………………………………………..

date (signature)

Kurzfassung

Diese Arbeit beinhaltet beinhaltet die Untersuchung der Bildungsreaktion von $(Ba_xCa_{1-x})(Zr_yTi_{1-y})O_3$ [BCZT] Keramiken. Sie werden als alternatives System zu den bekannten Blei Zirkonat Titanat (PZT) Verbindungen eingesetzt, die aufgrund der hohen relativen Permittivität für verschiedene elektronische Bauelemente, insbesondere Vielschichtkondensatoren, eingesetzt werden.

Um den Reaktionsverlauf bei der Herstellung dieser Verbindung durch die Mischoxidmethode besser zu verstehen, werden die Ausgangsstoffe gemischt und mittels simultaner Thermoanalyse gekoppelt mit einem Massenspektrometer (STA-MS) und Hochtemperatur-Röntgendiffraktometrie (HT-XRD) untersucht.
Die STA-MS gibt Einblick in den Ablauf der Bildungsreaktion. Mit HT-XRD können Zwischenverbindungen identifiziert werden.

Die chemische Zusammensetzung sowie die elektrischen Eigenschaften der gesinterten Proben werden durch folgende Charakterisierungsmethoden genauer untersucht: Röngtendiffraktometrie, Hochtemperatur XRD und Impedanzspektroskopie. Anhand des Phasendiagramms werden die Zusammensetzungen der Proben ausgewählt und hinsichtlich der elektrischen Eigenschaften und der Struktur verglichen. Der Schwerpunkt der Arbeit liegt darauf die Bildungsreaktion zu verfolgen und die Homogenität des Materials zu überprüfen.

Während der Bildungsreaktion kann beobachtet werden, dass Zr^{4+} und Ca^{2+} in das $BaTiO_3$ Gitter, welches als Wirt fungiert, hinein diffundieren. Alle untersuchten Materialien weisen eine Perowskit-Struktur auf, die über verschiedene Zwischenphasen gebildet wird. Außerdem spielen die Ionenradien der einzelnen Komponenten und die Aufheizrate in der Thermoanalyse eine wichtige Rolle im Reaktionsmechanismus.

Abstract

This work contains the study of the formation reaction of $(Ba_xCa_{1-x})(Zr_yTi_{1-y})O_3$ [BCZT] ceramics. They indicate an alternative system to the well-known lead zirconate titanate (PZT) systems. Due to their good piezoelectric properties for different electronic devices, especially multilayer ceramic capacitors (MLCC).

To understand the reaction better, the starting materials are mixed via mixed oxide route and are analyzed by simultaneous thermal analysis coupled with a mass spectrometry (STA-MS) and high temperature x-ray diffraction (HT-XRD).
The STA- MS gives insight into the process of the formation reaction and with the HT-XRD intermediate compounds can be identified.

By using common characterization methods like X-ray diffraction, high temperature XRD and impedance spectroscopy, the chemical composition and the electric properties are examined. The samples are selected from the phase diagram and are compared in terms of electric properties and structure. Moreover, the focus is on the pathway of the forming reaction mechanism and the homogeneity of the material.

During the forming reaction it can be observed, that Zr^{4+} and Ca^{2+} diffuse into the $BaTiO_3$ lattice that operates as the host. All studied materials exhibit a perovskite structure which is formed through different intermediate phases. The heating rate of the thermal analysis and the ionic radii of the compounds constitute an important role in the reaction mechanism.

Acknowledgment

I would like to express my deep gratitude to all who helped me completing this work and who accompanied me during my studies.

At first, I thank Mr. Ao. Univ.-Prof. Dipl.-Ing Dr. Klaus Reichmann for supervising my master thesis, for many helpful advices and for supporting me with his excellent knowledge.

My gratitude also goes to Brigitte Bitschnau for recording the XRD measurements and for many useful conversations in terms of XRD analysis. Furthermore, I thank the EPCOS OHG for the high temperature XRD and the dielectric measurement.

Of course I want to thank my colleagues, especially Sarah, Patrick, Lisi and Mathias, for assisting me in every need and for spending many pleasurable hours together. Special thanks go to Marlene, Katharina, Carina, Benedikt, Richard, Carmen and Karin for always having a friendly ear.

I express my honest gratitude to Michael for being at my side all the time. Thank you for your support, your loving attention and for keeping up your good spirits even during stressful time.

My sincere thank is owed to my family for being with me and helping me all the time and for their special care in every life situation. Thank you for your faith and trust in me and for the love I received.

Table of contents

1 Introduction

Ferroelectric materials with perovskite type structure (ABO_3) have been studied extensively, because of their broad technical application in memory storage devices, multilayer ceramic capacitors (MLCC) and piezoelctric devices. Since the 20th century $BaTiO_3$ gained interest due to environmental and fundamental studies.[2] $Ba(Zr,Ti)O_3$ was considered as an important material for ceramic capacitors, because Zr^{4+} is chemically more stable than Ti^{4+}.[3]

Lead-free materials like $BaTiO_3$ or $(Ba,Ca)(Zr,Ti)O_3$ often show inferior properties compared to doped PZT but with the RoHS-directive in place, these materials get more and more popular in the scientific community. [4]

$BaTiO_3$ itself shows a high dielectric constant with a sharp maximum at about 130°C. With proper dopants this maximum can be depressed and shifted resulting in a stable dielectric over a wide temperature range. Solid solution of $BaTiO_3$ doped with Zr^{4+} and/or Ca^{2+} offer a higher relative permittivity but in a narrower temperature range. So $Ba(Zr,Ti)O_3$ systems have been established as one of the most important compositions for MLCC. Puli et al and Bera et al reported that the perovskite structure of $(Ba,Ca)(Zr,Ti)O_3$ ceramics is formed without any secondary phases. [5,6]

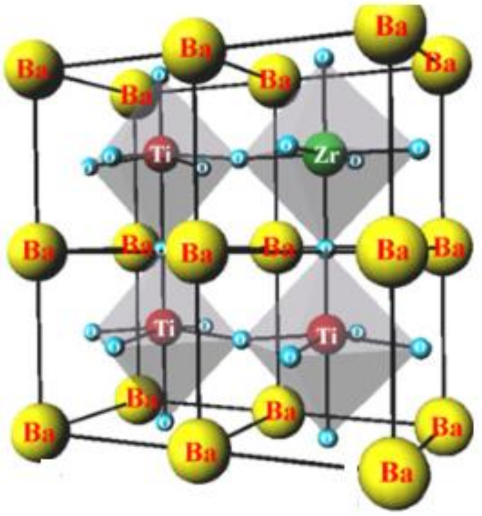

Figure 1: Schematic of a perovskite structure of a $Ba(Zr,Ti)O_3$ ceramic.[1]

The aim of this thesis is to follow the solid state reaction via thermal analysis and high temperature XRD and to find out, which intermediate phases are formed during processing. Furthermore, the relaxor behavior and the diffuse phase transition are characterized through dielectric measurement.

This work comprises the preparation – via the mixed oxide route – and characterization of Zr^{4+} doped $BaTiO_3$ and Ca^{2+}, Zr^{4+} doped $BaTiO_3$. The focus is on the forming reaction mechanism and therefore the structural formation of $Ba(Zr,Ti)O_3$ and $(Ba,Ca)(Zr,Ti)O_3$. It can be can be shown by dielectric measurments, that the materials show a relaxor ferroelectricity.In contrast to literature, it can be shown that the prepared ceramics are formed through intermediate phases.

For this work, first a literature survey was done in order to gain an overview of lead free ceramics and possible preparation methods. Secondly the ceramics were prepared and the structural properties and dielectric characteristics were discussed in a detailed way.

2 General Aspects

In the following chapter an overview is given why (Ba,Ca)(Zr,Ti)O_3 materials are so important. Polar oxide materials with perovskite structure, having a general formula ABO_3, gain importance for the ferroelectric components. These materials are found in a widespread area of applications: high dielectric constant capacitor, stereo tweets, buzzers, positive temperature coefficient resistors (PTC) thin film capacitors, ferroelectric thin-film memories and many more.[2,7]

2.1 Crystal Classes

Crystal systems are classified in 32 point groups which are divided in 7 basic crystal systems. These systems are called: hexagonal, orthorhombic, triclinic, tetragonal, rhombohedral, monoclinic and cubic. Furthermore, they are split into 11 centrosymmetric and 21 non-centrosymmetric groups. These non-centrosymmetric point groups do not contain any inversion centre and 20 of them exhibit piezoelectricity, that is the occurrence of polarization on mechanical stress.

There are of these non-centrosymmetric point groups, which exhibit a permanent polar axis along a certain lattice direction. Their polarization changes with the temperature and is therefore called pyroelectric. A typical pyroelectric material is wurtzite β-ZnS. A well-known subgroup of the pyroelectric materials are ferroelectric materials.

Like pyroelectrics, ferroelectrics also possess a polar axis, but in this case the polarization can be orientated through an applied electric field. As seen in the figure below the ferroelectrics are a subgroup of pyroelectrics and piezoelectrics. [8,9,2]

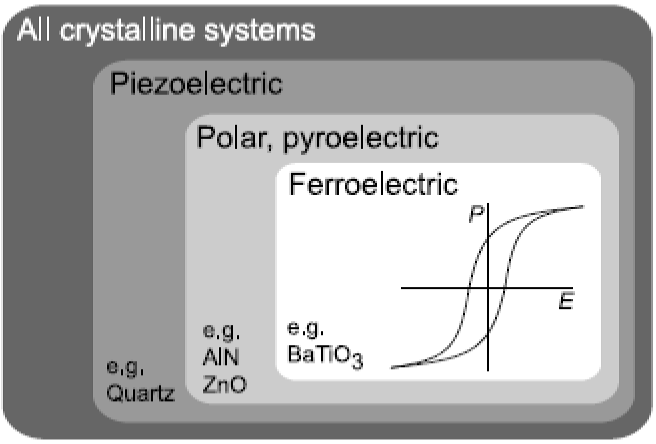

Figure 2: Electric properties of the different crystal classes.[8]

Plotting the polarization of a ferroelectric versus electric field yields a hysteresis loop (see inset in Figure 2). Additionally, the hysteresis loop visualizes that the spontaneous polarization can be reversed by an applied electric electric field exceeding the so called coercive field..[10]

2.1.1 Perovskite Crystal Structure

Most of the ferroelectrics, lead titanate ($PbTiO_3$), lead zirconate titanate (PZT), potassium niobate ($KNbO_3$) and epically barium titanate ($BaTiO_3$) have the well-known perovskite structure. The structure is named after the mineral $CaTiO_3$.[2]

It is a simple cubic structure (space group: Fm3m) which consists of the ABO_3 formula.[11] The unit cell with the B-cation in the center is shown in Figure 3.[2,10,8]

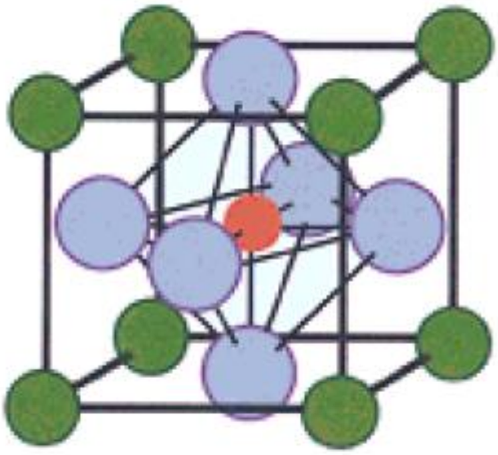

Figure 3: Perovskite ABO_3 unit cell for $BaTiO_3$. The A- site is Ba^{2+}(green), the B-site in the center is Ti^{4+} (red) and O^{2-}(blue). [2]

As Johnsonn et al reported, by such octahedral units the coordinated ion at the body centre of the unit cell and in the center of the cube eight such octahedral units, the perovskite structure is formed. [11]

In a cubic cell the cell constant a depends on the ionic radii r_A, r_B and r_0 as expressed in Equation 1.[11]

$$a = \sqrt{2}(r_A + r_0) = 2(r_B + r_0)$$

Equation 1: Ratio of A-site and B-site ion in a cubic perovskite crystal. (r_A... ion radius of the A-site, r_B...ion radius of the B-site ion, r_0.... Ion radius of the oxygen atom). [11]

Any distortion of the lattice is described by the ratio of A and B cell length is called the Goldschmidt tolerance factor t. If the factor is decreasing, it means that the size of the cation will be decreased.[11,9] The Goldschmidt factor has a typical value between $0.89 < t < 1.10$.

In Equation 2 the formula for the Goldschmidt tolerance factor is shown.

$$t = \frac{(r_A + r_0)}{\sqrt{2}(r_B + r_0)}$$

Equation 2: Goldschmidt tolerance factor t.[11]

PMN, BZT and BCZT show a complexity in their perovskite structure due to the relaxor behavior which will be discussed in later chapters.

2.2 Electric and Dielectric Properties

The properties of ferroelectric materials – polarization and strain – are described through physical models. [12]

The dielectric displacement *D* in an external field *E* is described by Equation 3 containing the permittivity of the vacuum and the external field is described by an external applied field $\varepsilon_0\vec{E}$ and by the electrical polarization $\vec{P}$. [8]

$$\vec{D} = \varepsilon_0\vec{E} \cdot \vec{P}$$

Equation 3: Charge neutrality. ($\varepsilon_0\vec{E}$… applied electric field, $\vec{P}$… polarization).[8]

The Equation 3 is independent of the polarization mechanisms, so it makes no difference if it is a pyroelectric, piezoelectric or dielectric polarization.[8,13]

As an example a simple plate capacitor is taken. It has to be distinguished between

1. Constant charges
2. Constant voltage

If the charges are constant (*D*=const.) it is called an open circuit condition and if the applied voltage is constant (*E*=const.) it is called short circuit condition. This difference is shown in Figure 4.[8]

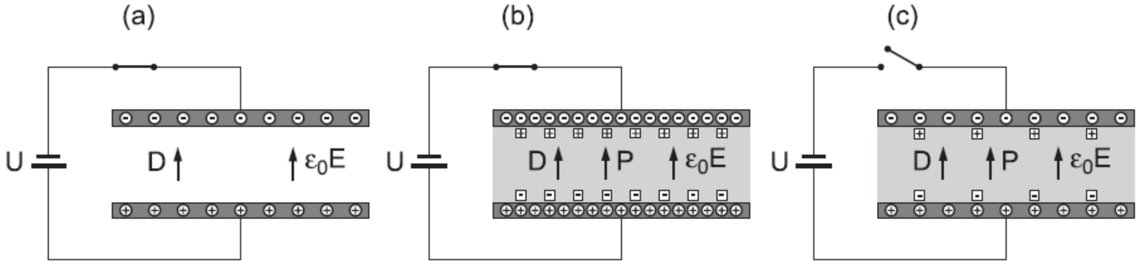

Figure 4: Displays a parallel plate capacitor. (a) without any dielectric; (b) *E*=const which indicates a short circuit condition; (c) *D*=const. which indicates a short circuit condition. [8]

Additionally, the pure dielectric response describes the proportionality of the polarization to the electric field. [8,12]

$$\vec{P} = \varepsilon_0 \cdot \chi \cdot \vec{E} \qquad \text{or} \qquad \vec{D} = \varepsilon_0 \cdot \varepsilon_r \cdot \vec{E}$$

Equation 4: Pure dielectric response. (ε_0… dielectric constant, χ… susceptibility, ε_r..relative dielectric constant)[8]

Another important factor is the susceptibility χ which is related to the relative dielectric constant ε_r. The coherence between the relative dielectric constant and the susceptibility is: $\chi = \varepsilon_r - 1$.[8,12,14]

To sum up, Equation 3 and Equation 4 describe the dielectric properties. The sum of the dipole moments result in the polarization which describes the permittivity and the capacity of a structural component with defined geometry.[8,14]

$$P = \sum_j N_j \cdot p_j$$

Equation 5: Polarization *P*. (*N_j*… densitiy of the material, *p_j*… dipolmoment).[8]

The relation between the atomic polarizability *α* and the permittivity *ε* is the Clausius-Mossotti equation. This equation is mainly used for structures with cubic structure and induced dipoles.

$$\varepsilon = \frac{\varepsilon_0 + 2N_j\alpha_j}{\varepsilon_0 - N_j\alpha_j}$$

Equation 6: Clausius-Mosotti equation. [8]

The specific conductivity is described through the loss factor *tanδ* which has also a key role in the dielectric measurement. In the circuit conductivity represented by ohmic resistor, which trigger the thermal loss. The loss factor needs to be minimized to avoid capacity changes due to temperature changes. The strain of the material is an important factor because it also influences the capacity due to geometry changes. [12]

The coherence between susceptibility and relative permittivity (Equation 4 and Equation 5) and the geometry of the building component leads to the capacity.

$$C = \varepsilon_0 \cdot \varepsilon_r \cdot \frac{A}{d} \cdot (n-1)$$

Equation 7: Capacity of a plate capacitor. (*A*… area of the capacitor, *d*…thickness of the capacitor, *n*… number of electrods (within a plate capacitor the *n-1* term is negligible).[12]

Real capacitors are always defective due to the leakage currents in the dielectric material. The dielectric losses cause the heating of the capacitor. Furthermore, the equivalent circuit diagram is shown in the figure below. [12]

$$i = i_C + i_R = j\omega \cdot C \cdot u \cdot \frac{1}{R} u$$

Equation 8: Description of a real capacitor *C* through the resistance *R* and the capacitive current i_C and the ohmic load i_R.[12]

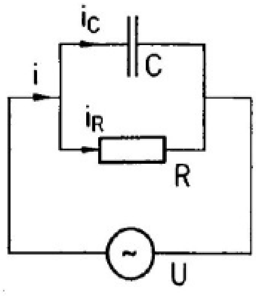

Figure 5: Equivalent circuit diagram of a real capacitor. [12]

The loss factor *tanδ* is described by the ratio between the real and the imaginary part of the current. [12]

$$tan\delta = \frac{|i_R|}{|i_C|} = \frac{1}{\omega \cdot R \cdot C}$$

Equation 9: Loss factor described by the resistor *R*, the capacity *C* and the circular frequency *ω*. [12]

2.2.1 Mechanisms of Polarization

In this chapter, the four different mechanisms of polarization are discussed. The three basic types are electronic, ionic and orientation polarization. All, including the space charge polarization, can be explained through their intrinsic contribution. [8,12]

- **Electronic Polarization**

  This kind of polarization is found in all dielectric materials. When an electric field is applied, the core (positive charged) and the shell (negative charged) shift in the opposite direction of the material. Additionally, the polarizability *α* is proportional to the volume of the shell. Therefore, with increasing atom size the electronic polarization is also increasing. [12,8]

Figure 6: Electronic polarization, which shows the displacement of core and shell.[12]

- **Ionic Polarization**

  As the name says, it occurs in ionic materials. It appears when an electric field is applied and the cations and anions are displaced in the opposite direction. These materials increase the net dipole moment. [8]

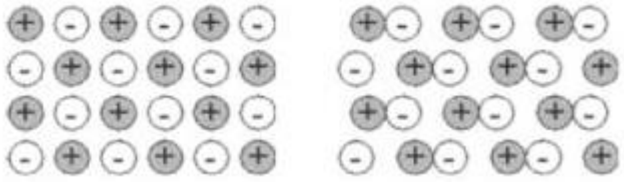

Figure 7: Ionic polarization, which displays the displacement of cations and anions by an induced dipole. Left: E=0 and right E>0. [12]

- **Orientation Polarization**

  A permanent dipole is either induced or permanently present due to a separation of positive and negative charges in a molecule (e.g. H_2O) or a unit cell in a crystalline solid. In absence of an external electric field, the dipole moments are orientated randomly as seen in Figure 8 (left). Applying an electric field, the dipoles orient in the same direction. The thermal movement disturbs the conformation. [8]

Figure 8: Orientation polarization, which visualizes the displacement of permanent dipoles. Left: E=0 and right E>0. [12]

- **Space charged Polarization**

  The diffusion of ions or electrons along the field direction results in a separation of charges. Space charged polarization exists in dielectric materials which show inhomogeneities in their conductivity. They occur in ceramics which show electrically conducting grains and insulating grain boundaries. [8]

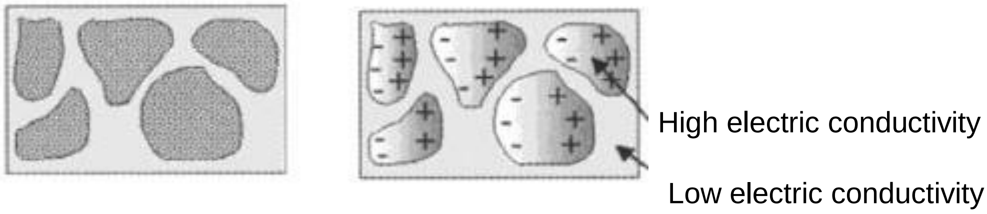

Figure 9: Orientation polarization, which show the collection of free charge carriers at the grain boundary. Left: E=0 and right E>0. [12]

The total polarization of the materials combines all types discussed above. [8]

Electronic and ionic polarization are called intrinsic because the contribution comes from the lattice, whereas space charged and orientation polarization are extrinsic. The sum of intrinsic and extrinsic contributions describes the total polarizability α. The total polarizability contains the space charge polarizability α_s, the orientation polarizability α_O, the ionic polarizability α_i and the electronic polarizability α_e.[8]

$$\alpha = \underbrace{\alpha_s + \alpha_O}_{\text{extrinsic}} + \underbrace{\alpha_i + \alpha_e}_{\text{intrinsic}}$$

Equation 10: Formula of the sum of extrinsic and intrinsic polarizability.[14]

Each polarization has a different relaxation time which is related to the frequency of the applied frequency external electric field. In Figure 10 the dispersion of the dielectric is shown. Resonance effects are shown in the electronic and ionic polarization and a relaxation behavior is found in the other types. [8]

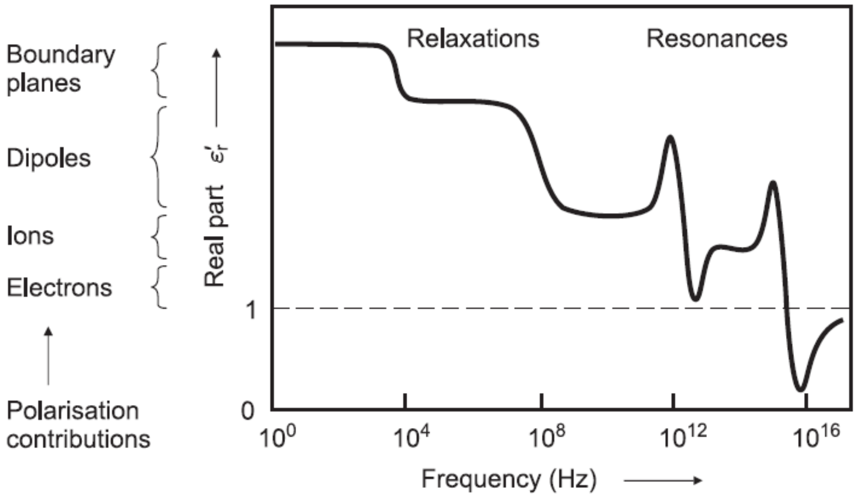

Figure 10: Frequency dependence of the relative permittivity in caused by different polarization types. [8]

2.3 Characteristics of Ferroelectric Materials

As mentioned in Chapter 2 ferroelectricity is the effect of spontaneous polarization, which can be reversed by application of an electric field. [15,8]

2.3.1 History of Ferroelectric Materials

The discovery of the ferroelectricity is leading back to the last century and is the work of the physics, Weiss, Pasteur, Pockels, Hooke, Groth, Voigt and the Curie brothers.[16]
The intensive study of ferroelectrics starts with the Rochelle salt and potassium hydrogen phosphate which are two water soluble crystals. Rochelle salt is a material which has excellent optical quality due to the large single crystals which grow rapidly. [2,16]

The study was going on quickly during the second world war with the discovery and investigation of barium titanate.[16] Between 1940 and 1950 there has been a continuous succession of materials and technology.[2] The initial reports of $BaTiO_3$ results from studies of

TiO_2 and BaO, which show ceramic materials with high dielectric permittivities. Thurnaurer and Deaderick created mixed oxides already in 1941.[17] Wainer and Solomon reported that the dielectric constants are increasing up to 1000, which is greater than for other ceramics. So they started working precisely on $BaTiO_3$. Also Vul and Goldmann started to report more detailed studies.[18] In 1945 Megaw pointed out that at room temperature a tetragonal structure is obtained and converts to a cubic structure at 120°C.[19] Also the dielectric loss or the relative permittivity ε_r versus the temperature show the phase transition which has been reported by von Hippel.[20] Four years later (1949) other phase transitions from tetragonal to orthorhombic or from orthorhombic to rhombohedral structure were reported.[21] However, at the end of the World War II $BaTiO_3$ became more interesting for academics and also for the industry due to the small volume and high capacitance. The capacitor technology uses such ceramic materials. [16]

In the next periode, 1950 to 1960, 100 new ferroelectrics were accrued, including lead zirconate titanate. Over this period, the number of known three to four perovskite ferroelectric was increasing to 25 known perovskite ferroelectrics. 1960 to 1970 is also called the age of high science or age of diversification due to the exploration of defect chemistry, the electrooptic properties and electronic conduction. In the next years, the electroceramics are getting more and more integrated in multilayer packages and ceramic resistors. [16,2]

Present markets show that the future for such materials is bright and is getting brighter over the years. The aim is to create smart and very smart materials which can be used either in electroceramics or the semiconductor industry. An example for smart types are piezoelectric ceramics and for very smart types electrostrictive relaxors. Hence, the key concept is to fabricate multifunctional materials with all creativity that engineers can raise. [2]

Therefore, the Zr^{4+} doped $BaTiO_3$ gains attention due to the high dielectric constant at low temperatures and it exhibits a relaxor behavior.[22]

2.3.2 Ferroelectric Polarization

As mentioned in Chapter 2.3.1, in 1921 ferroelectricity was discovered by Valasek.[23] The arrangement of the polar axis is static. A spontaneous polarization caused by spontaneous deformation is accompanied by internal mechanical stresses. The grain boundary prevents the free expansion for each individual grain. To reduce the elastic stresses, regions with different orientations are formed and are called domains. The angle between the orientations shows different values due to the crystal structure. The important domains for tetragonal structures are the so called 90° domains whereas the 180° domains are located in all phases. [24]

Because of the domain wall movement or 180° polarization jumps an alignment of the domain polarization in the direction of the applied field appears. The ferroelastic effect refers to the interaction of the domains with an applied mechanical field. Non 180° domains are increasing under pressure whereas 180° domains increase under stress. [24]

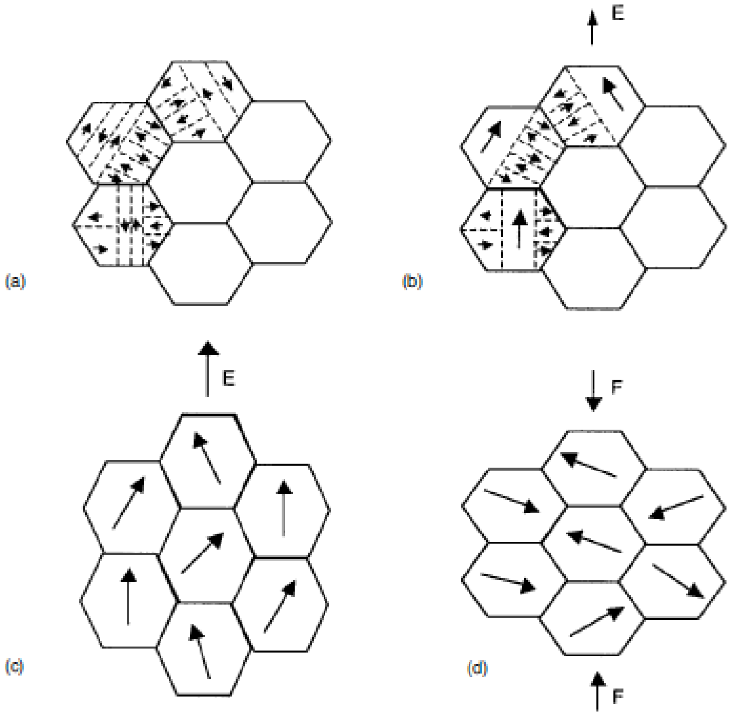

Figure 11: Schematic illustration of the application of the electrical and mechanical stress of a polycrystalline ceramic. (a) stress free; each grain is non polar and the domains get cancelled (b) applied electric field; 180° domains switch producing a net overall polarity but no changing in dimensionality (c) with increase in electric field and (d) with disorientation.[24]

The changes of domain structures are visible in the hysteresis loop if a high electric field is applied. [24,12]

2.3.2.1 Hysteresis Loop

The ferroelectric hysteresis loop is shaped in analogy to the similar magnetic loop *M-H* (magnetization vs magnetic field) obtained from a ferroelectric material. The standard form is the *P-E* loop (polarization vs electric field) which has a symmetric order. Due to the symmetric loop the remnant polarization and the coercive field can be easily determined. [25]

The most effective tool to understand ferroelectricity is the *P-E* hysteresis loop.[26] In principle a ferroelectric material has its own hysteresis loop and therefore it can be identified. The hysteresis loop of an ideal material is shown in Figure 12. The characteristic parameters are the spontaneous polarization $P_{s,}$ the remenant polarization P_r and the coercive field E_c.[27] The moment which describes the polarization is defined as

$$P = \frac{q \cdot d}{V}$$

Equation 11: Formula of the polarization P, which is equal to the electric charge *q*, the relative displacement *d* and the volume *V* of the unit cell [28,29]

The coherence between this moment and the electric displacement vector is: [29,28]

$$\vec{D} = \varepsilon_0 \cdot \varepsilon \cdot \vec{E} = \varepsilon \cdot \vec{E} + \vec{P}$$

Equation 12: Electric displacement factor *D*.[28,29]

For an ideal ferroelectric material, the hysteresis loop is symmetric, which means that E_c and P_r are the same. But in reality the loop is affected by many factors such the thickness of the sample, material composition, thermal treatment, defects, measurement conditions and so on. Furthermore, the hysteresis loop shows a difference if it is a single crystalline material or a polycrystalline material. This can be explained by the clamping effect of the domains.[27]
For example, the shape of $PbTiO_3$ is rather square, whereas the $BaTiO_3$ ceramic is tilted at a certain degree. If a $BaTiO_3$ crystal is used instead of a ceramic the *P-E* loop shows a linear course. [25,27]

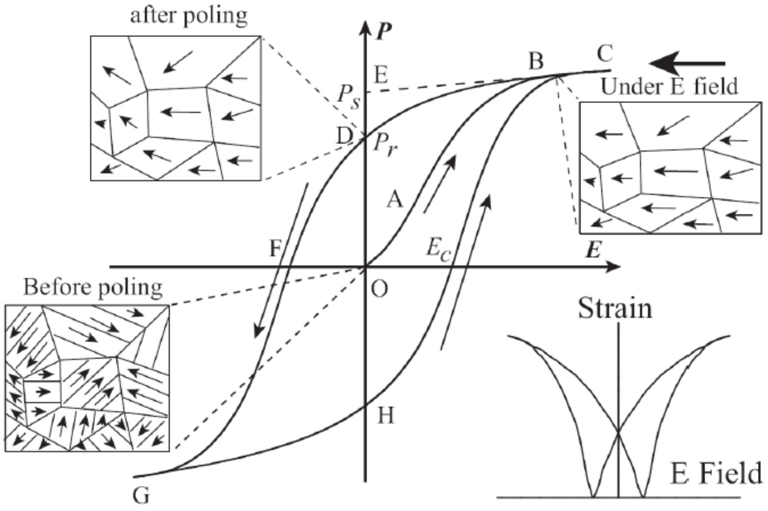

Figure 12: Hysteresis loop of a ferroelectric material and the corresponding polarization rotation.[27]

After poling, when there is no electrical field *E* the remnant polarization E_r can easily determine using the hysteresis loop. The field value at zero polarization is called the coercive field E_c.[25]
To get a zero net macroscopic polarization, the directions of the domains are orientated in a random way. By increasing the electric field strength, the macroscopic polarization is gradually induced. To get a zero polarization a coercive field is needed. An electric field with an opposite direction describes the coercive field. [27]

2.3.3 Ferroelectric Phases and Domains

Ferroelectric domains of a material are volume regions which show the same direction after polarization. All domains have nearly the same energy when a zero field and strain free conditions are applied.[25] Domains are separated by domain walls.[30] If elastic stress and free charge carriers counter the process of domain formation, domain walls are built as seen in Figure 13. [8]

Domain patterns depend on many factors such as the influence of vacancies, dopants and dislocations.[8,25]

The configuration of the domains follows a head-to-tail order to avoid discontinuity in the polarization.

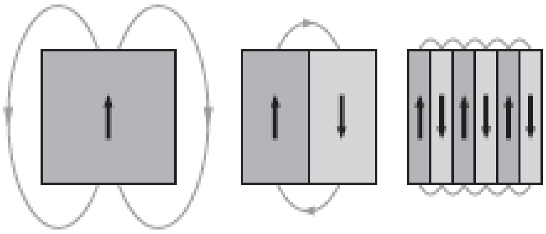

Figure 13: Domain formation. [8]

The 180° domains are the only one which have the potential to reduce elastic energy. 90° domains show a tetragonal structure, whereas 109° and 71° domains are observed in the rhombohedral structure. Two important types of the coarse grained $BaTiO_3$ are Herringebone and Square net pattern. Herringebone is the most common in unpoled ceramics whereas the Square net pattern visualizes the poled state. Both states are shown in the figure below. [8]

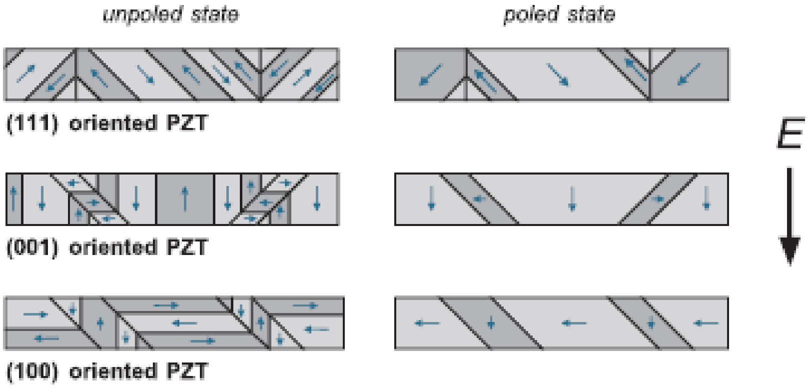

Figure 14: Domain structures of tetragonal PZT and the different orientations. [8]

By polishing and etching or polishing and coating with carbon, the domains can be visualized under the light or electron microscope. The parallel lines by 90° rotations caused in polar directions or domain walls between 90° and 180° domains, make the domains visible. [8]

Also other methods can observe the domain structures like Powder Pattern Method, Liquid Crystal Method, X-ray Topography and so on. Depending on the criteria, also the methods can be combined to reach a good efficiency. [8,12,24]

To sum up, domain structures depend on the symmetry of the ferroelectric material. [24]

2.3.4 Ferroelectric Phase Transitions and Curie-Weiss Behavior

A ferroelectric material represents a spontaneous polarization P_s which increases with decreasing temperature and it arises continuously or discontinuously at a certain temperature.[31] This transition temperature is called Curie-temperature T_c. The symmetry of a crystal changes at a transition point due to the interaction of the atoms in the crystal structure. The spontaneous polarization is produced by phase transition and is called the ferroelectric phase transition.[24,31,32]

At the Curie temperature the material shows a transition from paraelectric to a ferroelectric phase. When the temperature T is smaller than T_c the crystal is not ferroelectric but the other case round $T>T_c$ a ferroelectric behavior is given. When more ferroelectric phases within a structure are observed, the formation from one ferroelectric phase to another phase happens at the transition temperature. This phenomenon is seen in $BaTiO_3$ which is shown in the figure below.[24,8]

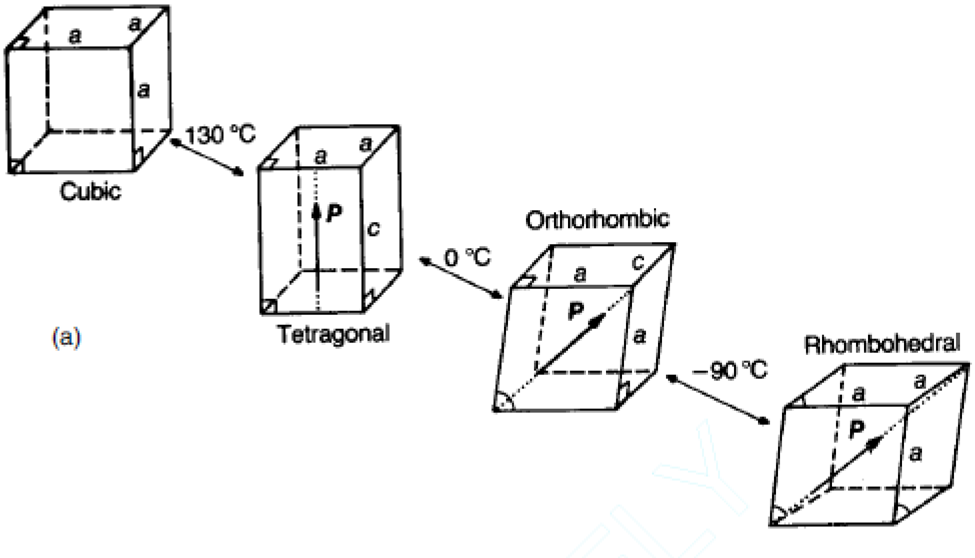

Figure 15: Unit cell of the 4 phases of barium titanate at different temperatures.[24]

In the last century the dielectric properties of $BaTiO_3$ have been studied intensively. Above the Curie temperature, there is a temperature dependence and this can be defined through the Curie-Weiss law:

$$\varepsilon_r` = \varepsilon_0 + \frac{C}{T - T_0}$$

Equation 13: Curie-Weiss law. (C…Curie constant, T…temperature, T_0… Curie-Weiss temperature, ε_0 … permittivity of the vacuum).[24]

The permittivity and the polarization are sensitive to dopants and defects in the crystal. However, in ceramics this effect is more pronounced due to the porosity, grain size, sintering temperature and sintering time.[15] The diagram of the relative permittivity vs temperature of $BaTiO_3$ is visualized in Figure 16.[8]

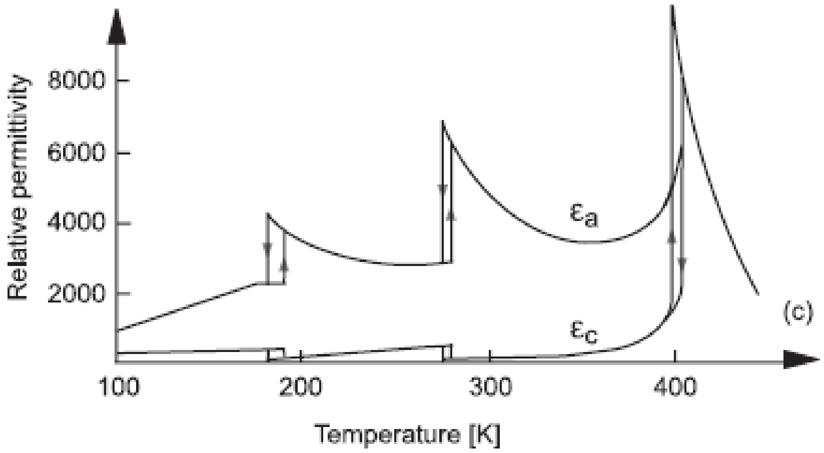

Figure 16: Property of $BaTiO_3$, temperature as function of relative permittivity. [8]

As mentioned above the Curie-Weiss temperature T_0 is different from the Curie Point T_c. In the first order transition the Curie Weiss temperature is smaller than the Curie point whereas in the 2nd order transition the Curie Weiss temperature is the same as the Curie point.[8]

The two types of transitions are the classical ones. They are defined for the classical ferroelectric materials.[15]

The schematic of the transition can be observed in the figure below.

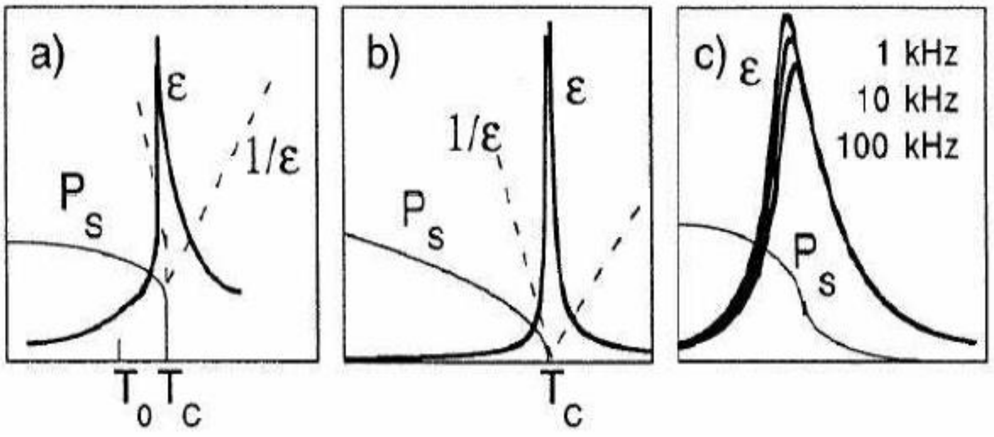

Figure 17: Schematic of the transition states, where (a) shows a first order, (b) a second order ferroelectric and (c) shows the relaxor ferroelectric.[33]

2.3.5 Diffuse Phase Transition

The diffuse phase transition (DPT) is mostly found in ferroelectric materials, which is known as ferroelectric diffuse phase transition (FDPT). The FDPT were first studied in the 1950s by Smolenskii. [34]

So the important characteristics of DPT are:

- The permittivity- temperature curve shows broad maxima,
- with increasing temperature, the spontaneous und remnant polarization decrease gradually,
- the transition temperature is different by using different techniques,
- relaxation character in the transition region and
- no Curie-Weiss behavior above the transition temperature.

The broad maxima of the transition region are important for the application of relaxor materials. It is mentioned that the DPT is an appearance of fluctuation, in a large temperature range. The fluctuation is divided into two types: compositional and structural fluctuation. The compositional fluctuation is described for ferroelectric solid solutions whereas the structural fluctuation is present in the temperature region around the transition point. [34,35,8]

The structural disorder at different sites has been responsible for the DPT in a perovskite (ABO_3) structured ferroelectric material. [36]

The gradual transition from a paraelectric to a ferroelectric phase below the Curie temperature T_C can be indicated by plotting the relative permittivity as a function of temperature. [24]

Rolov et al calculates the diffuseness parameter for both fluctuations with the Gaussian concept.[37,36]

$$\frac{1}{\varepsilon} - \frac{1}{\varepsilon_m} = \frac{(T - T_m)^{\gamma}}{C}$$

Equation 14: Modified Curie-Weiss law where γ and C are constants, ε_m and T_m are the dielectric maximum and the temperature maximum. [24]

The diffuseness constant γ describes the character of the phase transition. If $\gamma = 1$ the normal Curie-Weiss law is followed and $\gamma = 2$ describes a complete diffuse phase transition. [38]

The region below the transition temperature of ferroelectrics is important due to the mechanical and electric properties. For many applications it is important to use that broad maxima to shift the temperature to the range of interest.

2.4 Advanced Ferroelectrics – Relaxors

In the beginning it should be mentioned that relaxor ferroelectrics have similar properties to those of spin and dipole glasses. A characteristic of ferroelectric relaxor materials is the occurrence of random electric fields in the lattice due to cations of different charge number or different size on equivalent sites (chemical disorder). Lead based B-site perovskite materials are the common used materials.[39] The relaxor material includes a number of lead based perovskite type materials like $Pb(Mg_{1/3}Nb_{2/3})O_3$ (PMN) and $Pb(Zn_{1/3}Nb_{2/3})O_3$ (PZN). Recently, relaxor properties were also found in lead free materials like $BaTiO_3$-$CaTiO_3$-$BaZrO_3$ (BCZT)[40], $Ba(Ti,Zr)O_3$ (BZT)[41] and $BaTiO_3$–$x$$CaTiO_3$–$SrTiO_3$.[42]

To identify the relaxor class a broad peak has to be present when the relative permittivity ε_r versus the temperature is plotted.[8]

2.4.1 Dielectric Properties of Relaxors

Normal ferroelectrics show no strong frequency dependence, whereas relaxors show a frequency dependence of the dielectric permittivity as a function of temperature. The temperature of the maximum of the relative permittivity T_m is near the Curie temperature T_C. Instead of a sharp phase transition at T_C, a diffuse phase transition takes place, as already mentioned in Chapter 2.3.5. The relaxor materials do not follow the Curie-Weiss law up to the so called Burns temperature T_d. Above the Burns temperature the Curie-Weiss law is valid. [43] In the figure below, the difference of normal ferroelectric and the two different relaxor types are shown.

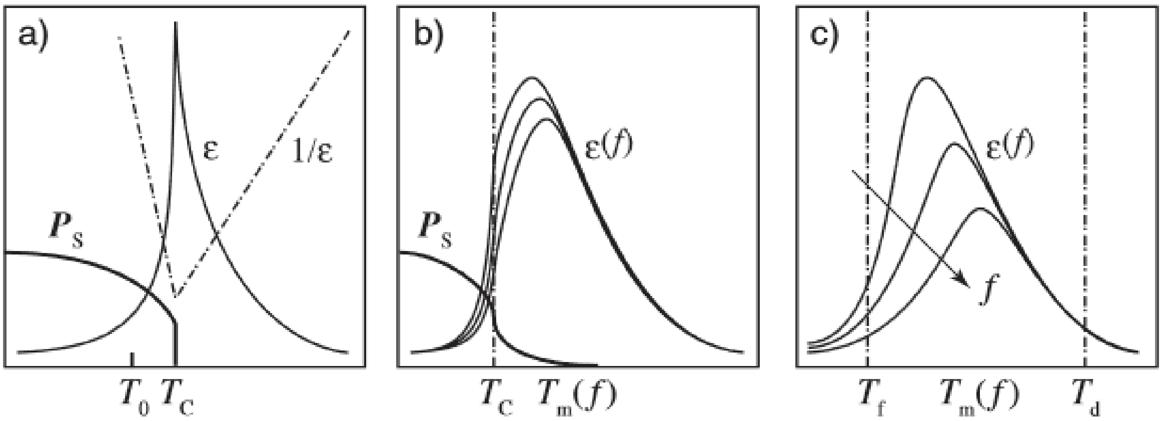

Figure 18: Illustration of the difference for (a) a normal ferroelectric, (b) a relaxor with a diffuse relaxor to ferroelectric phase and (c) a canonical relaxor.[43]

As mentioned above the Curie-Weiss law is not valid in relaxor materials, they can be approximated by a quadratic relation.

$$\chi = \frac{C}{(T - T_0)^2}$$

Equation 15: Quadratic Curie Weiss-law.

2.4.2 Performance of Relaxors

As already noted in the Chapter Diffuse Phase Transition, the ferroelectric relaxor behavior is a result of the of the fluctuation of polar regions and the structural disordering. A perovskite relaxor with mixed oxides shows a disorder in the structure and therefore the properties and physics of that material are described.

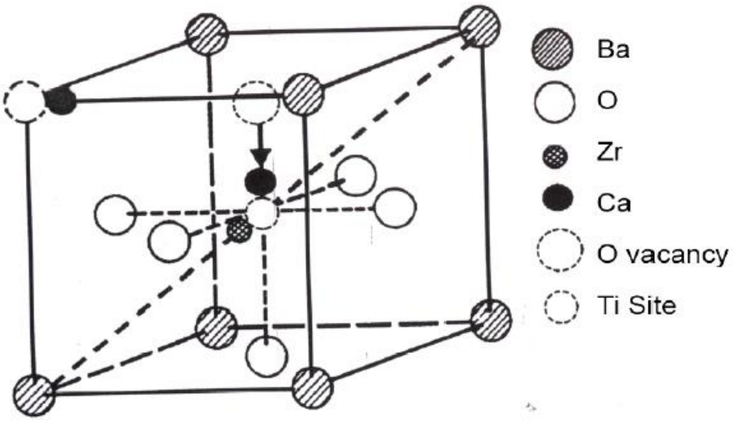

Figure 19: The cubic ABO_3 structure of $BaTiO_3$ with vacancies and substitution of Zr^{4+} and $Ca^{2+.}$

The relaxor material is defined through the macroscopic symmetry change at the transition temperature, in nanometer scale. This nanoscale leads to polar nanodomains which exist above the transition temperature and are crucial for the properties. Due to the high relative permittivity of relaxors they are commonly used in capacitor technology. To sum up, relaxors show a new area of ferroelectrics and verify an interesting area for researchers and industry.[15,24]

2.4.3 A brief Survey through the Theoretical Approach of Relaxor Materials

Bokov et al discussed the polar nanoregions in a detailed way. The nanoregions are existing due to the structural disorder which is influenced by temperature. So a rapid phase transition is taking place to a ferroelectric or antiferroelectric state. [39]

The first approach was done in the 1950s by Smolenskii and Isupov.[34] Relaxor materials are characterized by their chemical composition and the concentration of the ions which share the same side. Therefore, a compositional fluctuation occurs. However, the cation concentration alone cannot explain the frequency dependence. [39] Cross et al proposed that the flipping of the different orientations is a model of nanoregions and that show the frequency dependence.[16] Nowadays, there are many different models which explain the relaxor frequency dependence:

First concept:

The basis of the dipole- glass model describes that the crystals with polar nanoregions show a lower symmetry and are embedded into a matrix with cubic symmetry. The main disadvantage is that there is no overlapping from relaxor to ferroelectric state and no electric field. [29,16]

Second concept:

It describes that the whole crystal consists of low symmetry nanodomains which are separated by the domain walls with a thickness of 100nm or lower (comparable to the size of nanodomains). This model contains the random field model as Westphal and Kleemann reported. [44] It describes that a second order phase transition is hindered when the random local fields do not exist. Furthermore, this system shows a continuous orientational symmetry. In a perovskite type relaxor the crystallographic directions can be aligned in different directions and therefore they can be called quasi continuous. But it must be given that the directions are as large as in the phase transition from cubic to rhombohedral. This concept concludes the domain wall motion to describe the frequency dependence. [45]

The order of the perovskite structure depends on the electrostatic interactions, the bonding and the repulsions. Glinuck and Fari reported a random field theory, which says that the ferroelectricity of cations is embedded in a polarizable matrix. The dipole-dipole interaction are random which leads to a ferroelectric order at low temperature.[46]

Bokov et al described a similar model of short range repulsion between the ions. [39] Furthermore, the random field theory of covalent bonding has been introduced by Egami et al.[47]

2.5 Solid State Reaction

The solid state reaction is the classical way to prepare $BaTiO_3$ at temperatures as high as 1200°C. Such high calcination temperatures conclude coarse grained materials of some µm size which is due to the intensive milling step. Furthermore, the calcination temperature depends on the milling step and the morphology. To prepare such fine powders other preparation methods like hydrothermal, oxalate and alkoxide method can be used.

The solid state reaction type is based on a diffusion controlled reaction and starts from barium carbonate and titan dioxide. [48,49]

$$BaCO_3 + TiO_2 \longrightarrow BaTiO_3 + CO_2\uparrow$$

Reaction equation 1: Forming reaction of barium titanate. [48]

Beauger, Muttin et al reported that $BaCO_3$ reacts with $BaTiO_3$ and BaO is used as mobile agent. BaO diffuses into the TiO_2 at the interface and furthermore an intermediate layer barium orthotitanate at 1100°C is formed. [49,48]

$$BaCO_3 + BaTiO_3 \longrightarrow Ba_2TiO_4 + CO_2\uparrow$$

Reaction equation 2: Forming reaction of barium orthotitanate. [49]

The remaining TiO_2 starts to react slowly with the barium orthotitanate to barium titanate. This means that a diffusional exchange between Ba^{2+} and Ti^{4+} rich regions is taking place. [48]

$$Ba_2TiO_4 + TiO_2 \longrightarrow 2\ BaTiO_3$$

Reaction equation 3: Formation of barium titanate. [49]

Subsequently, the $BaCO_3$ are completely dissolved in TiO_2 and so it can be mentioned that the morphology of $BaTiO_3$ is determined by the TiO_2 particles. However, Henning et al also found out that a large amount of the intermediate phase is formed when the particle size of $BaCO_3$ and of TiO_2 is small. Hence, the particle size of $BaCO_3$ is a significant influence to the monophase of $BaTiO_3$ and also to $(Ba,Ca)(Zr,Ti)O_3$ (BCZT). The BCZT ceramic is a commonly used dielectric material. [48]

In the following figure, the reaction mechanism of $BaTiO_3$ is shown.

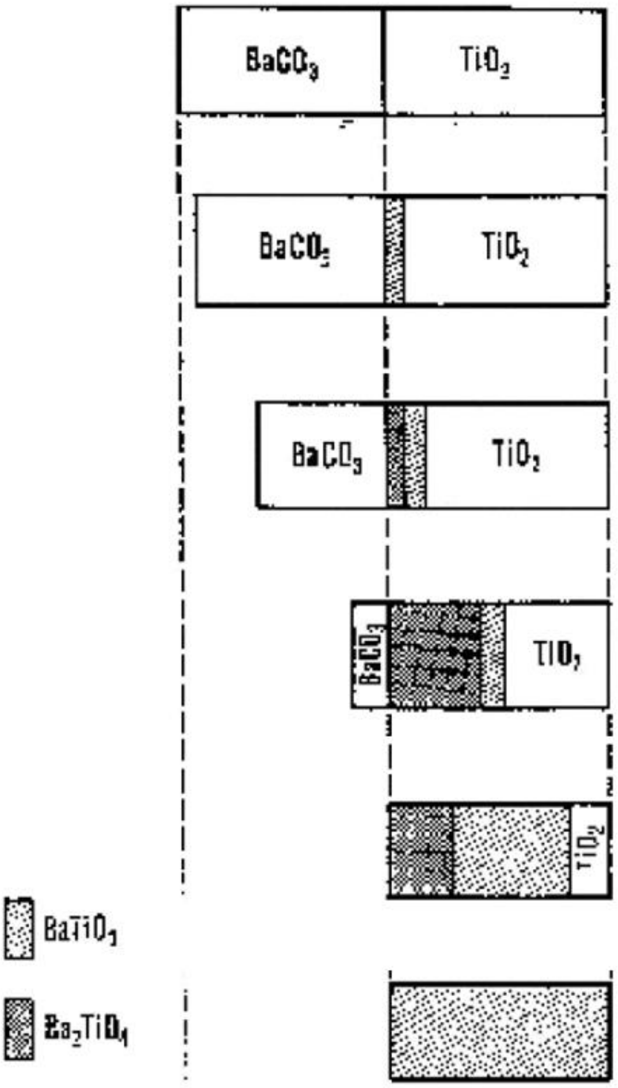

Figure 20: Diffuse reaction mechanism of the solid state reaction of $BaTiO_3$.[49]

2.5.1 Kinetic Model

Carter reported that a component A reacts with a component B to a product with a defined thickness y. [50]

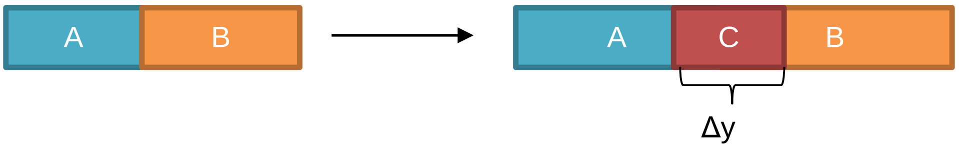

Furthermore, he also assumed that the reaction is diffusion limited. The reaction product is inverse proportional to the thickness y.[50]

$$\frac{dy}{dt} = \frac{k}{y}$$

Equation 16: Definition of the thickness. [50]

The quantity of Q_A is defined as the volume of a circle. The rate of the quantity Q_A is equal to the flux of the material through the thickness of the shell. [50]

$$\frac{dQ_A}{dt} = \frac{-4\pi k_1 r_2}{(r_2 - r_1)}$$

Equation 17: Change of the Q_A, where k is the reaction constant. [50]

This equation for the steady state condition is provided by the activity of the diffusing species at the interface and the thickness of the layer. The area of the diffusion increases with the square of the radius in the shell. The thickness of the shell must be equal all the time when flux is going through. The diffusions coefficient *Ddc/dy* at any time must vary at the diffusion layer as $1/r^2$.

Therefore, the diffusion controlled reaction can be defined at any time as followed:

$$\Delta y(t) = \sqrt{2V_{AB}\, \Delta G_{AB}{}^{0} (D_A + D_B) \cdot t}$$

Equation 18: Kinetic of the diffusion controlled reaction. (*t*…time, *V*… volume, *G*…Gibbs energy, *D*…diffusions coefficient)[51]

When $D_A >> D_B$ the thickness will increase at the interface C/B and when $D_B >> D_A$ it increases on the interface A/C. To sum up, it can be said that the more reactive compound covers the reaction partner.[51]

2.5.2 Defects

Before starting to discuss defect chemistry of $BaTiO_3$ the abbreviations have to be determined. Therefore, the Kröger and Vink notation is used.

Table 1: Kröger-Vink notation for ionic point defects in a binary oxide MO. The indices ´, • and x describe the negative, positive and neutral charge. [12]

Symbol	Term
$\mathbf{M_M}$	Metal cation M^{2+} on a regular lattice site
$\mathbf{O_O}$	Oxygen ion O^{2-} on a regular lattice site
$\mathbf{V_M^X, V_M^{\prime}, V_M^{``}}$	neutral, simply negative and doubly negative cation vacancy
$\mathbf{V_O^X, V_O^{\bullet}, V_O^{\bullet\bullet}}$	neutral, simple positive and doubly positive anion vacancy
$\mathbf{M_i^x, M_i^{\bullet}, M_i^{\bullet\bullet}}$	neutral, simple positive and doubly positive interstitial cation
$\mathbf{O_i^x, O_i^{\prime}, O_i^{\prime\prime}}$	neutral, simply negative and doubly negative interstitial anion

The Kröger-Vink notation takes into account the electron neutrality, the conversation of the mass and the space ratio of anion and cation. Defects can be introduced through non stoichiometry and dopants and are subjected thermodynamically equilibriums reactions and the kinetic.[12]

The entropy (*ΔS*) increases due to the thermodynamic equilibrium. This is shown through the lower Gibbs free energy (*ΔG*):[12]

$$\Delta G = \Delta H - T\Delta S,$$

Equation 19: Formula of the Gibbs energy.

Where T is the temperature and *ΔH* is the enthalpy. No crystals are absolutely perfect and therefore the degree of imperfection is tolerated before second phases develop varies from compound to compound. Defects in solids are important due to the structure of the material and the performance. As mentioned in the beginning, $BaTiO_3$ are used in the MLCC and therefore the defect chemistry, composition and processing of $BaTiO_3$ is better understood. Many studies show a shift of phase transitions when a dopant is added. Hence, to control the dopant concentration and distribution, the dielectric properties are important. [52]

The defect chemistry has been studied by Frenkel, Schottky, Kröger and Vink and Wagner. It can also be adjusted by the oxygen partial pressure. Therefore, the oxygen deficiency can lead to oxygen vacancies or interstitial cations. By oxygen excess oxides can move to cation vacancies or oxygen ions can move to interstitial places. The resulting holes are compensated by cations [12]

Dopants are often used in the systems BZT or BCZT to change the electrical properties. An excess of oxygen can lead to cation vacancies during the sintering process. [12,40,53]

The complex ternary system is difficult to understand, $BaTiO_3$ can be used to describe the defect model. Daniels and Hardtl reported the defect model for donor doped barium titanates.[52]

$$K_i = N_C N_V e^{\frac{-E_g}{k_B T}} = 10^{45} e^{\frac{-2.9eV}{k_B T}}\, cm^{-6}$$

$$K_{Re} = [V_O^{\bullet\bullet}] n^2 pO_2^{\ 1/2} = 10^{27} e^{\frac{-2.9eV}{k_B T}}\, atm^{1/2} cm^{-3}$$

Equation 20: Equilibrium constants K_i for electronic reaction and K_{RE} for reduction reaction. (N_C and N_V… effective conduction band density and effective valence band density, E_g… band gap energy, T… absolute temperature, k_B… Boltzmann constant, $[V_O^{\bullet\bullet}]$… concentration of double ionized oxygen vacancy, n… concentration of the electron).[52]

Wernicke et al specified the diffusions coefficient of barium and oxygen vacancies. The activation energy is calculated with 2.05 eV for oxygen and 2.76 eV for barium. [52]

$$D_{V_O^{\bullet\bullet}} = 5.7 \cdot 10^3 e^{\frac{-2.05eV}{k_B T}}$$

$$D_{V_{Ba}''} = 6.8 \cdot 10^2 e^{\frac{-2.76eV}{k_B T}}$$

Equation 21: Diffusions coefficient of oxygen and barium vacancies. [52]

Such componds as $BaTiO_3$ can have two types of defects:

1. Schottky defects
2. Frenkel defects

The binary systems ensue the Schottky defect reaction but $BaTiO_3$, which is a ternary system, follows the partial Schottky reaction. That reaction can be a extrinsic defect due to the variation of Ba:Ti ratio. [52]

Partial Schottky defect reaction for $BaTiO_3$:

The partial Schottky reaction of a Ba-rich $BaTiO_3$ is described in the following equations. The TiO_2 partial Schottky defect can be described in the solubility regime.

$$BaO \xrightarrow{BaTiO_3} Ba_{Ba}^{X} + O_O^{X} + V_{Ti}'''' + 2V_O^{\bullet\bullet}$$

Reaction equation 4: Partial Schottky defect reaction.

After the BaO solubility is increasing the reaction is reversed from right to left hand side and then a formation of the secondary phase barium orthotitanate can be observed. So following reaction is given

$$Ba_2TiO_4 \xrightarrow{BaTiO_3} 2Ba_{Ba}^{X} + Ti_{Ti}^{X} + 4O_O^{X} + V_{Ti}'''' + 2V_O^{\bullet\bullet}$$

Reaction equation 5: Partial Schottky defect reaction of the secondary phase.

The electron neutrality is given by

$$[V_O^{\bullet\bullet}] = 2[V_{Ti}''''] .$$

Equation 22: Electron neutrality.

The equilibrium constant is defined as and furthermore it is assumed that $a_{BaO} = x_{BaO}$

$$K_{Ba-rich} = [V_{Ti}^{''''}][V_O^{\bullet\bullet}]^2 a_{BaO}$$

$$K_{Ba-rich} = [V_{Ti}^{''''}][V_O^{\bullet\bullet}]^2$$

Equation 23: Equilibrium constant K.

At equilibrium state the equilibrium constant K and the defect concentration can be linked.

2.6 Zr^{4+} doped $BaTiO_3$ ceramics

$BaTiO_3$ ceramics gained great interest due to the ferroelectric characteristics. Its low Curie temperature T_C of 120°C sets a limit for high power transducers and the low electromechanical coupling factor is not as interesting as that of PZT. The drawback of pure $BaTiO_3$ is the high temperature coefficient near the Curie temperature. The high temperature coefficient can be avoided by adding dopants due to the shifting of the transition temperature. $BaTiO_3$ shows a multiple ferroelectric- ferroelctric phase transition which results in a temperature dependence of piezoelectric properties. A large piezoelectric coefficient results by a substitution on the Ba^{2+} or Ti^{4+} side. Also a good electromechanical coupling factor and a more stable structure is observed. An important example is $Ba(Zr,Ti)O_3$ which can be used in many devices. [54,22]
Yu, Guo et al reported the phase diagram of $Ba(Zr_xTi_{1-x})O_3$. [55]
The ferroelectricity of BZT ceramics changes with the Zr^{4+} content. Therefore, at higher Zr^{4+} content x>0.08 show a broad peak by plotting temperature vs the relative permittivity ε_r due to the inhomogeneous distribution of Zr^{4+} ions in the Ti^{4+} site. With a Zr^{4+} content of x=0.20 only one phase transition exists and by increasing the content to x=0.25 the typical relaxor behavior can be observed. [55] BZT ceramics show a rhombohedral and tetragonal structure in the range of $0.10 \leq x \leq 0.15$. Above that Zr^{4+} content range the structure changes from rhombohedral to cubic. [56–59]
Rehrig et al reported that the BZT ceramic with a low Zr^{4+} content provide a crystal growth in milimeter size and a piezoelectric coefficient of 355 pC/N is determined at room temperature.[58]
In 2015 Yang, Wu et al pointed out that with a Zr^{4+} content of 6% the piezoelectric coefficient is 420 pC/N with the conventional solid state method at 1400°C for 100 hours. [60]
In literature the BZT ceramics were prepared through solid state method using a calcination temperature between 1100°C and 1250°C with 2 to 12 hours holding time. [61] The sintering time is used with 1400°C to 1500°C with a holding time of 2 hours. [62,63] Furthermore the relative density is determined with 90% to 94% as Mahesh et al reported. [64]

2.7 Ca^{2+} and Zr^{4+} doped $BaTiO_3$ ceramics

Ca^{2+} and Zr^{4+} doped $BaTiO_3$ (BCZT) are used as key materials for multilayer ceramic capacitors (MLCC) due to their high capacitance. They are so called Class 3 capacitors. Their temperature specification is Y5V. [65] This kind of compound is important due to its electrical properties and it is healthier and environmental friendlier than lead based materials.

Lui and Ren prepared a piezoelectric ceramic system $Ba(Ti_{0.80}Zr_{0.20})O_3$-$(Ba_{0.70}Ca_{0.30})TiO_3$ (BZT-BCT) which shows a quite high piezoelectric coefficient of 620 pC/N. That piezoelectric coefficient is comparable to that of PZT. Their phase diagram visualizes a morphotropic phase boundary (MPB) which starts from a rhombohedral and tetragonal phase and by increasing the temperature to the triple point a cubic phase has been found. [66]

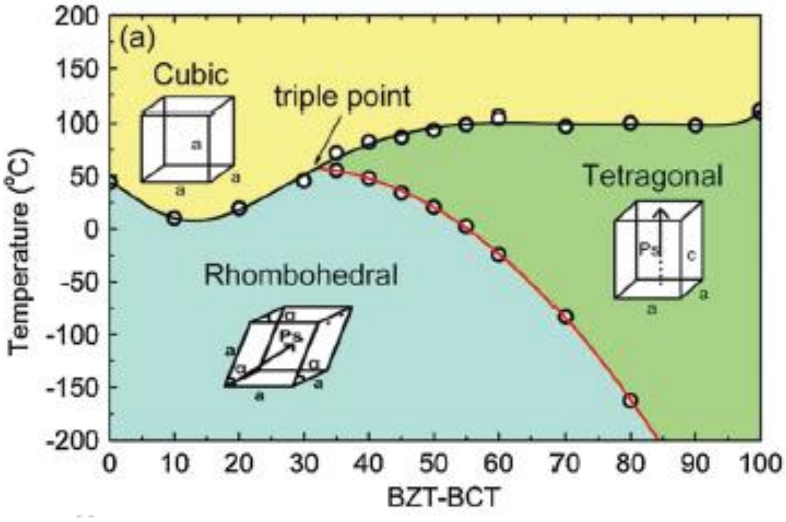

Figure 21: Phase diagram of the BZT-BCT system. [66]

They found out that the important feature of such systems is that a cubic-rhombohedra-tetragonal triple point is existing at x=0.32 and T=57°C. This point optimizes the piezoelectric coefficient of many lead based systems. The vanishing polarization anisotropy at the MPB enhances the piezoelectricity and leads to a small energy barrier between the ferroelectric phases. Furthermore, the rotation between rhombohedral and tetragonal phases is facilitated.[66]

In contrast to Liu and Ren, Keeble et al reported that the BCZT ceramics show an intermediate orthorhombic phase. Also the tetragonal – rhombohedral phase transition was identified as tetragonal- orthorhombic transition. Furthermore, the orthorhombic- rhombohedral phase coalesces near the triple point, as seen in Figure 22. [67]

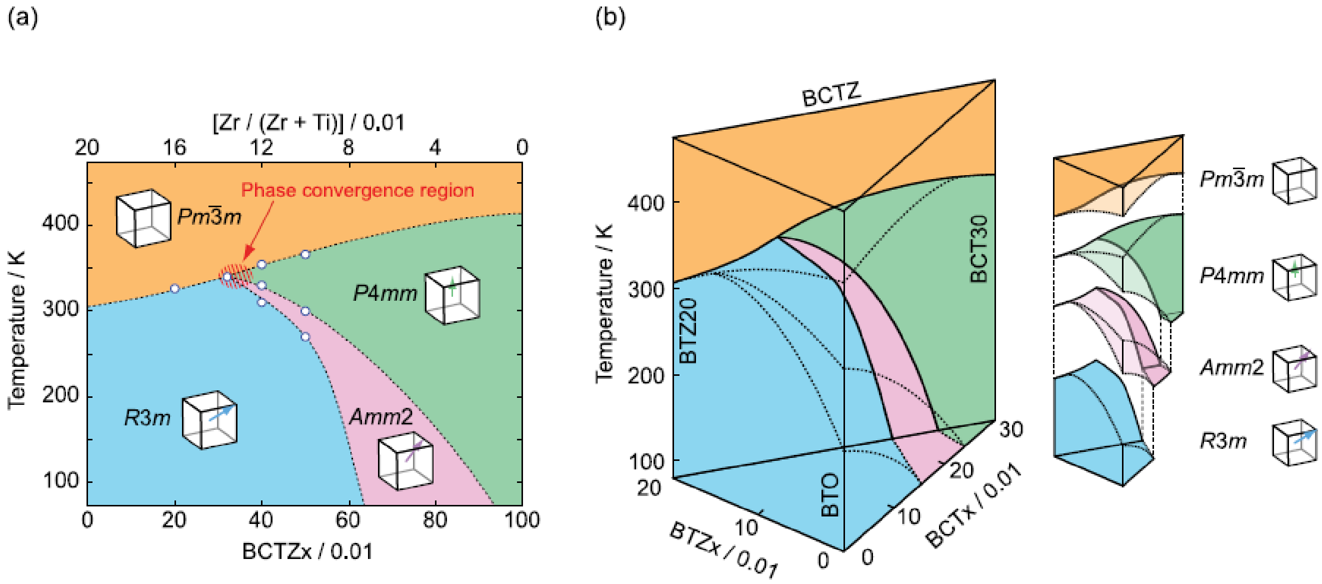

Figure 22: (a) Phase diagram of BCZT, which is based on the studies before. In contrast, an orthorhombic phase is observed. (b) A 3D phase diagram of BCZT, which shows how the binary BZT and BCT form the ternary BCZT. [67]

To show the intermediate phase they use a high resolution synchrotron and X-ray diffraction was used.[67]

Liu and Ren also discussed the BCZT ceramic with x=0.50 due to the location near the MPB in Figure 21 and the piezoelectric coefficient of 560-620 pC/N. [66] Xue, Zhou et al studied the piezoelectric, dielectric and elastic properties of the BZT-50BCT ceramic in a detailed way. They also changed the concentration of Ca^{2+} and Zr^{4+} in the compound. [68] Li, Xu et al reported that the $(Ba_{0.84}Ca_{0.16})(Ti_{0.90}Zr_{0.10})O_3$ have a high dielectric constant around 4800 and also determines a coexistence of orthorhombic and rhombohedral phases. They also show that the ceramic with a calcium content of 8% and a zirconium content of 5% has a piezoelectric constant of 365 pC/N between orthorhombic and tetragonal phases. The Curie temperature is increasing to 115°C when the Ca^{2+} content is 1% and the Zr^{4+} content is 2%. The polymorphic phase transition gained opportunity to improve the dielectric properties of the ceramic material. With increase of the Ca^{2+} content the polymorphic phase transition shifts to lower temperature and cannot be seen above the room temperature with x=0.18. [69]

Zhang et al studied the $(Ba_{0.95}Ca_{0.05})(Ti_{1-x}Zr_x)O_3$ ceramics by varying the Zr^{4+} content and found out with the X-ray diffraction that there is a coexistence of a orthorhombic and pseudocubic phase. The orthorhombic-pseudocubic phase transition temperature is shifted near to room temperature with a Zr^{4+} content of 4%. So by optimizing the zirconium content, the electric properties are as good as that of the lead based ceramics.[70]

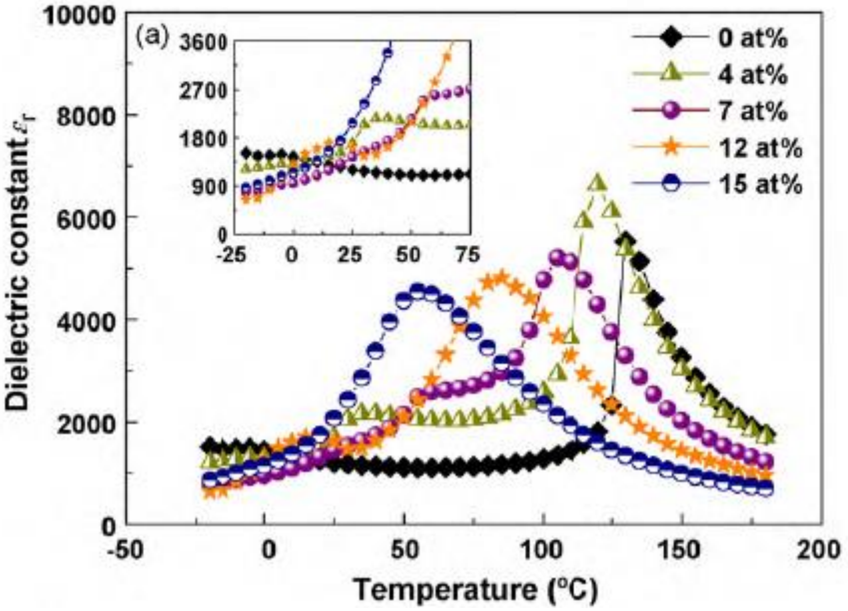

Figure 23: Relative permittivity as a function of temperature, with varying Zr^{4+} content. [70]

3 Experimental Part

This chapter introduces preparation, examination and characterization of the samples. The preparation of (Ba, Ca) (Ti,Zr)O_3 is done via mixed oxide route.
The chapter shows the testing of different barium to calcium and zirconium to titanium ratio.

3.1 Sample Preparation

As mentioned above the samples are produced via mixed oxide route, which are displayed in the table below.

Table 2: Produced samples with their abbreviations.

Samples	Abbreviation
$BaZr_{0.20}Ti_{0.80}O_3$	BZT80
$BaZr_{0.25}Ti_{0.75}O_3$	BZT75
$BaZr_{0.25}Ti_{0.75}O_3$ + 1% TiO_2	BZT75-1
$Ba_{0.80}Ca_{0.20}ZrO_3$	BCZ80
$Ba_{0.80}Ca_{0.20}Zr_{0.20}Ti_{0.80}O_3$	BCZT80
$Ba_{0.94}Ca_{0.06}Zr_{0.20}Ti_{0.80}O_3$	BCZT94

The amount of the starting materials is calculated and weighted according to the formula below. As starting materials $BaCO_3$, $CaCO_3$, ZrO_2 and TiO_2 from the producer MERCK with a purity of 99% are used.

$$\boldsymbol{E_n} = \frac{\boldsymbol{A_n \cdot B_n}}{\boldsymbol{C_n}} \cdot \frac{\boldsymbol{E_{ges}}}{\sum_{i=1}^{n} \frac{A_i \cdot B_i}{C_i}} \qquad\qquad C_n = \frac{x_{metal} \cdot M_{metal}}{M_{ges}}$$

Equation 24: Calculation of the weighted portion.

A_n... molar mass of the educt / g·mol^{-1}
B_n... proportion of the metal in the ceramic / g·g^{-1}
C_n... metal content of the oxide or the carbonate / g·g^{-1}
E_{ges}... Amount of the raw materials / g
E_n...weighted portion of the educt / g
x_{metal}… amount of the metal /1
M_{metal}…molar mass of the metal / g·mol^{-1}
M_{ges}… molar mass of the starting material / g·mol^{-1}

Table 3: Calculation for $Ba_{0.80}Ca_{0.20}Zr_{0.20}Ti_{0.80}O_3$ (E_{ges}=10g)

BCZT	**$BaCO_3$**	**$CaCO_3$**	**ZrO_2**	**TiO_2**	
$C_n/g \cdot g^{-1}$	0.6959	0.4004	0.7403	0.5994	
$B_n/g \cdot g^{-1}$	0.8000	0.2000	0.2000	0.8000	
$A_n/g \cdot mol^{-1}$	137.330	40.078	91.224	47.880	
$\frac{A_n \cdot B_n}{C_n}$	157.874	20.019	24.645	63.904	**Σ=266.442**
E_n/g	5.925	0.751	0.925	2.398	

To get a homogenous mixture of the different starting materials, the weighted educt are mixed within a ball mill (Retsch S 1000) with distilled water. As milling medium yittrium stabilized zirconia balls are used. The raw materials are pre milled for 1 hour with 60 rpm. Afterwards the white suspension is sieved to separate it from the zirconia balls and dried in the compartment drier at 80°C for 24 hours.

The calcination process is done in a batch furnace Nabertherm C290 at 1250°C for 5 hours. The heating and cooling rate of 5°C/min is selected. Formation of the desired perovskite compound was examined by X-ray diffraction (XRD).
In Figure 24 the temperature program for the calcination process is shown.

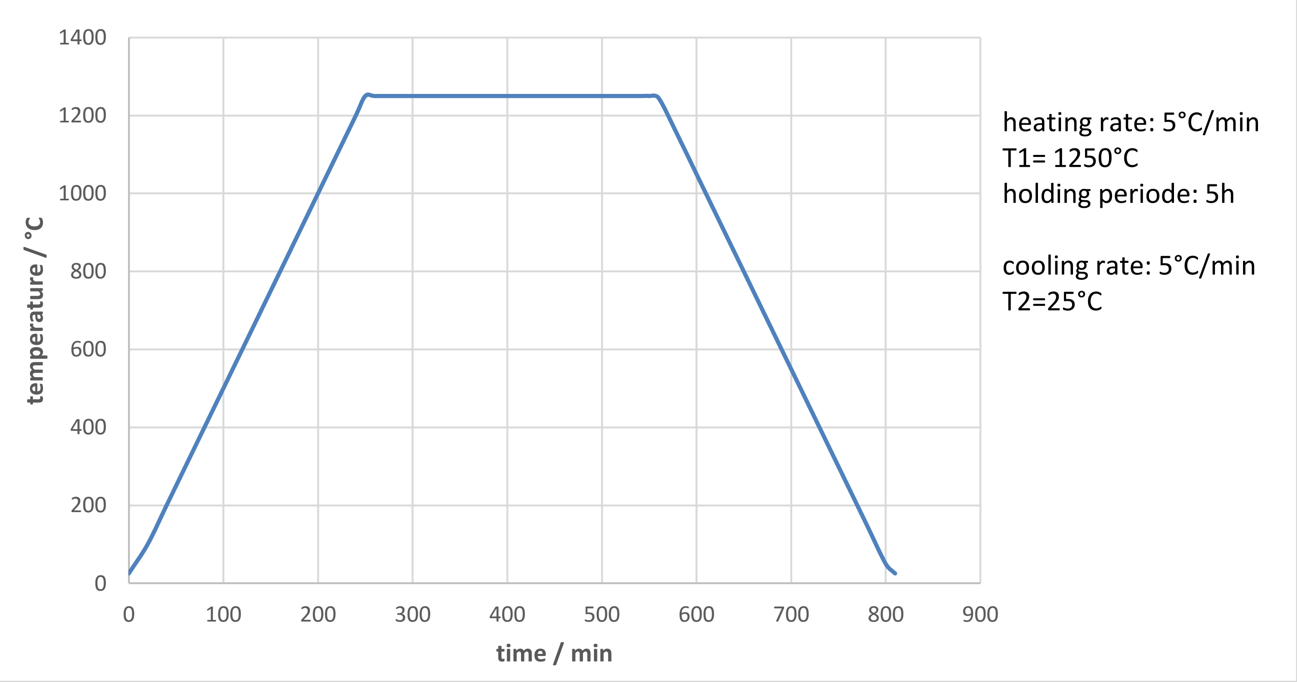

Figure 24: Temperature curve for the calcination process

The reaction control of the calcined powder is done through XRD analysis. Afterwards the raw material has to be milled again. Milling is done in the same way as in the pre milling step with distilled water, milling for 1 hour with 60 rpm and drying in the compartment drier (24h at 80°C). This milling step is used to reduce the particle size before starting with the granulation. Afterwards the white powder needs to be granulated because the fine product can hardly be formed by pressing.

Before pressing, debindering and sintering the fine material is treated with 3% binder (30wt% polyethylene glycol PEG). After granulation (addition of binder) the samples are sieved with a mesh wide of 315 µm and 180 µm. Afterwards the material can be used for further processing.

Subsequently, the powder is pressed into disc shaped samples with a diameter of 13 mm. Pressing is executed with a maximum force of 2 tons (150 MPa) and a duration of 5 minutes.

Before starting the debindering program the green density of the discs is determined by weighing and measuring the geometrical dimensions with a vernier caliper.

Through pyrolysis the binder is removed (decomposition to CO_2 and H_2O) with the following temperature program in a batch furnace (Figure 25).

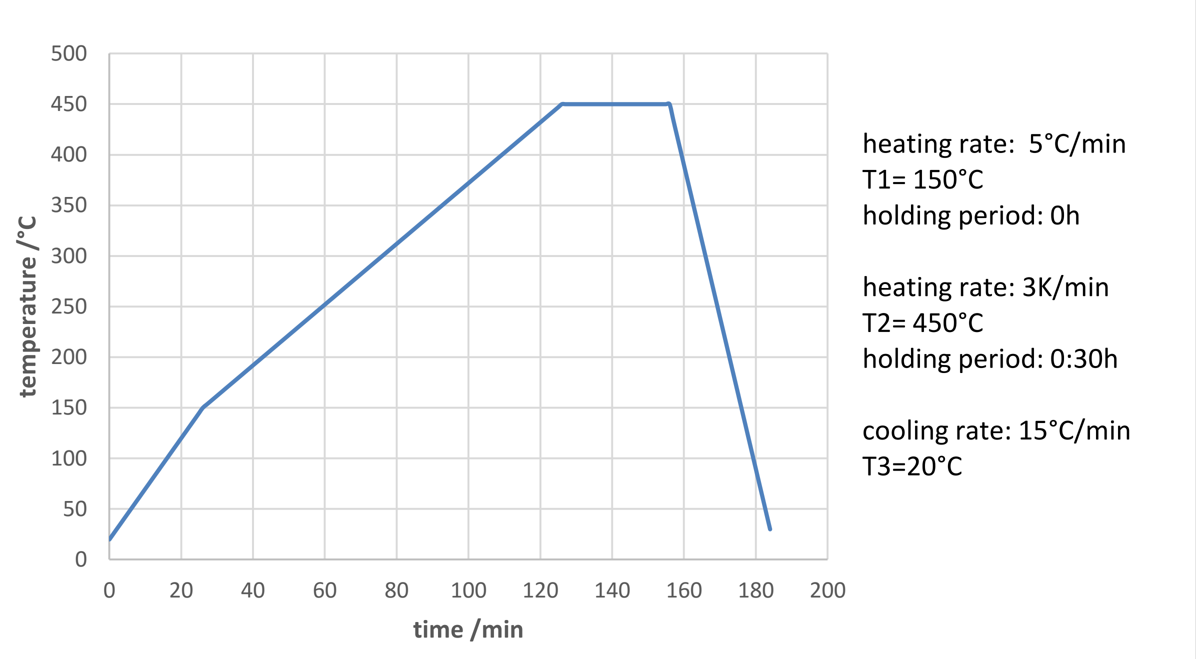

Figure 25: Temperature curve of the debindering process

In the debindering step it is important that the decomposition is preceded completely, otherwise the product can be affected negatively. To accelerate the pyrolysis, the reaction is done with open Al_2O_3 crucibles.

After debindering the samples need to be sintered. The sintering process defines the ferroelectric behaviour and is the determining forming step. The aim is to achieve dense samples without decomposition and evaporation of the components. Sintering is done under air atmosphere in closed Al_2O_3 crucibles.

Besides, to ensure a good density, the sintering temperature of the (Ba,Ca)(Zr,Ti)O_3 ceramics is set to 1400°C with a heating and cooling rate of 5°C/min (Figure 26).

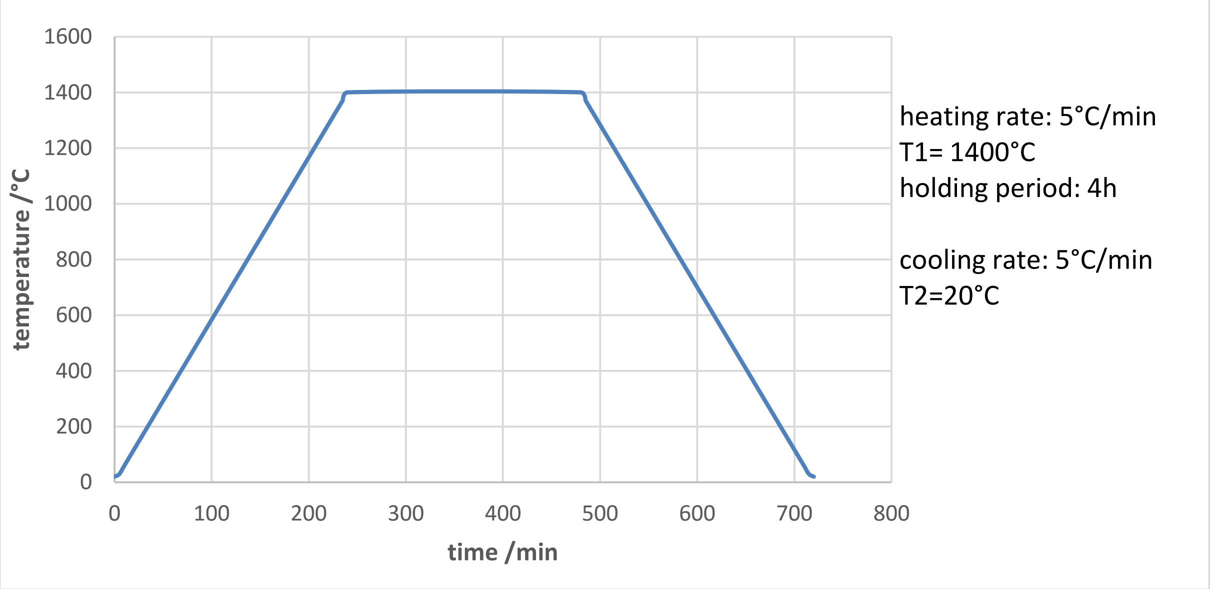

Figure 26: Temperature curve of the sintering process

One of the sintered samples is now crushed and freshly grounded with an agate mortar to examine the structure, phase and lattice parameters via XRD analysis at room temperature. Before crushing the sample, the length and diameter of the disc is measured with a vernier caliper to calculate the relative density.

From the crude material a high temperature XRD is done by a X-ray diffraction spectrometer Panalytical XPert Pro MPD equipped with HTK 1200NK (Anton Paar) to pursued the forming reaction of the material. The measurement is done from room temperature to 1200°C using 50°C intervals.

Also an electric measurement is done. Samples are either sputtered with 100nm gold for 30 minutes at each side or get coated with silver conductive paint. To remove upstands at lateral surface a fine silicon carbide grinding paper (800 mesh) is used.

The impedance spectroscopy is done in a temperature range from -50°C to 300°C, only the sample $Ba_{0.80}Ca_{0.20}ZrO_3$ is measured in a lower temperature range as Levin, Amos et al suggests.[53]

3.2 Sample Characterization

To characterize the prepared samples, the following measurements were used. These techniques are standard methods for solid state analysis.

3.2.1 Simultaneous Thermal Analysis with Mass Spectrometry (TG/DSC-MS)

The educt mixture was characterized by differential scanning caloriemetry (DSC) and thermogravimetry (TG) with mass spectrometry (MS) in a Netzsch STA Model No 409C under air, with different heating rates.

The properties of the powders were measured under air (flow rate N_2:O_2= 80:20 mL/min) with the heating rates 10K/min, 5K/min and 3K/min from room temperature to 1400°C. The different heating rates are used to extrapolate the data to 0 K/min, as seen in Figure 27.

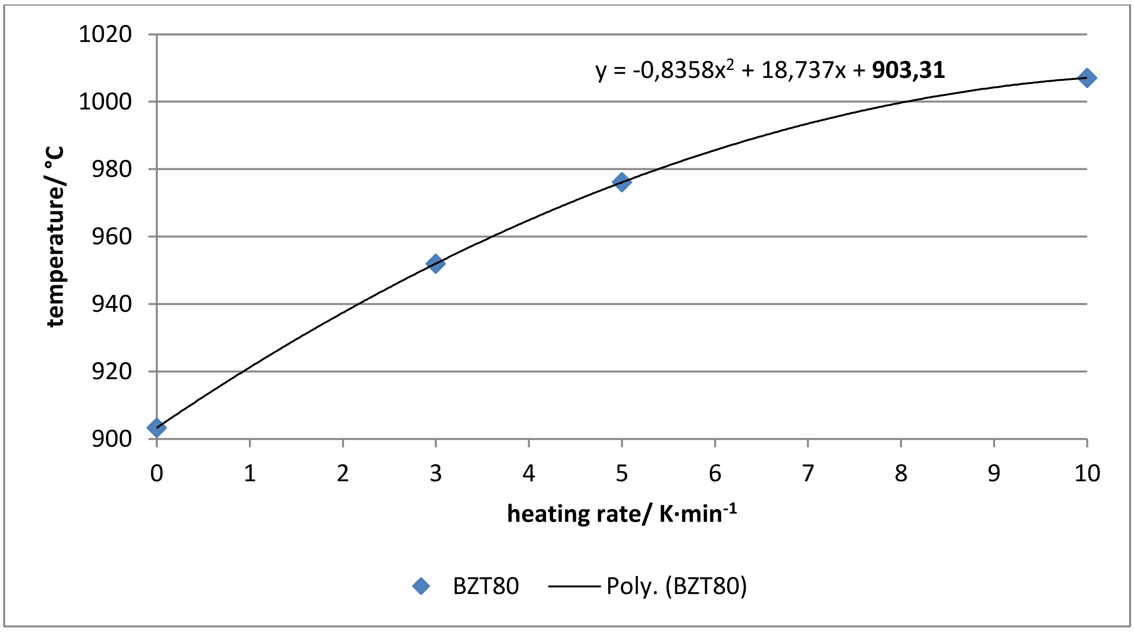

Figure 27: Example for the extrapolation to 0 K/min with the end temperature of BZT80 as example.

The MS program operates secondly with a mass scanning speed of 1 second. The vacuum in the quadrupole MS is 10^{-4} Pa and a multiple ion detector (MID) was used in the measurement. The m/z ratio of 18 (H_2O^+) and 44 (CO_2^+) had been detected.

This measurement includes following data: mass loss, heat capacity and ion currents of H_2O and CO_2. This kind of information is important to give an explanation of the reaction, the enthalpy and of volatile components.

3.2.2 Densitometry and Shrinkage Measurement

As mentioned in the beginning, the theoretical density is determined by the unit cell dimensions through X-ray diffraction.
The geometric dimension was measured through vernier calliper and weighing of the disc shaped samples before and after sintering. The ratio of the apparent density to the theoretical density is the relative density. The relative density gives information about how good the sample is sintered. The relative density should be close to 1, because porous samples show a higher loss factor.

By comparison of the geometric density of the green body and the sintered sample the shrinkage during the sintering process could be estimated.

3.2.3 X-Ray Powder Diffraction and High Temperature X-Ray Diffraction

The measurement equipment was a BRUKER D8 Advance using a Cu K_α radiation source and phases present in the sample has been identified with Panalytics X'Pert High Score Plus software. Furthermore, the ICSD database is used to identify the peaks of the XRD spectrum. The Rietveld refinement was done to estimate the lattice parameters and therefore the cell volume.

X-ray powder diffraction (XRD) is a method to identify the phase of a crystalline material (e.g minerals, inorganic compounds) and provides the unit cell dimensions. Crystals are regular arrays of atoms and X-ray can be distinguished as waves of electromagnetic radiation. The interaction of the sample and the incident beam is determined by the Bragg´sch law.

$$\mathbf{n \cdot \lambda = 2 \cdot d \cdot sin\theta}$$

n... 1,2,3,..
λ... wavelength/nm
d... distance between the lattice plane
θ... bragg angle (angle between the lattice plane and the x-ray)

XRD pattern are used to monitor on the one hand structural properties, as purity and change of symmetry, on the other hand chemical reactions.

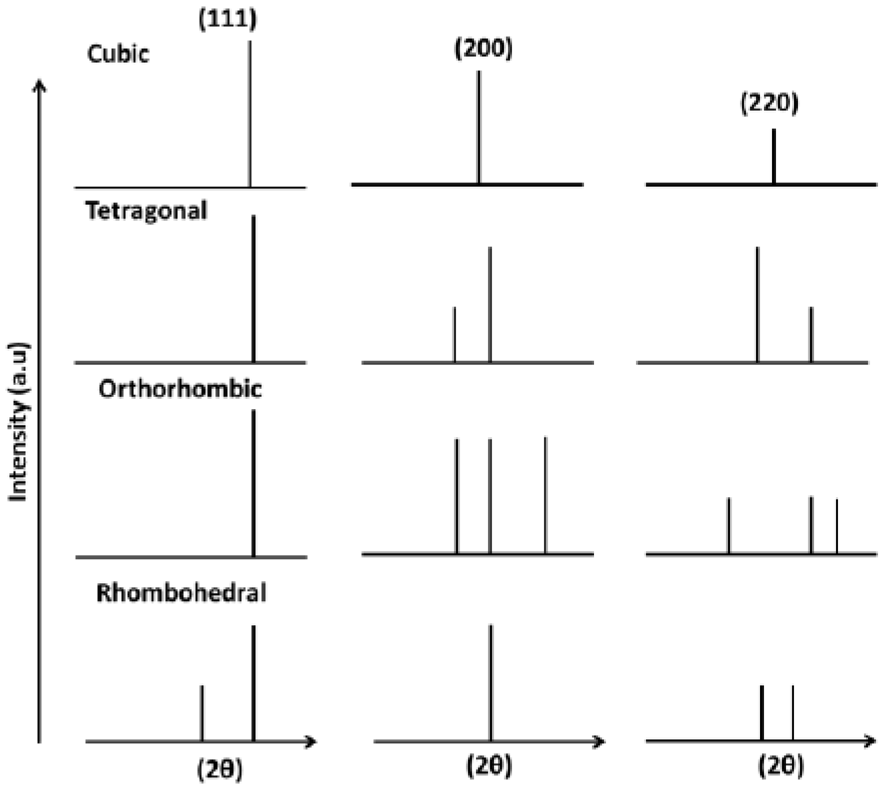

Figure 28: X-Ray diffraction for different symmetries with the reflection (111), (200) and (220)

The calcined and the sintered samples were used for the XRD measurement. The samples were grinded with the agate mortar to get a fine powder before starting the measurement.

The XRD was measured for following samples: $BaZr_{0.20}Ti_{0.80}O_3$, $Ba_{0.80}Ca_{0.20}Zr_{0.20}Ti_{0.80}O_3$, $Ba_{0.80}Ca_{0.20}ZrO_3$, $Ba_{0.94}Ca_{0.06}Zr_{0.20}Ti_{0.80}O_3$ and $BaZr_{0.25}Ti_{0.75}O_3$ at room temperature and 2θ= 10°-100° with 0.02° steps. The received lattice constants are used to calculate the cell volume and therefore the theoretical density of the samples which is calculated with the following formula.

$$\delta_{theo.} = \frac{M \cdot n}{V \cdot N}$$

$\delta_{theo.}$.... theoretical density/ $g \cdot cm^{-3}$

M... molecular weight / $g \cdot mol^{-1}$

n... number of formula units/ 1

V... volume of the elementar cell/ $Å^3$

N... Avogadro number/ $6.022 \cdot 10^{23}$

The HT-XRD was done by X-ray diffraction spectrometer Panalytical XPert Pro MPD equipped with HTK 1200NK (Anton Paar). It studies the material behavior as a function of temperature. Temperature depended XRD for the samples $BaZr_{0.20}Ti_{0.80}O_3$, $Ba_{0.80}Ca_{0.20}Zr_{0.20}Ti_{0.80}O_3$ and $Ba_{0.80}Ca_{0.20}ZrO_3$ were done.

The raw materials were given on a platinum ribbon in a regular thickness and furthermore the platinum ribbon is heated. Through the TG/DSC-MS data the temperature range of ongoing chemical reactions could be estimated.

The onset of the mass degradation is used as the starting temperature. Consequently, the samples were measured from 30°C to 1200°C in 50°C steps. To obtain information about the peaks at lower temperature the starting materials were analysed at room temperature, therefore the reflexes could assign to the different phases.

3.2.4 Impedance Spectroscopy

As mentioned in the beginning the capacity C_p and the loss factor tanδ were measured with an impedance analyzer (Novocontrol Quatro Cryosystem). From the capacity and the geometric measurement, the permittivity ε was calculated. The measurement was done from -50°C to 300°C at different frequencies (1MHz, 100kHz, 10kHz, 1kHz, 100Hz).

For electrical measurement the surfaces of the samples were sputtered with 100 nm gold or painted with silver conductive paste (Leitsilber 200) and dried at 80°C for 45 minutes. Thus the sample can be regarded as a plate capacitor.

The relative permittivity ε_r is the permittivity of a given material relative to that of the permittivity of a vacuum. Also the dielectric loss factor tan δ is an important factor. This dielectric measurement is the amount of electrical energy when voltage is applied.

Therefore, following relationship of a multilayer capacitor is expressed.

$$C = \varepsilon_r \varepsilon_0 \frac{A}{d}(\text{n-1})$$

C... capacitance/ F

ε_r... relative permittivity (for vacuum it is 1)

ε_0... dielectric constant ($\varepsilon_0 \approx 8.854 \cdot 10^{-12}$ F·m^{-1})

A... area between the plates/ m^2

d... separation between the plates/m

n... number of printed electrodes

The frequency and temperature dependence is studied to get information of the relaxor behaviour of the material.

4 Results

The following chapter describes the evaluation of the used methods and the material properties.

The materials BZT80, BZT75, BZT45, BCZ80, BCZT80, and BCZT94 are discussed in detail with focus on the forming reaction mechanisms and their secondary phases.

4.1 Characterization of $BaZr_{0.20}Ti_{0.80}O_3$ and $BaZr_{0.25}Ti_{0.75}O_3$

Barium zirconate titanate [$Ba(Zr_xTi_{1-x})O_3$] ceramics are good candidates for multilayer ceramic capacitors (MLCC) due to their high dielectric properties and low dielectric losses. In recent years the electric properties are studied in a broad range. However, the work focuses on temperature and frequency dependence as well as the phase transitions and therefore the association of the ferroelectric relaxor behaviour. [71,54]

The chapter contains the $Ba(Zr_xTi_{1-x})O_3$ synthesis where x= 0.20 (BZT80) and x=0.25 (BZT75). The samples are prepared via mixed oxide route where the calcination is done at 1250°C and the sintering at 1400°C.

4.1.1 Thermal Analysis

The measurement shows the mass loss in a defined temperature range. Additionally, the emanation of CO_2 and water vapour has been detected by coupled mass spectrometry, which is shown in Figure 29.

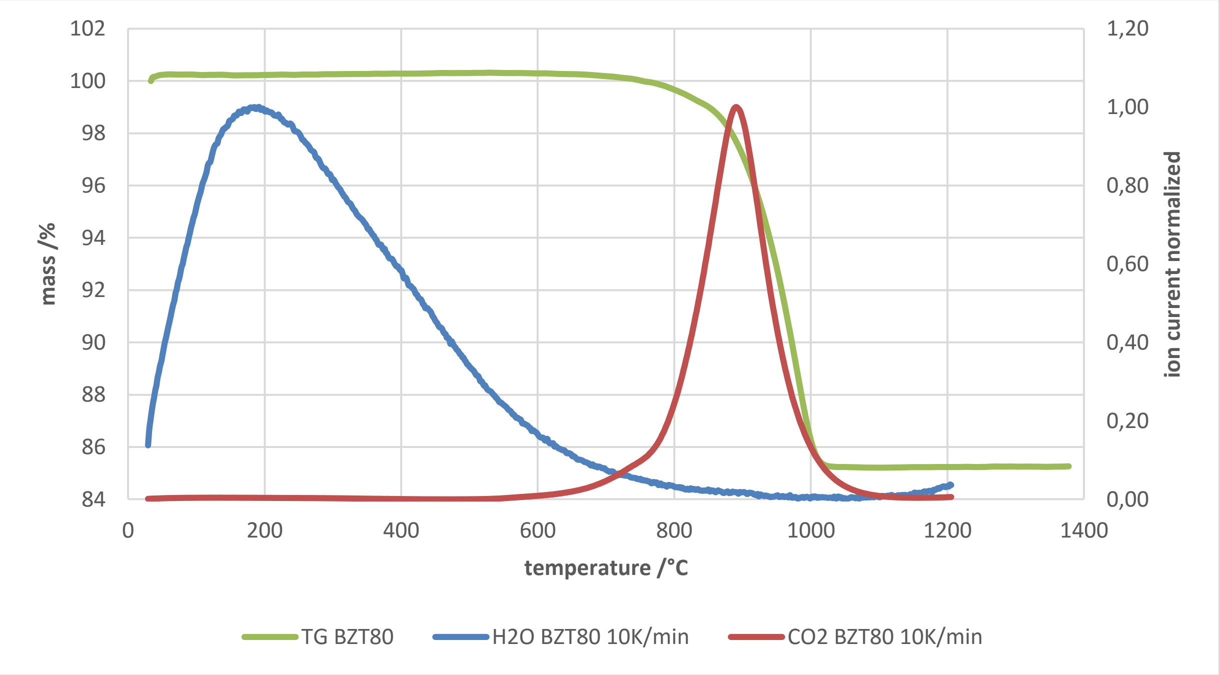

Figure 29: TG-MS of BZT80 with a heating rate of 10K/min.

The starting and end temperature of the thermogravimetry is shifted to higher temperatures with increased heating rate as seen in Figure 30. Furthermore, the CO_2 mass curve is shifted to lower temperatures by decreasing the heating rate from 10K/min to 3K/min.

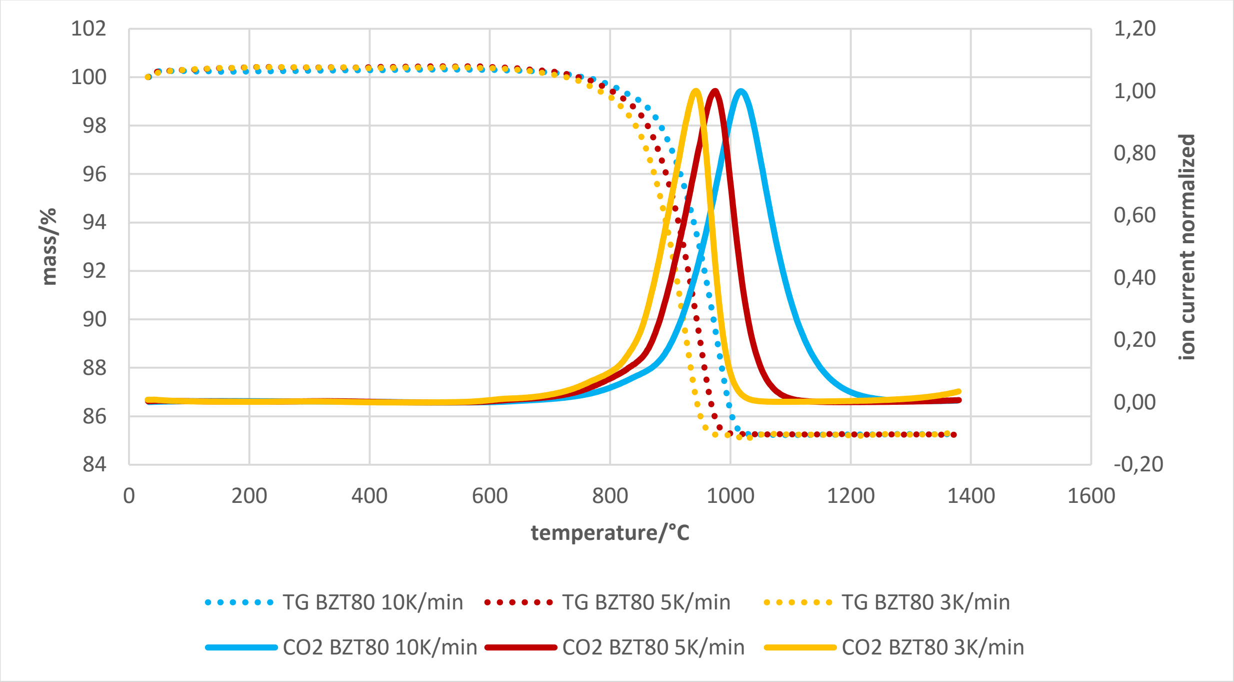

Figure 30: TG-MS of BZT80 for different heating rates (extrapolated end temperature: 903°C).

The results of BZT80 and BZT75 are similar but by changing the concentration of titanium from 80% to 45% ($BaZr_{0.55}Ti_{0.45}O_3$) results in a shift of thermal analysis. The mass loss of BZT45 is smaller (blue dashed line) and the end temperature is higher compared to BZT80/BZT75. In Figure 31 the difference is represented.

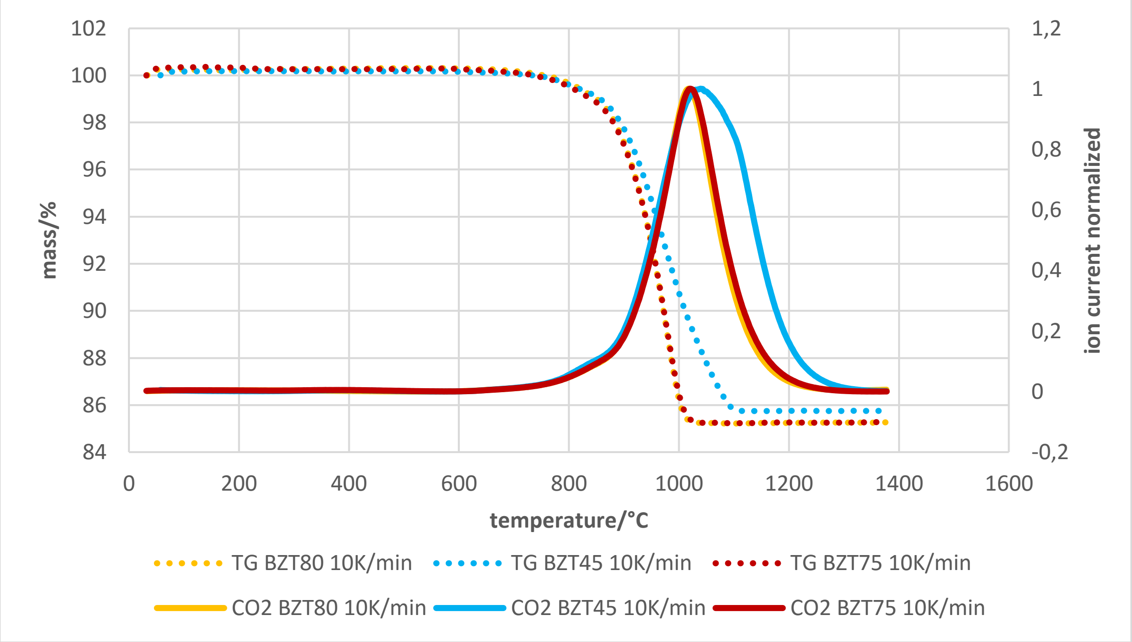

Figure 31: TG-MS of BZT80 (yellow), BZT75 (red) and BZT45 (blue) with different concentrations.

In Figure 32 it can be seen, that the BZT mixtures react gradually meaning that there is a mass loss (black curve) in two steps with the first onset temperature at 649.1°C and the second at 913.9°C. The first mass loss is barely visible, but the CO_2 mass curve (pink) visualizes a shoulder at approximately 915°C, which correlates with the first mass loss in the thermogravimetry. The first reaction takes place at 649.1°C with a mass loss of 0.98% and the second at 913.9°C with a mass loss of 14.05% which is associated with the highest CO_2 discharge.

The typical thermal decomposition is illustrated in Figure 32. It shows two endothermic peaks at 834.8°C and 984.9°C. The mass curve of water has no influence on the reaction because it takes place at temperatures below 200°C.

The peak at 834.8°C corresponds to the transition of $BaCO_3$ from the orthorhombic crystal structure to the trigonal one. Therefore, a sharp peak can be observed in the DSC curve (blue). The broad peak at 984.9°C describes an endothermic formation of $BaCO_3$ due to the CO_2 loss in that temperature range. It can be mentioned that more reactions are taking place due to the broadness of the peak.

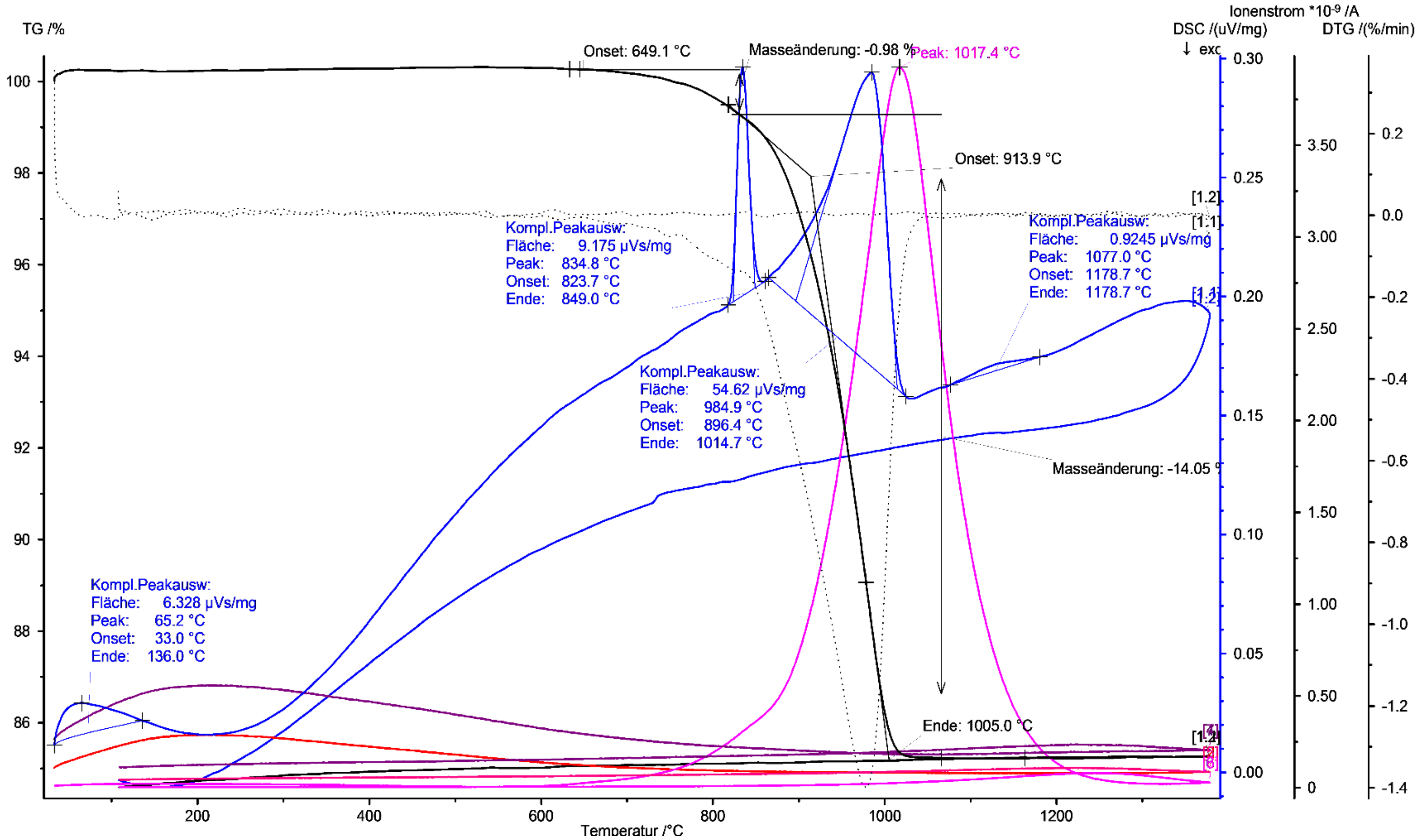

Figure 32: TG/DSC-MS for the BZT80 sample at 10 K/min.

To make an allocation of the peaks a high temperature XRD is done which is described in the following chapter.

4.1.2 High Temperature X-Ray Diffraction

Figure 33 to Figure 35 show the high temperature XRD patterns of $Ba(Zr_{20}Ti_{80})O_3$ ceramics. It can be seen that at room temperature only the initial compounds are existing. Increasing the temperature to 600°C the peaks at 2θ=27°-28° and 33°-34° are changing. This peaks are unidentified. Furthermore, at 800°C the most acidic compound TiO_2 reacts with $BaCO_3$ to form $BaTiO_3$. Afterwards at 950°C the secondary phase Ba_2TiO_4 is observed. The remaining Ti^{4+} reacts to the secondary phase and further to the $Ba(Zr,Ti)O_3$. Between 1100°C and 1200°C the amount of the secondary phase decreases rapidly because it is reacting with the ZrO_2 to form $Ba(Zr,Ti)O_3$. Therefore, two perovskite phases are formed with different Zr/Ti ratio, as seen in Figure 35 at 1200°C (BZT and $BaZrO_3$). The peak of $BaZrO_3$ is visualized at 1100°C at 2θ=29.8°, 43°, 49.6° and 53°.

So following reaction takes place.

$$BaCO_3 + TiO_2 \xrightarrow{\text{800-1050°C}} BaTiO_3 + CO_2\uparrow$$

$$BaCO_3 + BaTiO_3 \xrightarrow{\text{850°C-1150°C}} Ba_2TiO_4 + CO_2\uparrow$$

$$Ba_2TiO_4 + ZrO_2 \xrightarrow{\text{1100°C-1200°C}} BaZrO_3 + BaTiO_3$$

$$(1-x)BaTiO_3 + xBaZrO_3 \xrightarrow{\text{starts at 1200°C}} BaZr_xTi_{1-x}O_3$$

Equation 25: Forming reaction for BZT80.

$BaTiO_3$ and $BaZrO_3$ are formed separately and by interdiffusion the BZT component is formed. The secondary phase Ba_2TiO_4 is only observed in the temperature range from 950°C to 1150°C through the reaction of $BaCO_3$ and $BaTiO_3$.

At 850°C the formation of $BaCO_3$ from orthorhombic phase to trigonal phase is taking place, which is shown due to the shifting of the $BaCO_3$ peaks, for example from 2θ=23° to 2θ=21°. However, two perovskite phases with different Zr/Ti ratio are formed.

From 900°C to 1050°C the quantity of $BaTiO_3$ increases slowly with decreasing of $BaCO_3$ and TiO_2 reactants.

The quantity of $BaZrO_3$ is always lower than that of $BaTiO_3$ at any temperature up to 1200°C. At 1050°C the amount of $BaTiO_3$ starts decreasing quickly and the amount of $BaZrO_3$ and

$Ba(Zr,Ti)O_3$ are increasing rapidly. The perovskite phase is formed at 1100°C and furthermore the $Ba(Zr,Ti)O_3$ amount increases rapidly up to 1200°C.

At 1200°C BZT is detected but there is also a small amount of $BaZrO_3$ which has not been reacting yet.

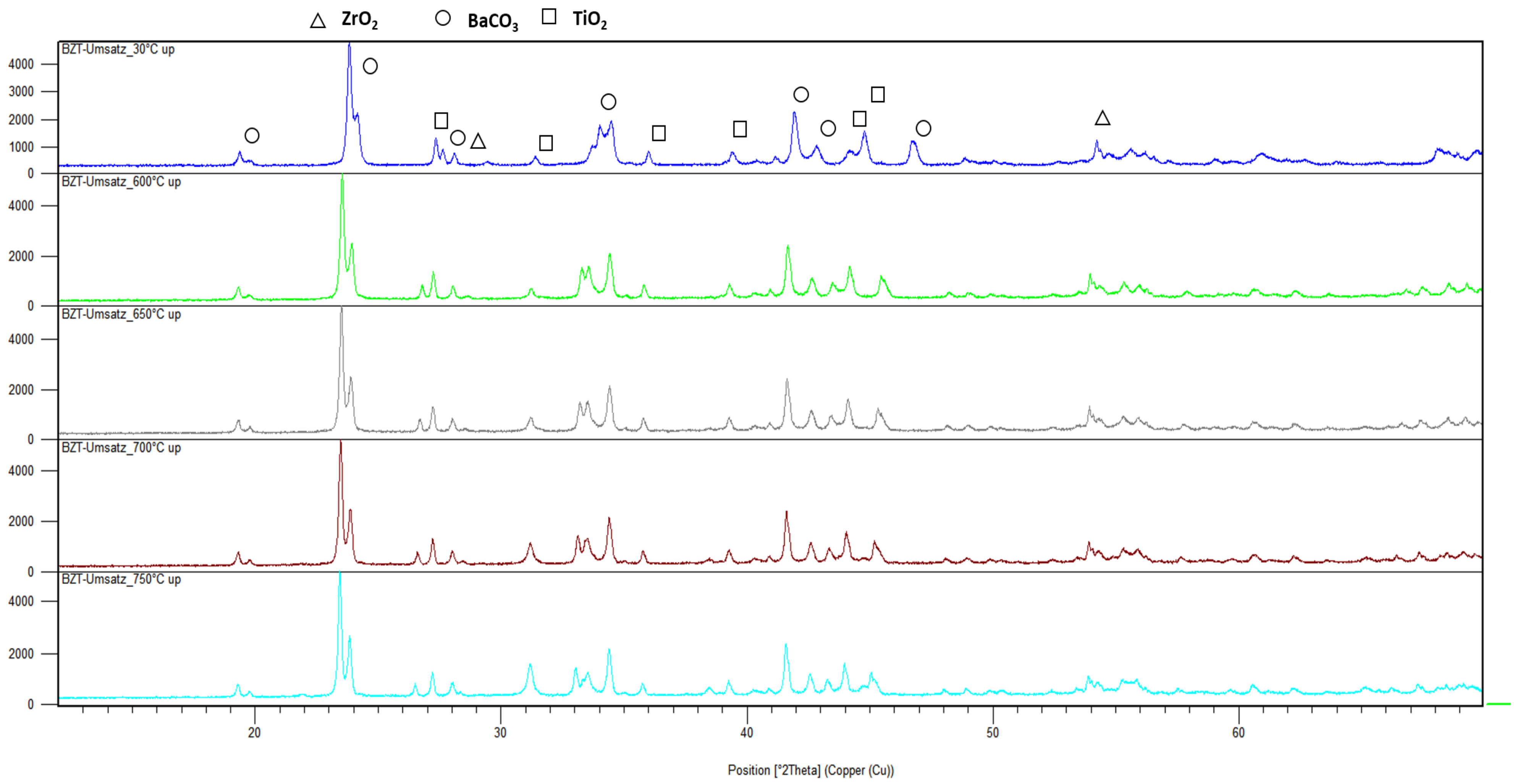

Figure 33: High temperature XRD pattern from 30°C to 750°C for $BaCO_3$, ZrO_2 and TiO_2. From room temperature to 600°C.

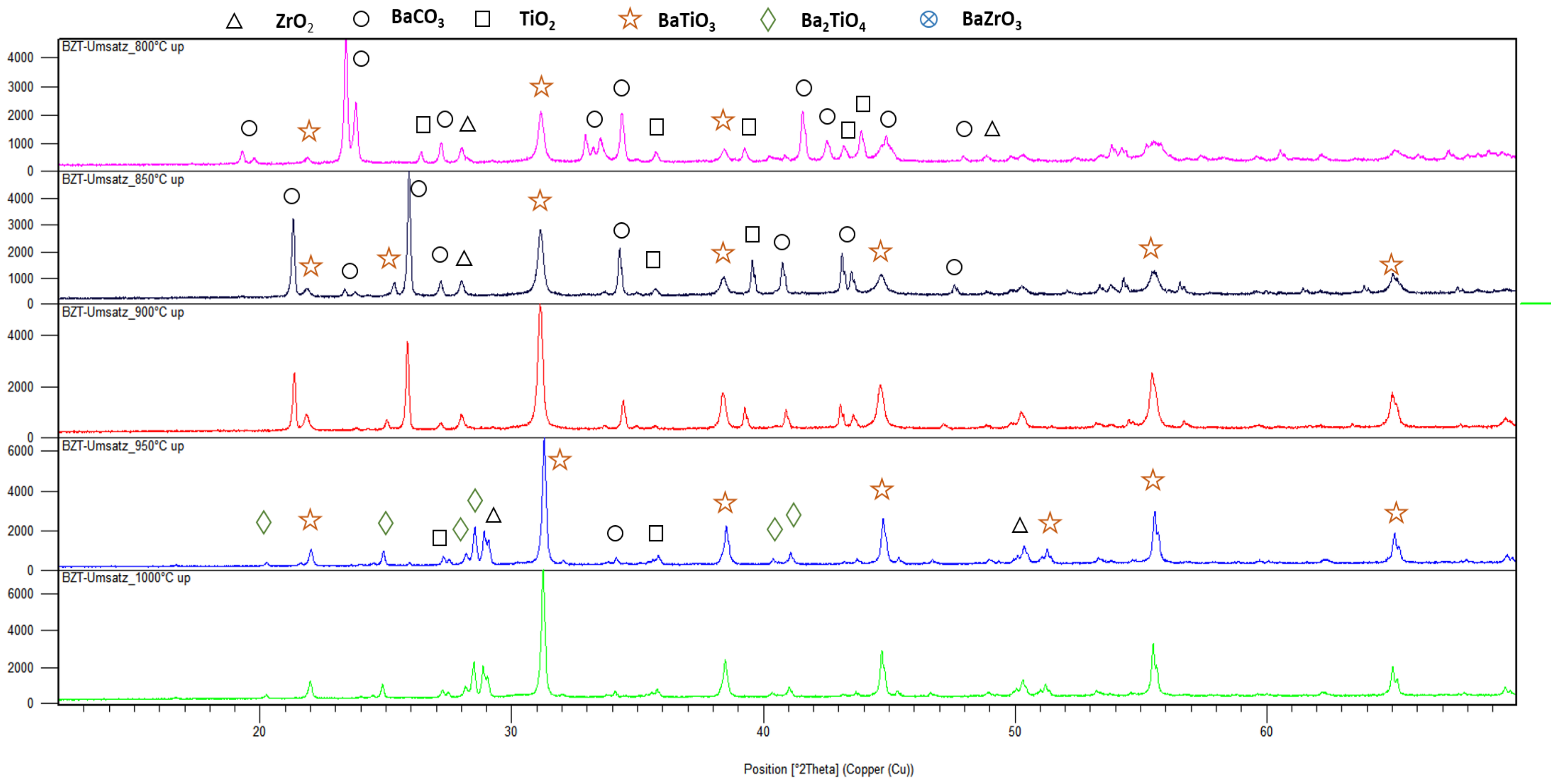

Figure 34: High temperature XRD from 800°C to 1000°C. A secondary phase is observed from 950°C to 1000°C which reacts later on with Zr^{4+} to $BaZrO_3$.

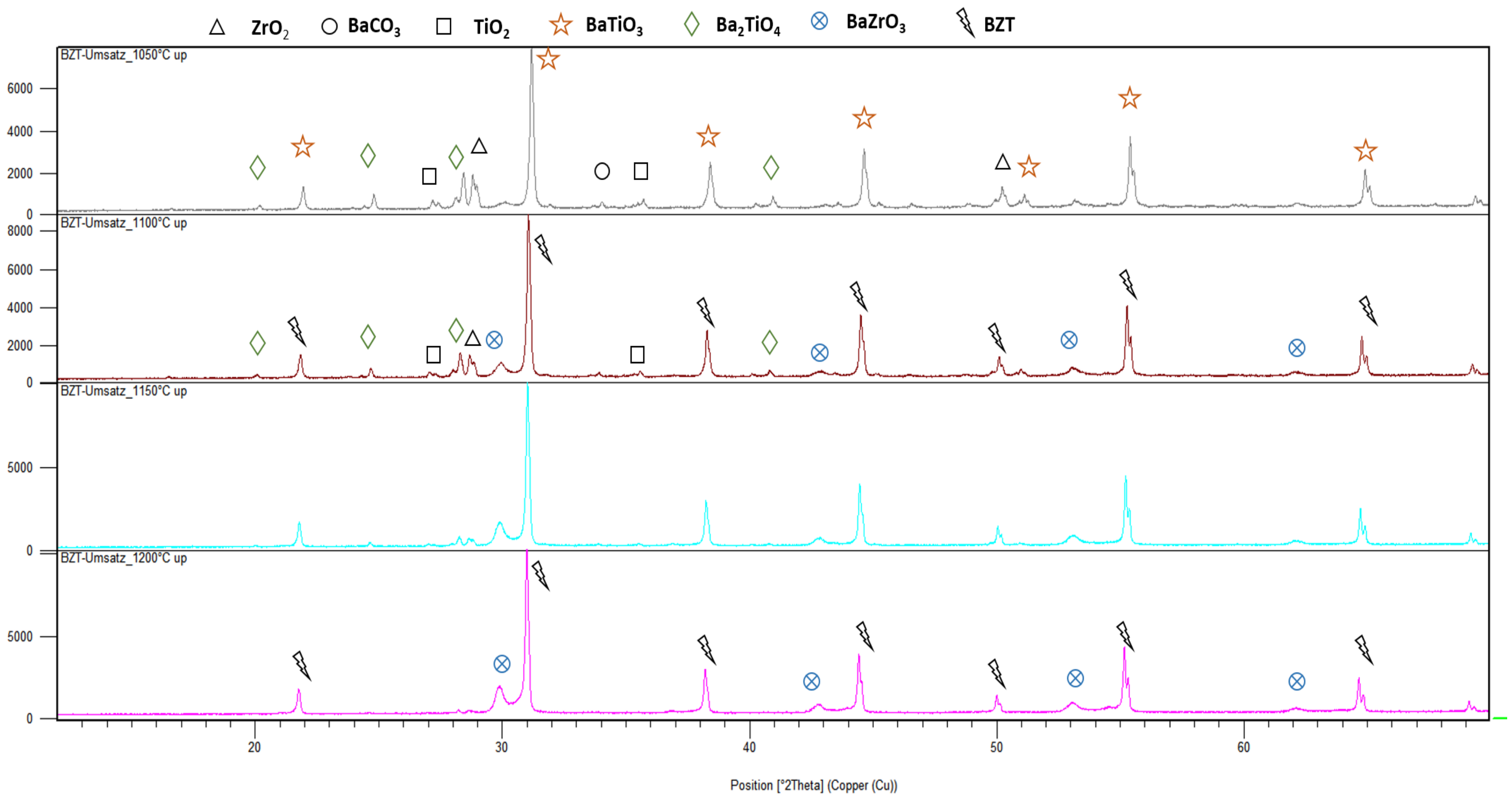

Figure 35: High temperature XRD pattern from 1050°C to 1200°C. The secondary phase Ba_2TiO_4 is observed up to 1100°C. Two perovskite phases of BZT and $BaZrO_3$ are formed.

4.1.3 X-Ray Diffraction

The X-ray diffraction pattern of calcined and sintered BZT80 is shown in the Figure 36. It can be observed that a single phase perovskite structure is formed after calcinations at 1250°C and no impurity phases are detected.

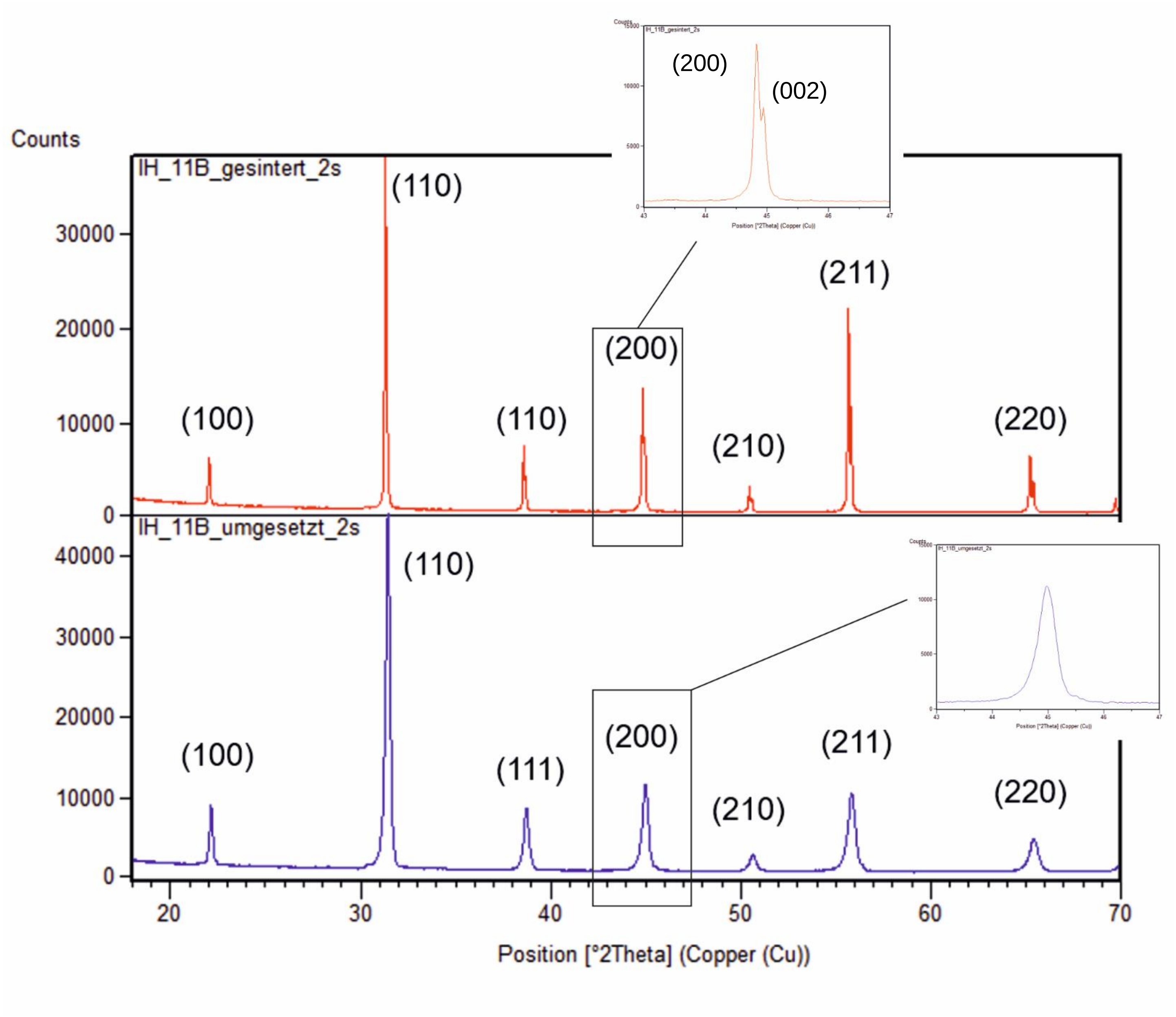

Figure 36: XRD pattern for calcined (blue) and sintered (red) BZT80, which indicates a single phase perovskite structure. The calcined sample shows a pseudocubic structure whereas the sintered sample indicates a tetragonal phase due to the splitting peak (200).

All the compositions of BZT80 and BZT75 show a pure perovskite structure without any secondary phases after calcination. This is an indication of an isovalent substitution of Ti^{4+} by Zr^{4+} to form a homogeneous solution. With increasing zirconium content, the tetragonal phase is more pronounced. The peaks are shifted to lower angles with higher zirconium content as seen in Figure 37.

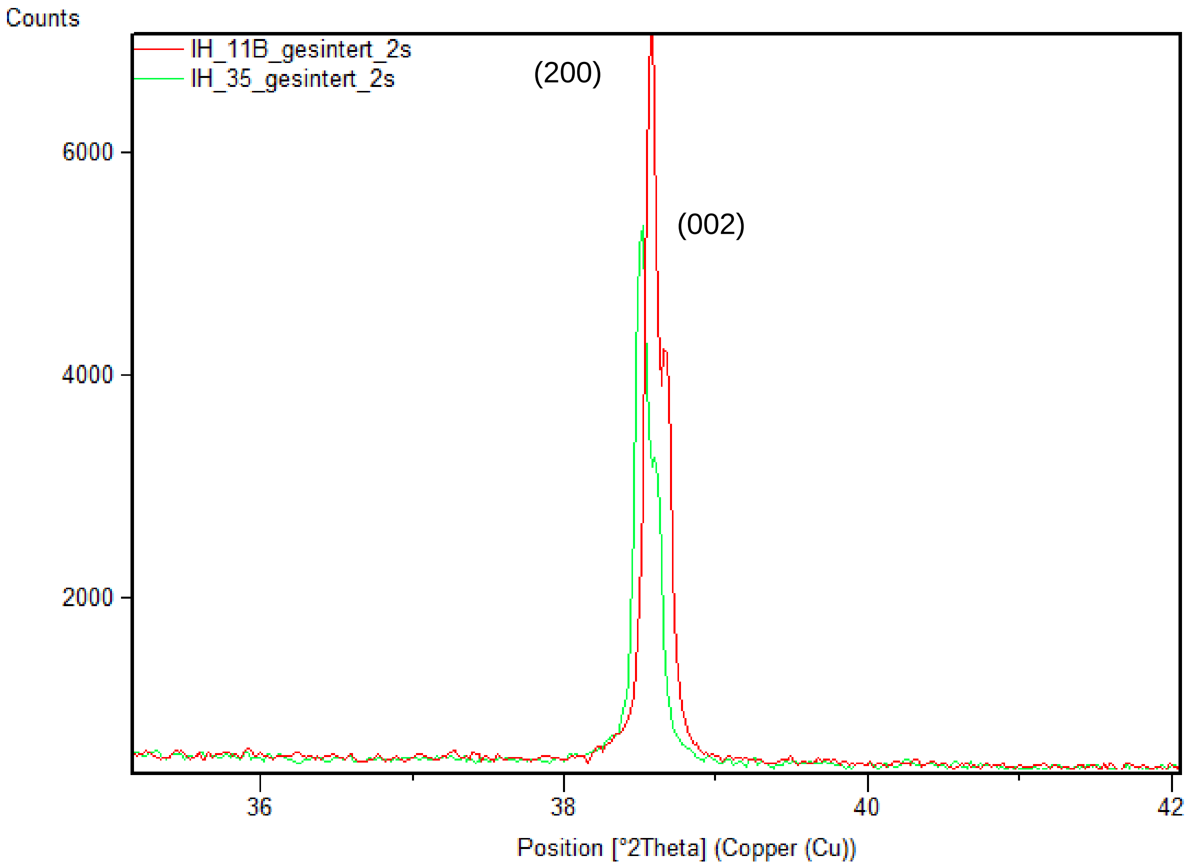

Figure 37: Shifting XRD pattern of sintered BZT80 (red) and sintered BZT75 (green).

In literature it is reported that that BZT ceramics have a tetragonal, orthorhombic, rhombohedral or cubic structure at room temperature. [55,3]

The BZT80 and BZT75 both show a pseudocubic structure after calcination at 1250°C. After sintering at 1400°C a tetragonal structure is received.

The splitting diffraction peaks of (200) and (002) shown in Figure 37 confirm the tetragonal phase. Besides the position shift the sintered samples also show a decreasing effect of the tetragonality with increasing zirconium content.

The lattice parameters of the ceramics are also increasing with increasing zirconium content because the ionic radius of Zr^{4+} (0.72Å) is larger than that of Ti^{4+} (0.61Å). Thus, also the cell volume of the BZT75 ceramic is increasing.

Table 4: Lattice parameters of the sintered pseudo cubic (a=b≠c and α=β=γ≠90°) BZT ceramics.

Composition	**Crystal system**	**a (Å)**	**c (Å)**	**Cell volume ($Å^3$)**
BZT80	tetragonal	4.0464	4.0511	66.33
BZT75	tetragonal	4.0544	4.0564	66.68

4.1.4 Densification and Shrinkage

The volume shrinkage of the samples is higher than 30% and the length and diameter shrinkage is between 7% and 15%.

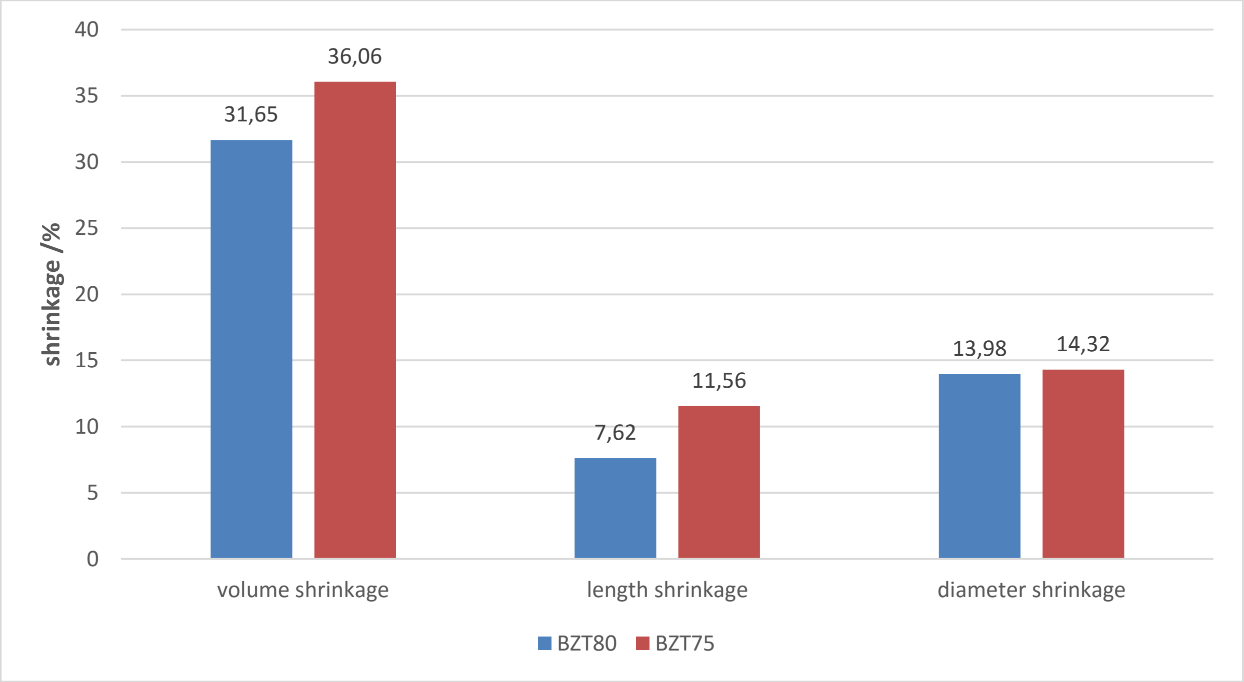

Figure 38: Shrinkage values from the geometric density of the green body in relation to the sintered samples, compared for BZT80 and BZT75 ceramics.

With increasing zirconium content, the shrinkage value is also increasing. This indicates that the sintering process is influenced by the Zr^{4+}/Ti^{4+} ratio.

As mentioned in the beginning the relative density is given by dividing the calculated density by the theoretical density.

$$\delta_{relative} = \frac{\delta_{calculated}}{\delta_{theoretical}}$$

$\delta_{calculated}$ … calculated value of the vernier caliper measurments /g·cm^{-3}

$\delta_{theoretical}$… results of the X-ray diffraction / g·cm^{-3}

The results of the density calculation are shown in the following table.

Table 5: Calculation of the relative density.

Composition	**Calculated density/ g·cm^{-3}**	**Theoretical density/ g·cm^{-3}**	**Relative density/ %**
BZT80	5.15	6.06	84.99
BZT75	5.22	6.10	85.59

Benabdallah et al reported that it is difficult to reach a relative density of more than 90% in BZT-BCT ceramics.[40] Hence a relative density of 84.99% for BZT80 and 85.59% for BZT75 are acceptable results for samples prepared via mixed oxide route.

4.1.5 Dielectric Properties

The figure below shows the relative permittivity at room temperature as a function of the frequency (1 MHz to 100Hz). The relative permittivity is decreasing with increasing zirconium content. The BZT80 ceramic has a permittivity of 12000 at room temperature whereas BZT75 only has 4000. Furthermore, a continuous fall with increasing frequency is observed.

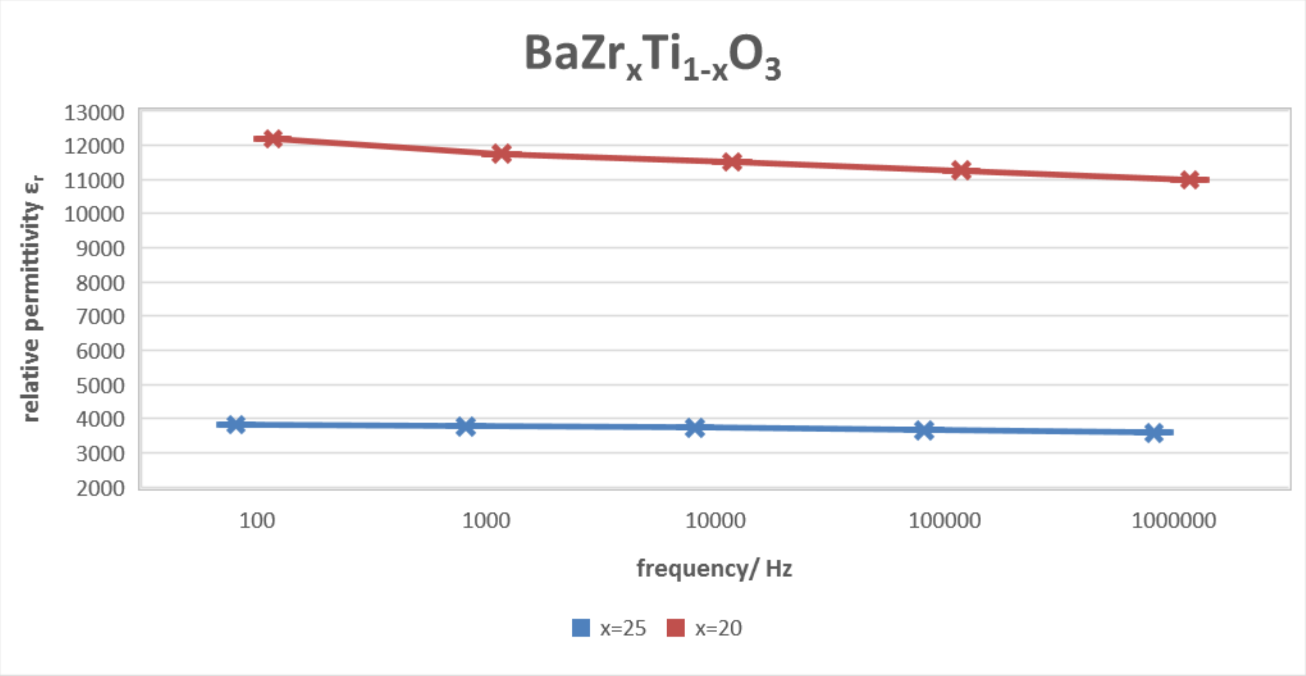

Figure 39: Dielectric permittivity as function of frequency for BZT80 and BZT75.

The temperature dependence of BZT ceramics with different frequencies is shown in Figure 40 and in Figure 41. The relaxor behavior is more obvious for BZT75 due to the shifting of the temperature maximum T_m (Figure 41). The BZT80 ceramic shows no shifting of the T_m as seen in Figure 40.

With increasing frequency, the temperature maximum T_m is shifted to higher temperatures and the relative permittivity is decreasing.

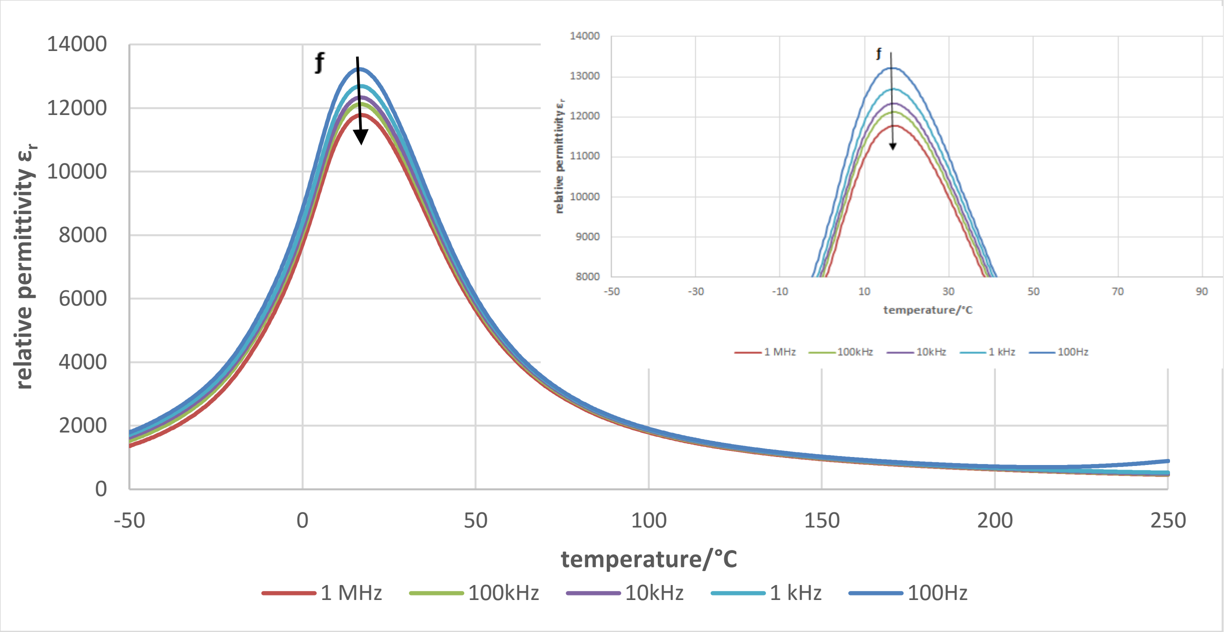

Figure 40: Temperature dependence of relative permittivity measured with different frequencies for BZT80 ceramic.

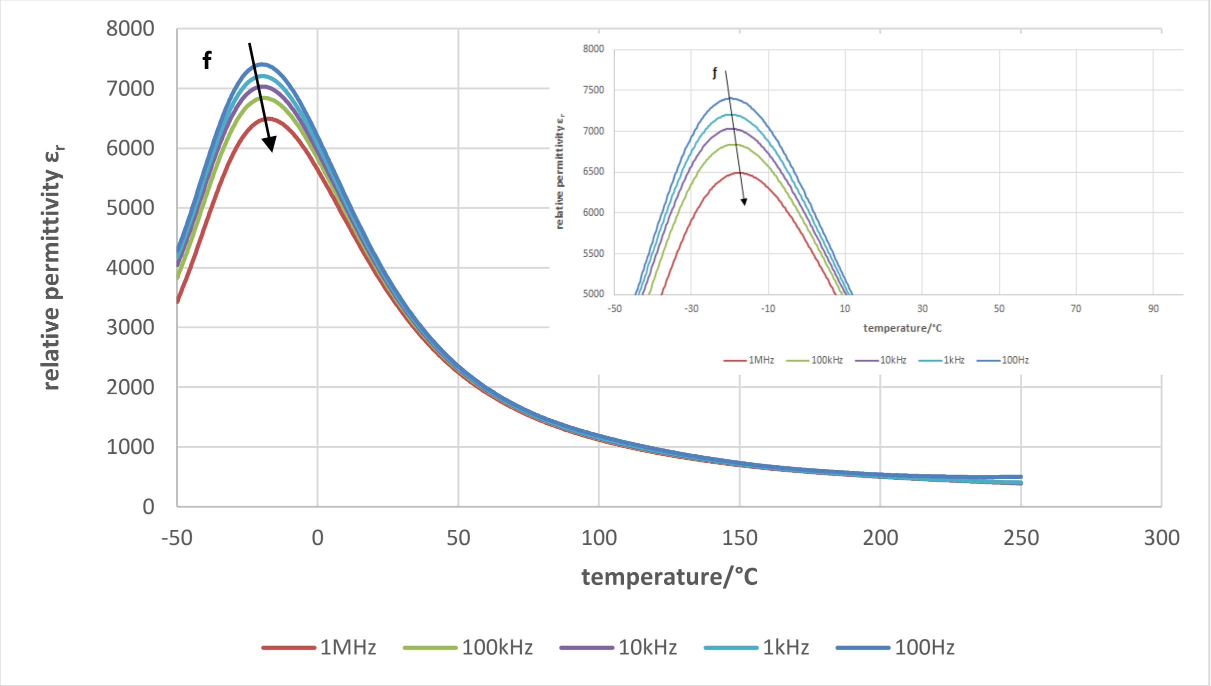

Figure 41: Temperature dependence of relative permittivity measured with different frequencies for BZT75 ceramic.

The samples BZT80 and BZT75 have high relative permittivity but rather low dielectric losses. From -50°C to 150°C the dielectric losses are smaller than 10%, by increasing the temperature the loss factor is also increasing, which indicates a thermally activated loss mechanism.

The relative permittivity of BZT75 is lower than that of BZT80 resulting from an increasing Zr^{4+} content. In contrast to Ti^{4+}, Zr^{4+} has a higher ionic radius concluding in lower maximum temperature (T_m). The interactions between the O^{2-} and the B-site ion become weaker and thus additionally decrease the T_m. [72] Also the crystal structure is changing with different Zr^{4+} concentrations.

Furthermore, the peaks become wider with higher Zr^{4+} content which indicates the phase transition from ferroelectric to paraelectric state or better a diffuse ferroelectric state. [73,74]

To describe the diffuseness of the phase transition the Curie-Weiss law is used.

$$\frac{1}{\varepsilon} - \frac{1}{\varepsilon_m} = \frac{(T - T_m)^\gamma}{C}$$

ε...	relative permittivity
ε_m...	maximum relative permittivity
T…	temperature
T_m…	temperature to the maximum relative permittivity
C…	Curie constant
γ …	diffuseness constant

The diffuseness constant describes the character of the phase transition. An ideal ferroelectric material has γ=1 whereas a ferroelectric relaxor material has γ=2. [74]

The function of log(T-T_m) plotted against log(1/ε-1/ε_m) at a frequency of 1kHz is displayed in the Figure 42.

The diffusion shows a linear relationship in BZT ceramics and the γ varies between 1.71 for BZT80 and 1.82 for BZT75. In the BZT75 the relaxor behaviour is more emphasized because of the higher diffuseness constant, which is close to the ideal value of 2.

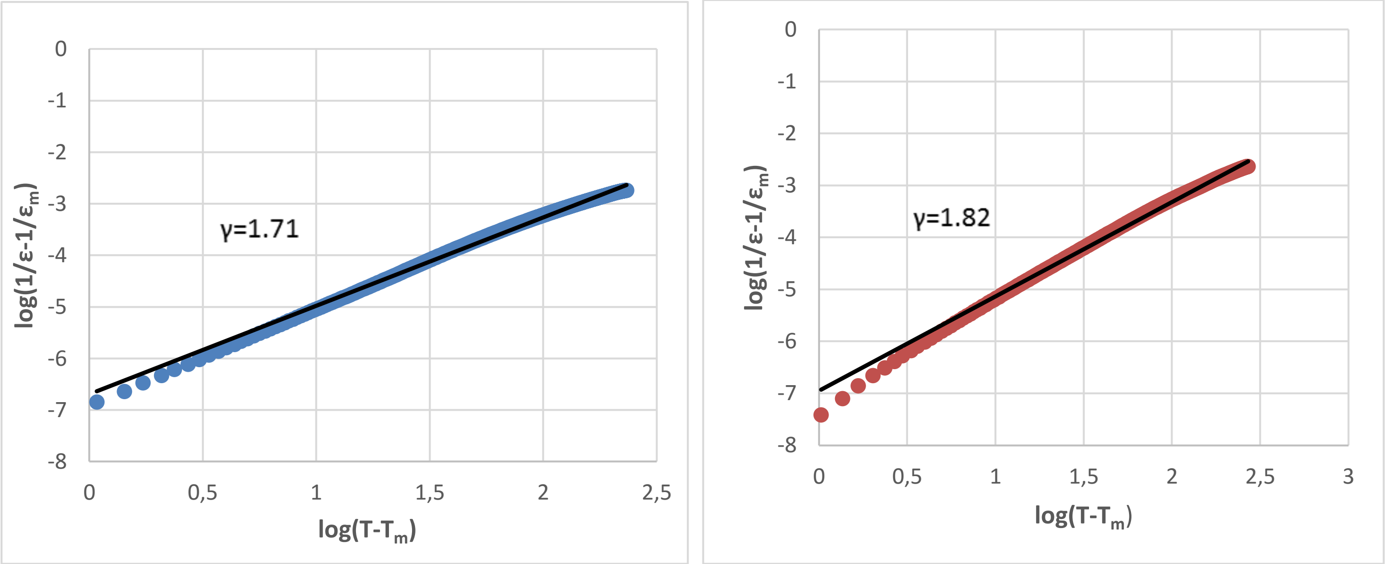

Figure 42: Plot of the diffuseness constant of BZT80 (blue) and BZT75 (red) to show the relaxor behaviour.

4.2 Characterization of $Ba_{0.80}Ca_{0.20}Zr_{0.20}Ti_{0.80}O_3$ and $Ba_{0.94}Ca_{0.06}Zr_{0.20}Ti_{0.80}O_3$

This chapter provides the (Ba_xCa_{1-x}) $(Zr_{0.20}Ti_{0.80})O_3$ synthesis where x=0.80 (BCZT80) and x=0.94 (BCZT94). The samples were prepared in the same way as described in the previous chapter.

Examination of the forming reaction, structure determination, dielectric properties and density measurement are documented in this chapter. The focus is on the forming reaction of the BCZT80 ceramic through high temperature XRD.

The effect of Ca^{2+} and Zr^{4+} substitution on $BaTiO_3$ is reported. Furthermore, BCZT80 and BCZT94 are compared to the BZT samples.

4.2.1 Thermal Analysis

As already mentioned in the chapter 4.1.1 the CO_2 mass curve is shifted to lower temperatures by decreasing the heating rate from 10K/min to 3K/min. Also the starting and the end temperature of the thermogravimetry is shifted to higher temperatures with increasing heating rate.

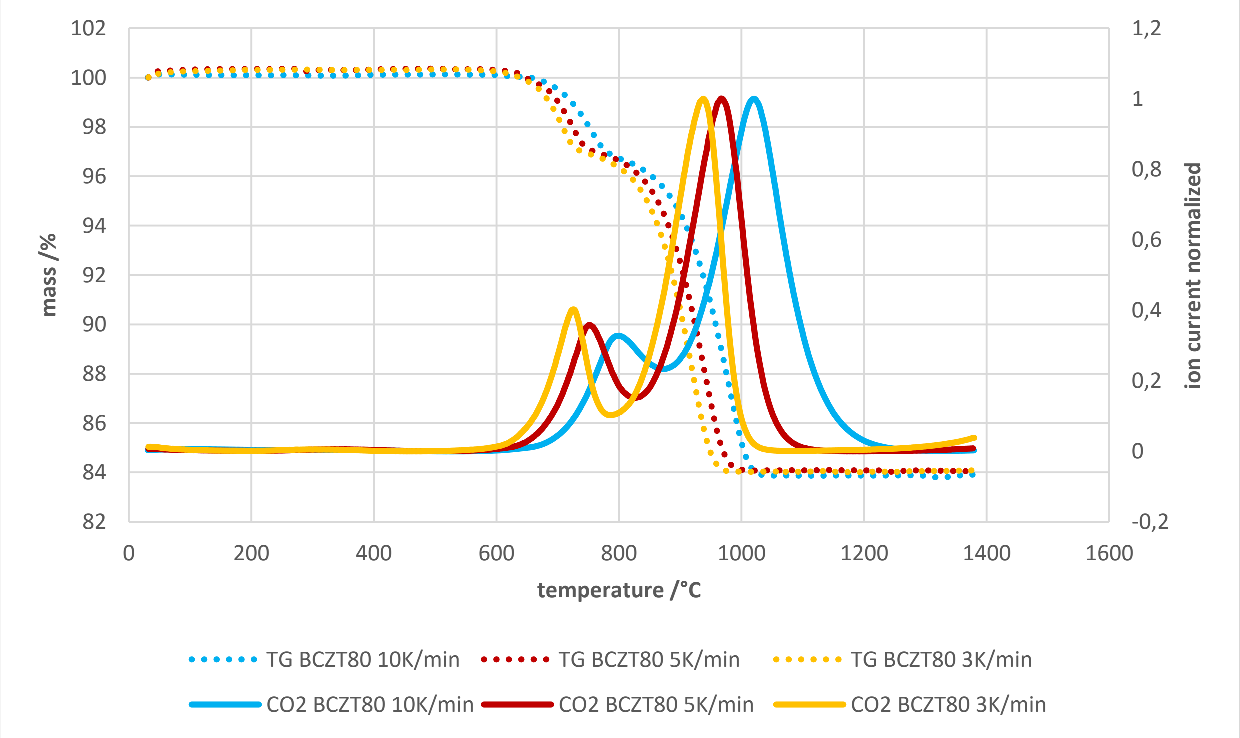

Figure 43: TG-MS of BCZT80 with different heating rates. The extrapolated end temperature is calculated with 916°C.

In contrast to the BZT ceramics, the BCZT ceramics show a minimal difference in the two mass loss steps by changing the heating rate. With decreasing heating rate, the first mass loss decreases and the second increases as seen in the table below.

Table 6: Mass loss at different heating rates for BCZT80

Heating rate	1st mass loss	2nd mass loss
10 K/min	3.50	12.75
5 K/min	3.44	12.80
3 K/min	3.40	12.84

In Figure 44 the thermogravimetry curve (black) of BCZT80 shows a gradually meaning of mass loss in two steps. Additionally, the decomposition of carbonates and emanation of water are visualized through mass spectrometry. The first reaction takes place with a CO_2 loss of 3.49% with an onset temperature of 699.7°C and the second of 12.75% with an onset temperature of 912.6°C which is associated with the highest CO_2 discharge.

Furthermore, the DSC curve (blue) shows 3 endothermic peaks. The first peak at 760.9°C shows that $CaCO_3$ is decomposed and it is part of the further reaction. The peak at 828.6°C corresponds to the transition of $BaCO_3$ from the orthorhombic crystal structure to the trigonal phase.

Finally, the very small broad peak at 1077.1°C corresponds to the formation of the perovskite phase.

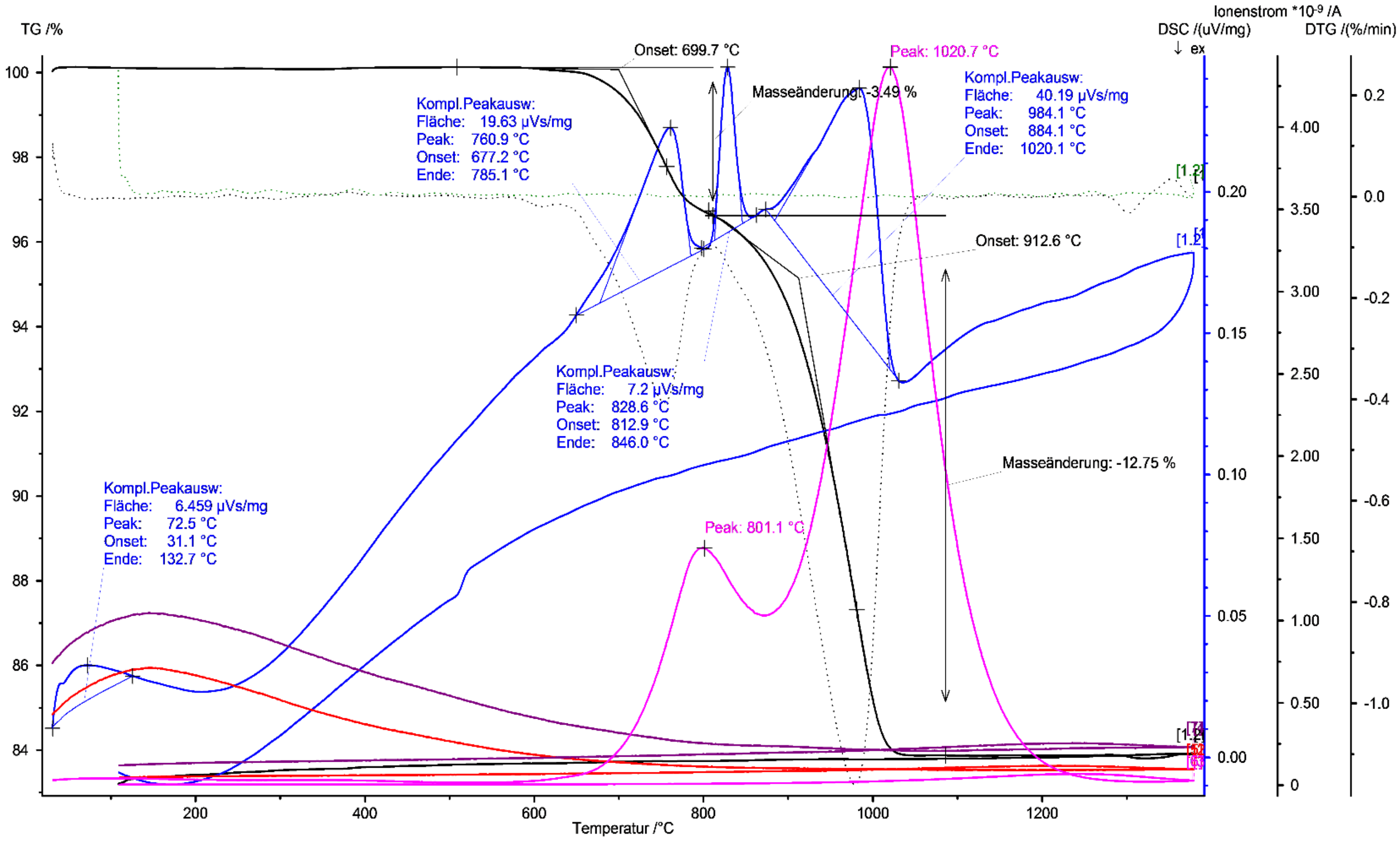

Figure 44: TG/DSC-MS of the BCZT80 ceramic with 10 K/min

In the DSC curve of BCZT94 only the $CaCO_3$ peak at 760.9°C is getting smaller due to decreasing Ca^{2+} concentration, all the other peaks remain the same as in Figure 44. If the BCZT80, BCZT94 and the BZT80 ceramics are compared, the increasing amount of Ca^{2+} also causes a higher mass loss.

The results of BCZT80 and BCZT94 show a difference in the mass loss and also the end temperature is different. The end temperature of BCZT80 is determined with 1011.1°C and BCZT94 with 1003.9°C. As seen in Figure 45 the mass loss is decreasing with decreasing calcium content. Also the first mass loss is getting smaller and without Ca^{2+} content the first mass loss is barely visible. Therefore, it is important to consider the CO_2 mass curve because it shows that there is actually an early mass loss.

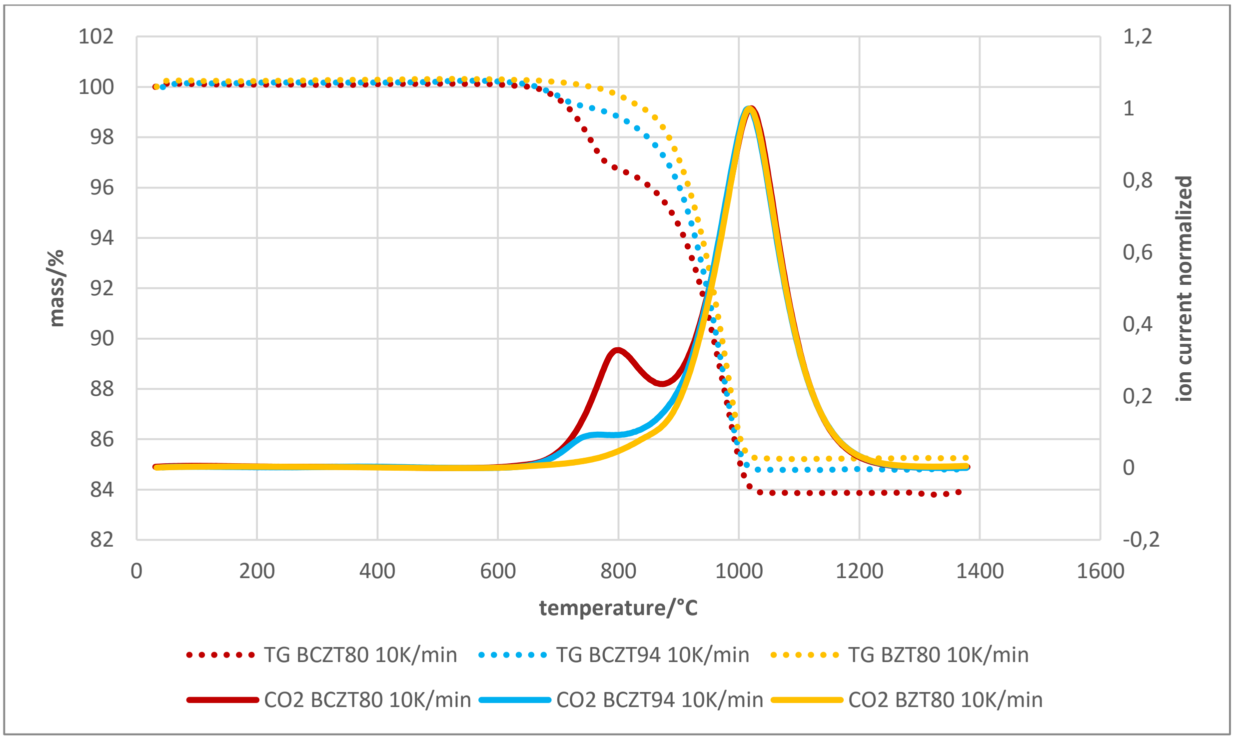

Figure 45: TG-MS curve of BCZT80 (red), BCZT94 (blue) and BZT80 (yellow) ceramics. With decreasing Ca^{2+} content the mass is also decreasing.

4.2.2 High Temperature X-Ray Diffraction

Figure 47 to Figure 49 show the high temperature XRD patterns of the mixture $BaCO_3$, $CaCO_3$, TiO_2 and ZrO_2 ball milled for 1 hour. In the first pattern at room temperature the diffraction peaks are all attributed to the initial components.

At 600°C the reaction starts by forming the secondary phase $CaZr_4O_9$ through CO_2 loss as seen in the TG/DSC-MS. The first endothermic peak in the STA-MS indicates the reaction of

$CaCO_3$ and ZrO_2 to the secondary phase $CaZr_4O_9$. In the high temperature XRD it is displayed between 2θ=32°-33°as a broad peak group and at 2θ= 45°.

Furthermore, at 850°C $CaCO_3$ and TiO_2 are starting to react and form $CaTiO_3$ at 2θ=20.5°,40.8° and 42°. The peak of $CaTiO_3$ is increasing rapidly up to 950°C and at 900°C a secondary phase is formed with the compound $BaTiO_3$, the remaining TiO_2 and $CaCO_3$.

Further at 850°C the formation of $BaCO_3$ from orthorhombic (space group: Pm3m) to trigonal (space group: R3mH) phase is taking place which is seen in a sharp endothermic peak of the DSC curve at 828.8°C. The peak of trigonal $BaCO_3$ decreases rapidly hence $BaTiO_3$ is being formed at 950°C (2θ=22° and 38.5°).

From 850°C to 900°C the ZrO_2 content is decreasing and Ba_2ZrO_4 is formed at 950°C. Furthermore, at 950°C at 2θ=38.6° the broad peak indicates two overlapping peaks of $BaTiO_3$ and Ba_2ZrO_4. They are reacting slowly up to 1100°C and form $Ba(Zr,Ti)O_3$.

At 900°C a broad peak at 2θ=31.5° and 55.5° indicates two overlapping peaks corresponding to $Ba(Zr,Ti)O_3$ and $CaZrO_3$. The $CaZrO_3$ content is decreasing whereas the BZT is increasing until no $CaZrO_3$ is left which is shown in Figure 46.

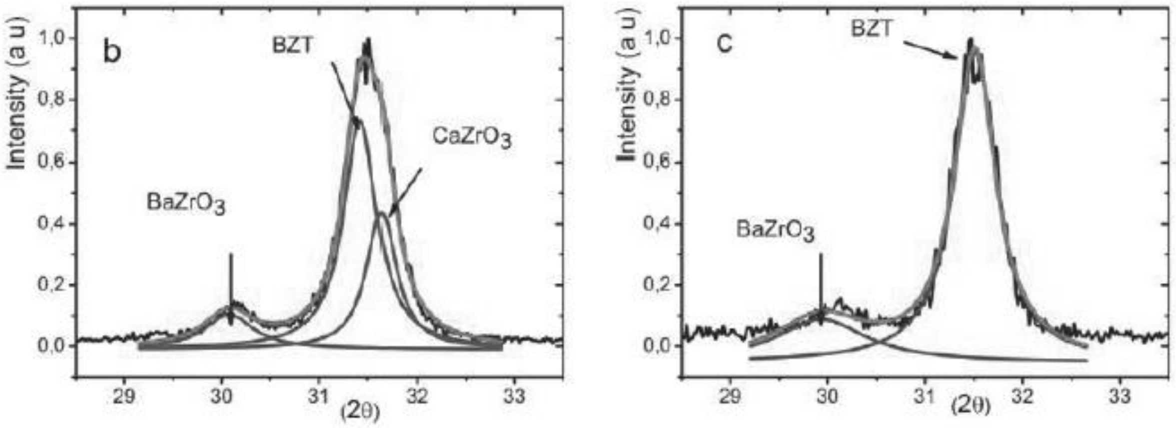

Figure 46: Frattini, Di Loreto et al reported the same result as shown in the HT XRD. [75] Peaks of the powder measured at 1050°C (left) and at 1100°C (right) and the CZ content is decreasing rapidly.

Additionally, at 900°C a secondary phase $Ba_3Ca_2Ti_2O_9$ is formed, which is still existing up to 1100°C. In the STA-MS it is visualized through a broad endothermic peak at 984°C with CO_2 mass loss.

At 1100°C and 2θ=30° $BaZrO_3$ starts to form and the peak is increasing up to 1200°C. Also the perovskite phase of $CaTiO_3$ has been recorded at 2θ=32.5°, 46.7° and 53.2. Just like $BaZrO_3$, the $CaTiO_3$ peaks are also increasing up to 1200°C.

The perovskite phase of $Ba(Zr,Ti)O_3$ is formed at 1100°C which is also visualized in the DSC curve as a flat broad peak at 1077°C.

The remaining amount of the secondary phase $Ba_3Ca_2Ti_2O_9$ and Ba_2ZrO_4 are completely reacted to $Ba(Zr,Ti)O_3$, $CaTiO_3$ and $BaZrO_3$ above 1150°C.

The raw material heated up in 50°C steps to 1200°C did not form a pure perovskite phase. It can be mentioned that the amounts of impurity phases decrease with increasing temperature. At 1200°C BZT, $BaZrO_3$ and $CaTiO_3$ phases can be observed but no BCZT phases.

Nevertheless, the BCZT80 ceramic is sintered at 1400°C and formed a pure perovskite structure with a small impurity amount of $CaTiO_3$.

Higher sintering temperatures may have eliminated such impurity phases due to higher solubility of Ca^{2+} in $BaTiO_3$ lattice.[5]

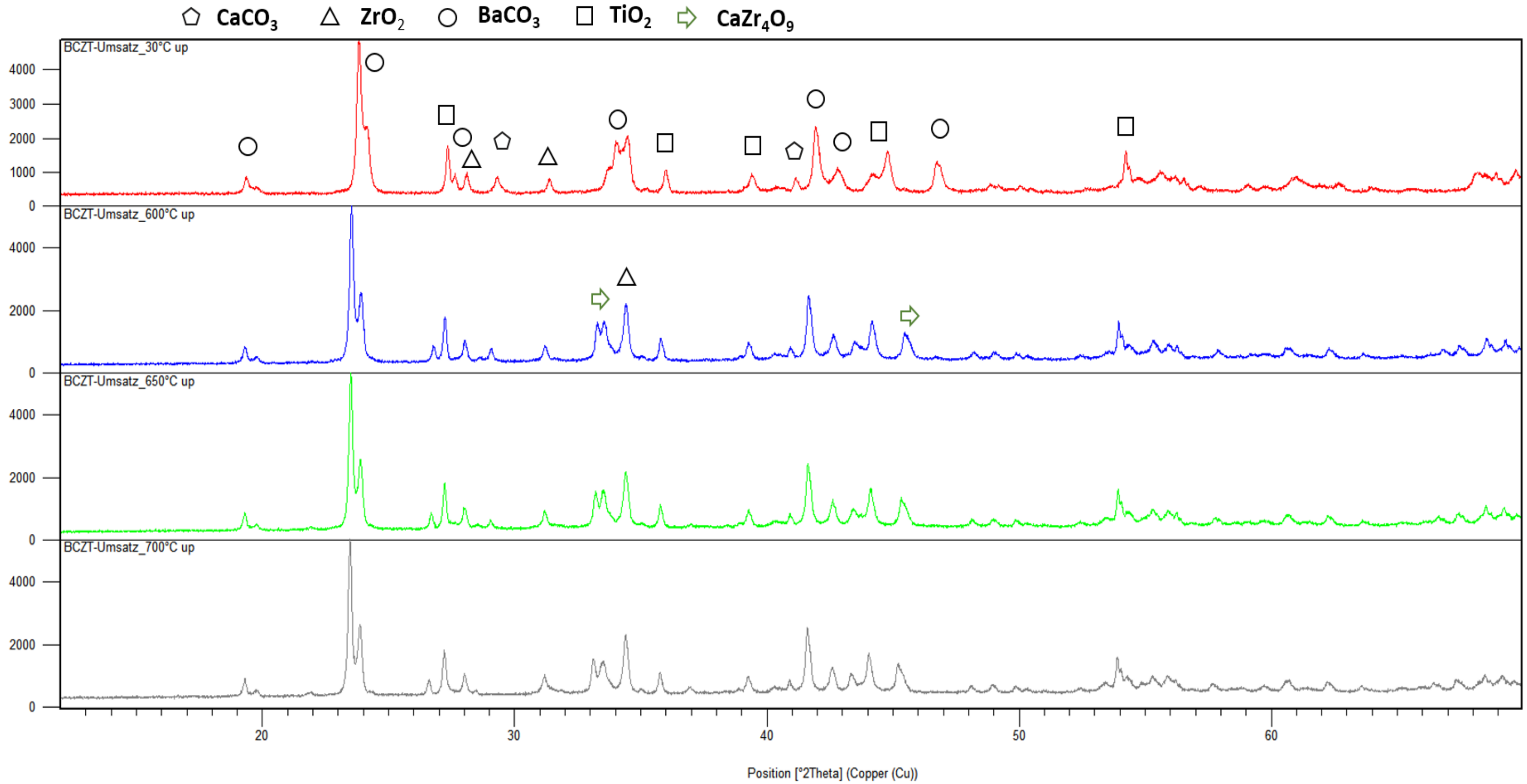

Figure 47: High temperature XRD pattern for BCZT80 in temperature range from 30°C to 700°C. In this temperature range the secondary phase $CaZr_4O_9$ is formed.

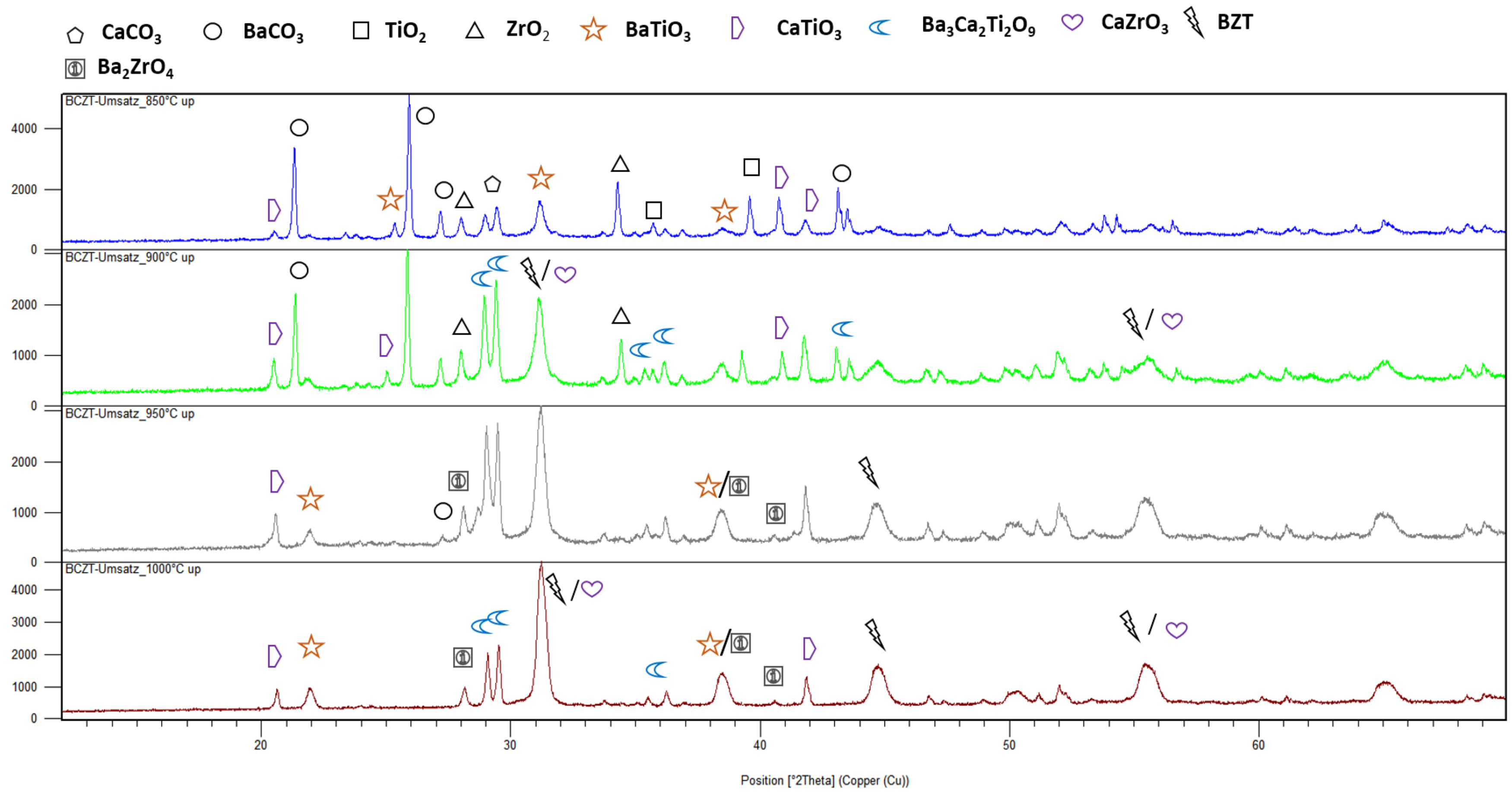

Figure 48: High temperature XRD pattern for BCZT80 from 850°C to 1000°C. There are secondary phases formed which later react to Ba(Zr,Ti)O$_3$ and CaTiO$_3$. In this temperature range there are many overlapping peaks determined.

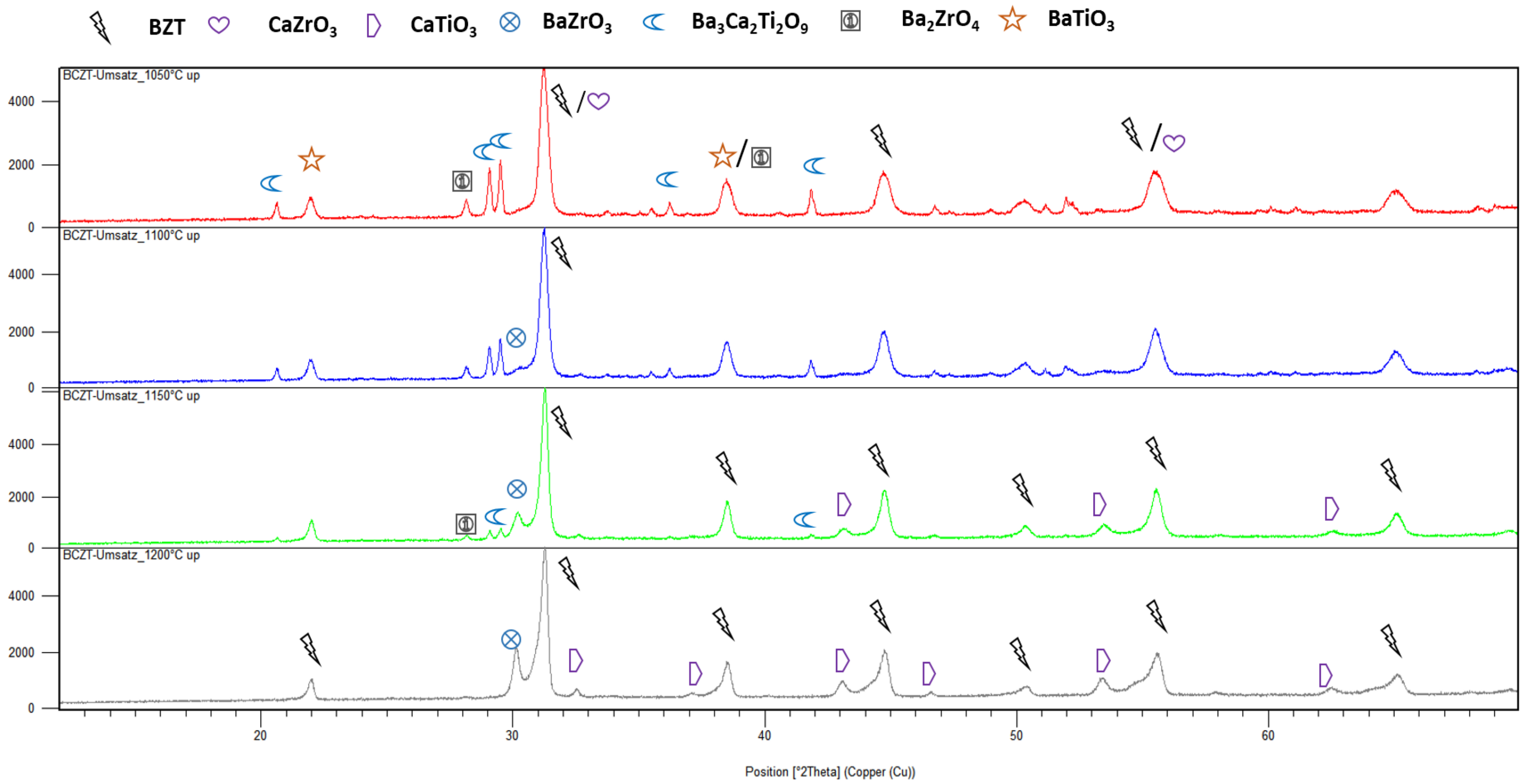

Figure 49: High temperature XRD pattern for BCZT80 from 1050°C to 1200°C. A perovskite phase is formed at 1100°C with $CaTiO_3$ and $BaZrO_4$ as impurity phases.

4.2.3 X-Ray Diffraction

The X-ray diffraction pattern of calcined and sintered BCZT80 is shown in Figure 50. It can be observed that a perovskite structure is formed after calcination at 1250°C, but there are still traces of residual $CaTiO_3$ and $BaZrO_3$. After sintering at 1400°C the intermediate component $BaZrO_3$ disappears and leads to the gradual transformation in the (110) BCZT peak. BCZT has been formed at 1400°C with the perovskite structured $CaTiO_3$. Ca^{2+} and Zr^{4+} diffuse into the $BaTiO_3$ lattice to form a solid solution.

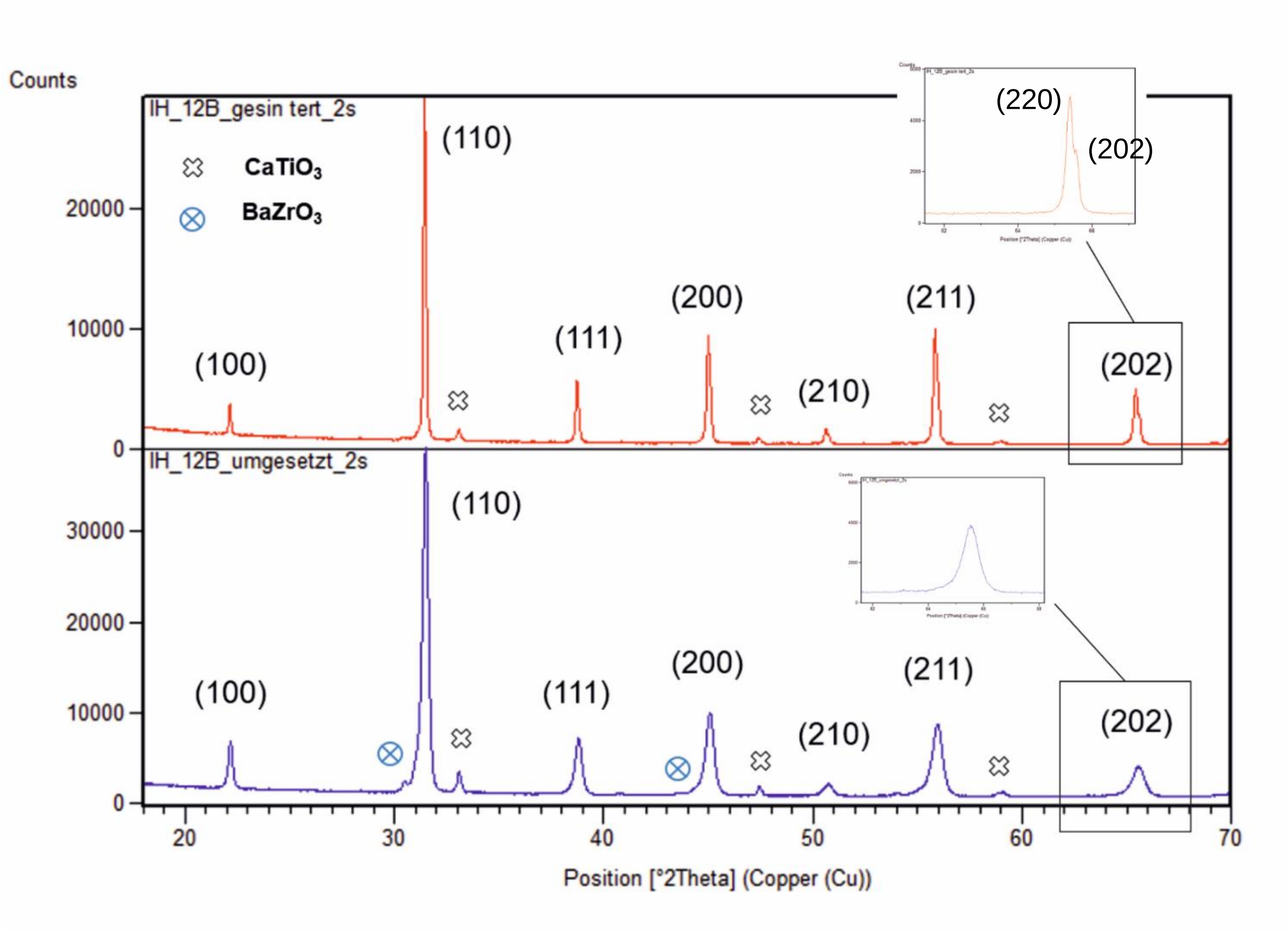

Figure 50: XRD pattern of BCZT80 calcined at 1250°C (blue) and sintered at 1400°C (red)and their impurities. The calcined sample shows a pseudocubic structure whereas the sintered sample indicates a tetragonal phase.

The characteristic peak (200) and (002) around 2θ=45° as well as the peak (220) and (202) around 2θ=65°characterize the phase.

In Figure 50 the (202) peak of the sintered BCZT80 at 2θ=66° shows a splitting peak which is not prominent. Hence the calcined sample shows a pseudocubic structure whereas the sintered sample shows a tetragonal phase.

Figure 51 illustrates that the (200) peak for BCZT94 is more prominent than in BCZT80 which indicates a tetragonal structure. The same effect can be observed in the (202) diffraction peak as seen in Figure 52.

The peak of the BCZT94 ceramic is shifted to a lower angle than BCZT80. This is the result of the different ionic radius of Ba^{2+} and Ca^{2+}. Calcium (1.94 Å) has a much lower ionic radius than barium (2.53 Å).

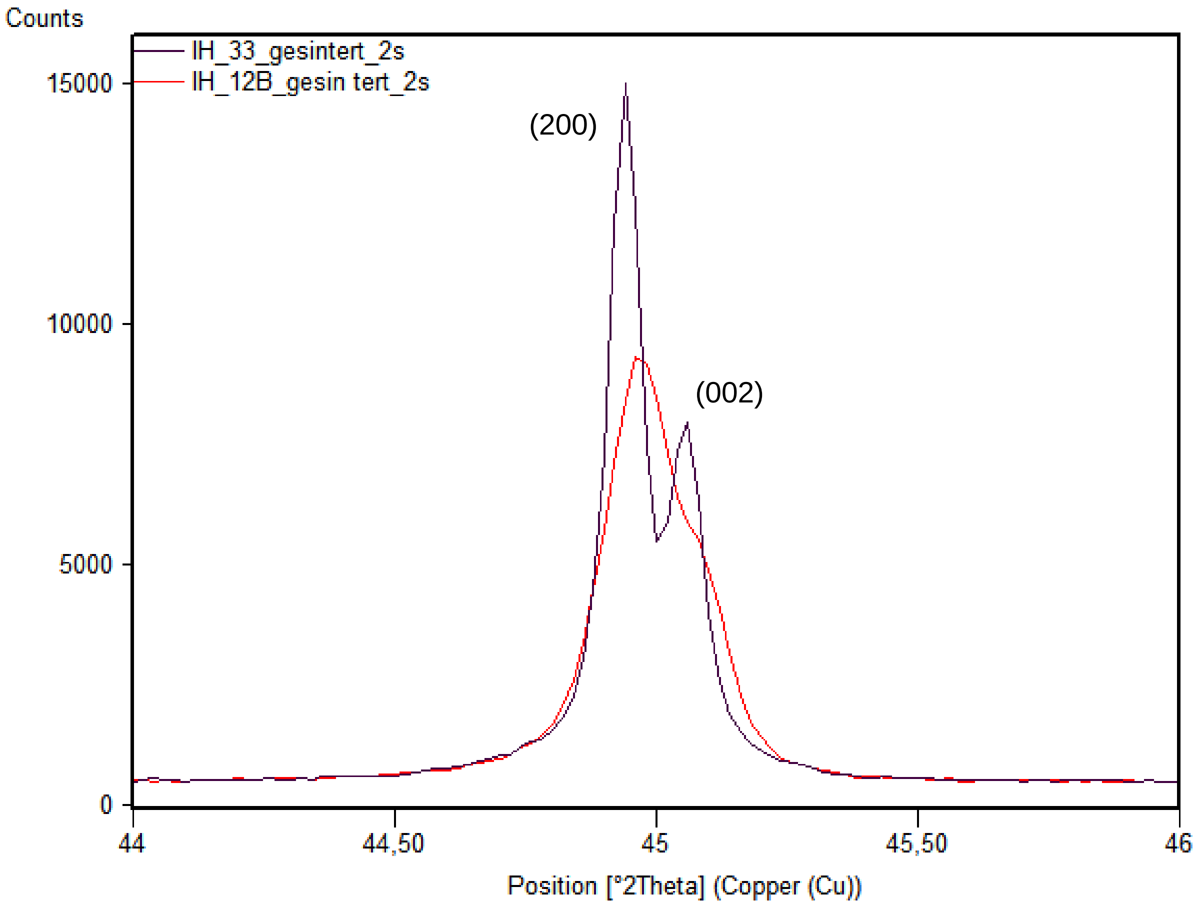

Figure 51: Diffraction peak (200) (002) which is shifted to lower angle with increasing barium content. Displayed with BCZT80 (red) and BCZT94 (purple).

In contrast to the BCZT80 ceramic the BCZT94 ceramic shows a single phase perovskite structure with a small amount of $BaZrO_3$ as impurity phase which can be seen in Figure 52.

The (200) peak splits into two peaks which indicate a coexistence of a tetragonal and a rhombohedral phase.

Considering the “Inorganic Crystal Structure Database” (ICSD) the diffraction peaks for BCZT94 show the tetragonal structure.

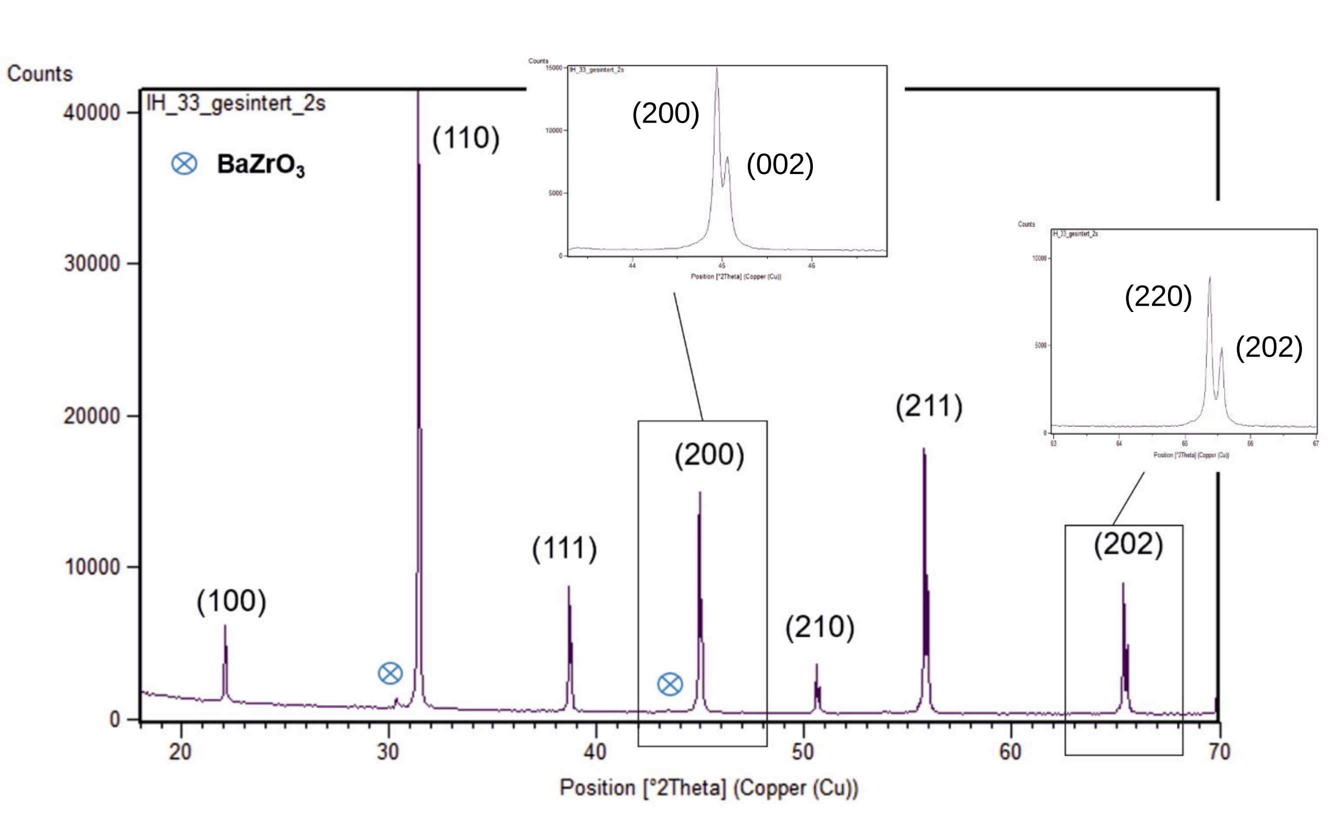

Figure 52: XRD pattern for BCZT94 ceramic sintered at 1400°C with $BaZrO_3$ as impurity phase. A tetragonal structure is formed in that ceramic.

It has to be mentioned that there is only a small amount of unreacted $BaZrO_3$ and no $CaTiO_3$ because the lower concentration of Ca^{2+} in contrast to BCZT80. To form a homogeneous solid solution Ca^{2+} and Zr^{4+} diffuse into the $BaTiO_3$ lattice.

As already stated above, the cell volume is decreasing with increasing barium content which can be obtained from the table below.

Table 7: Lattice parameters, cell volume and crystal structure for BCZT80 and BCZT94 ceramics.

Composition	**Crystal Structure**	**a (Å)**	**c (Å)**	**Cell volume (Å^3)**
BCZT80	tetragonal	4.0401	4.0422	65.98
BCZT94	tetragonal	4.0201	4.0616	65.64

The following figures represent the high temperature XRD, to exhibit how the forming reaction of BCZT80 is taking place.

4.2.4 Densification and Shrinkage

The geometrical density of the green body and the sintered sample are measured through a vernier caliper. The volume shrinkage of the samples is higher than 31% and the length and diameter shrinkage is between 7% and 16%.

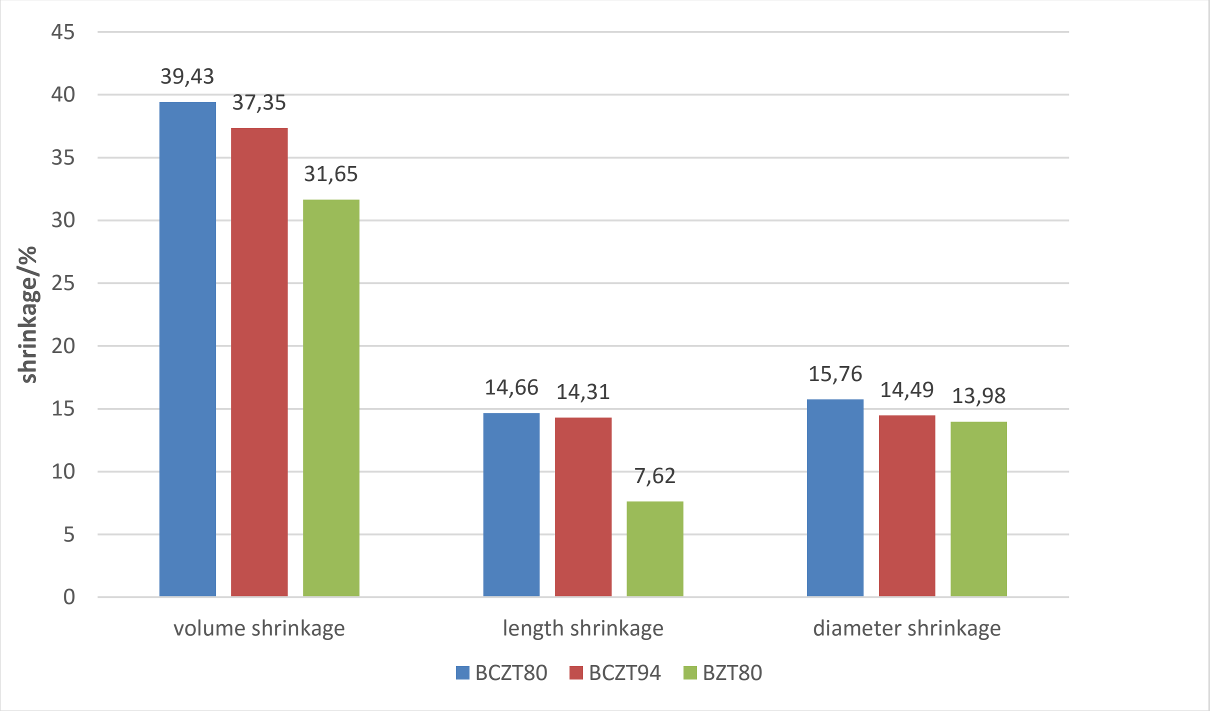

Figure 53: Shrinkage values from the geometric density of the green body in relation to the sintered samples, compared for BZT80, BCZT94 and BCZT80 ceramics.

The BCZT (BCZT80 and BCZT94) powder has a higher shrinkage than that of BZT80. The relative densities of the BCZT ceramics show the same effect. Therefore, it can be concluded that Ca^{2+} substitution increases the sinterability of the powder and the following table shows the difference of relative densities.

Table 8: Relative densities of BZT and BCZT ceramics.

Composition	Calculated density/ g·cm^{-3}	Theoretical density/ g·cm^{-3}	Relative density/%
BCZT80	5.30	5.61	94.48
BCZT94	5.39	5.93	91.45
BZT80	5.15	6.06	84.99
BZT75	5.22	6.10	85.59

It can be noted that, with decreasing Ca^{2+} content the theoretical density is increasing.

4.2.5 Dielectric Properties

Figure 54 shows the relative permittivities at different temperature as a function of the frequency (1kHz) for BCZT and BZT ceramics. It can be seen that BCZT80 and BCZT94 show a wider peak in contrast to the BZT ceramics.

The temperature maximum (T_m) shifts to lower temperatures with decreasing Ti^{4+} content. Another trend is that T_m is shifted to lower temperatures with increasing Ca^{2+} content and the peak is getting broader.

The ceramic without titanium (BCZ) shows no peak maximum because T_m is at much lower temperatures then measured.

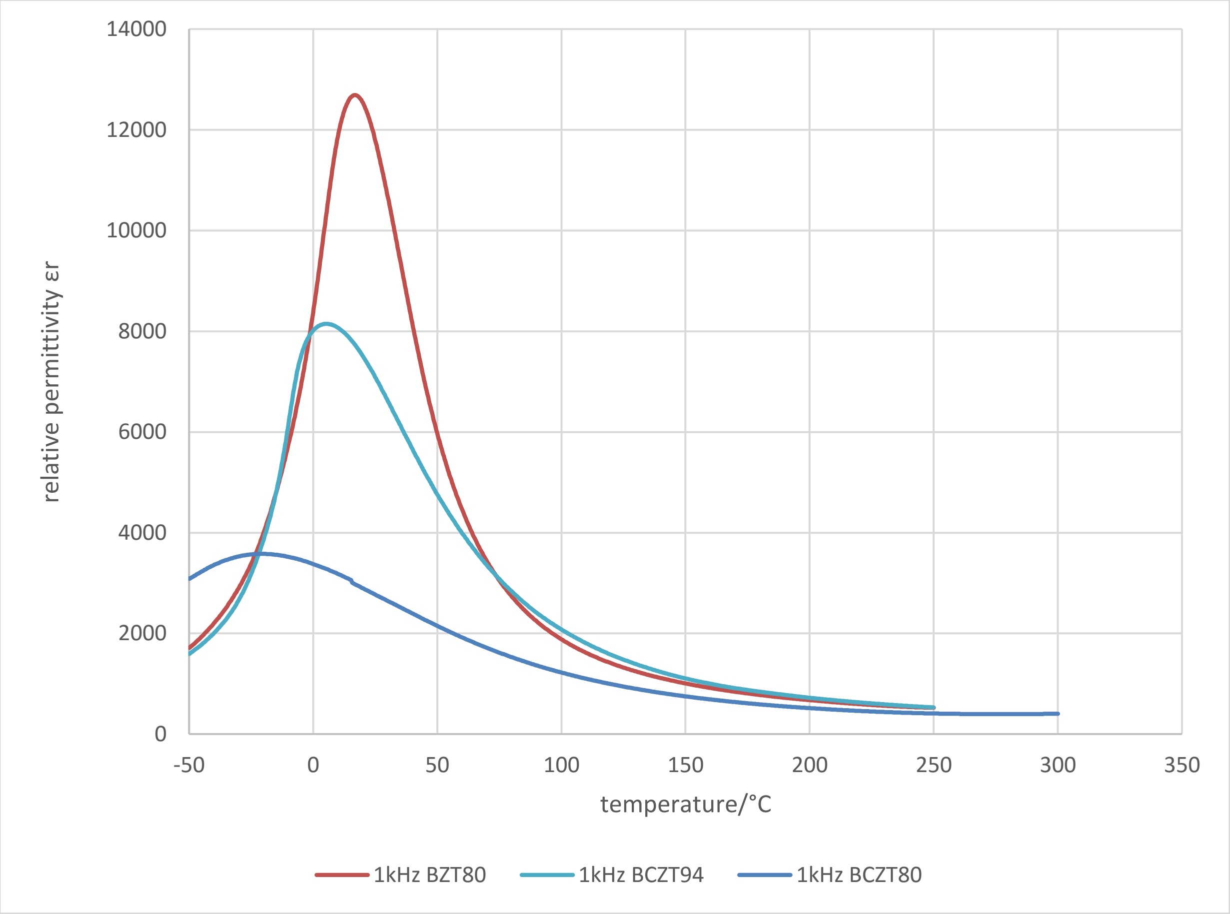

Figure 54: Temperature dependent relative permittivity of BZT and BCZT ceramics at 1kHz.

Figure 55 shows the frequency dependence at room temperature of the BCZT ceramic. It is observed that the relative permittivity is decreasing with increasing frequency which typical for ferroelectric relaxor material. Higher Ca^{2+} content results in lower relative permittivity. To emphasize the relaxor properties the relative permittivity is plotted against the temperature in Figure 56 and Figure 57.

.

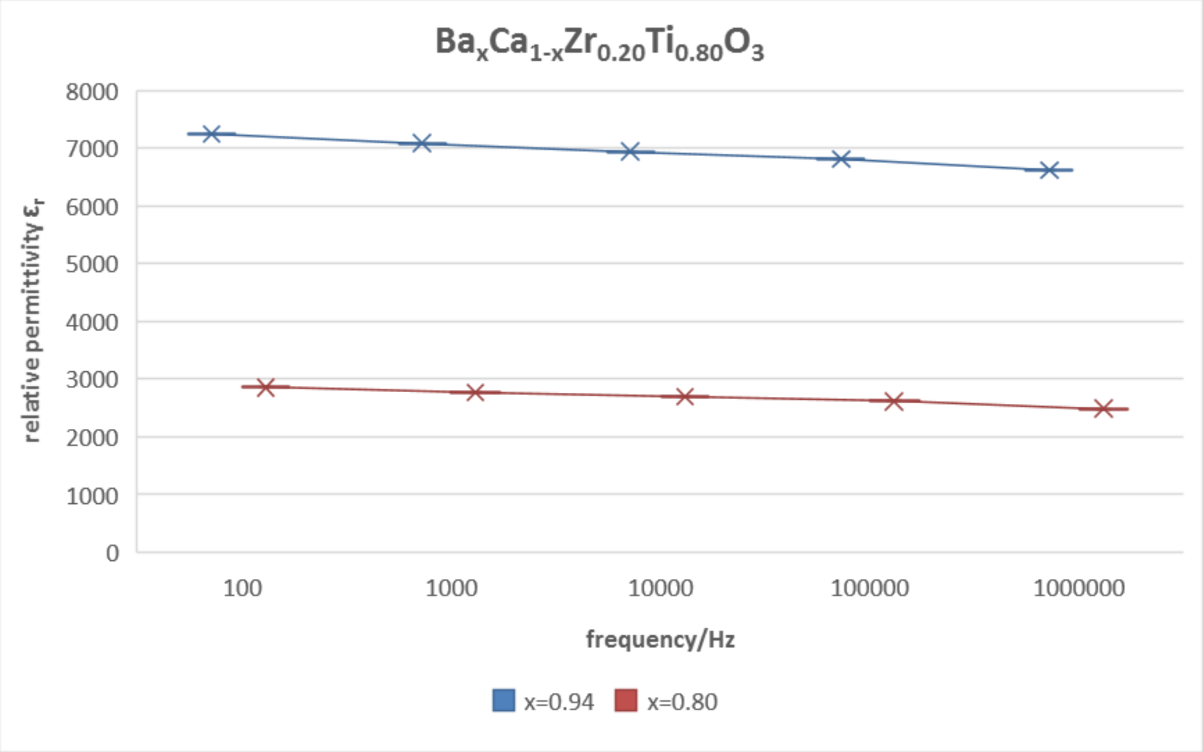

Figure 55: Dielectric permittivity as function of frequency for BCZT with x=0.94 and x=0.80.

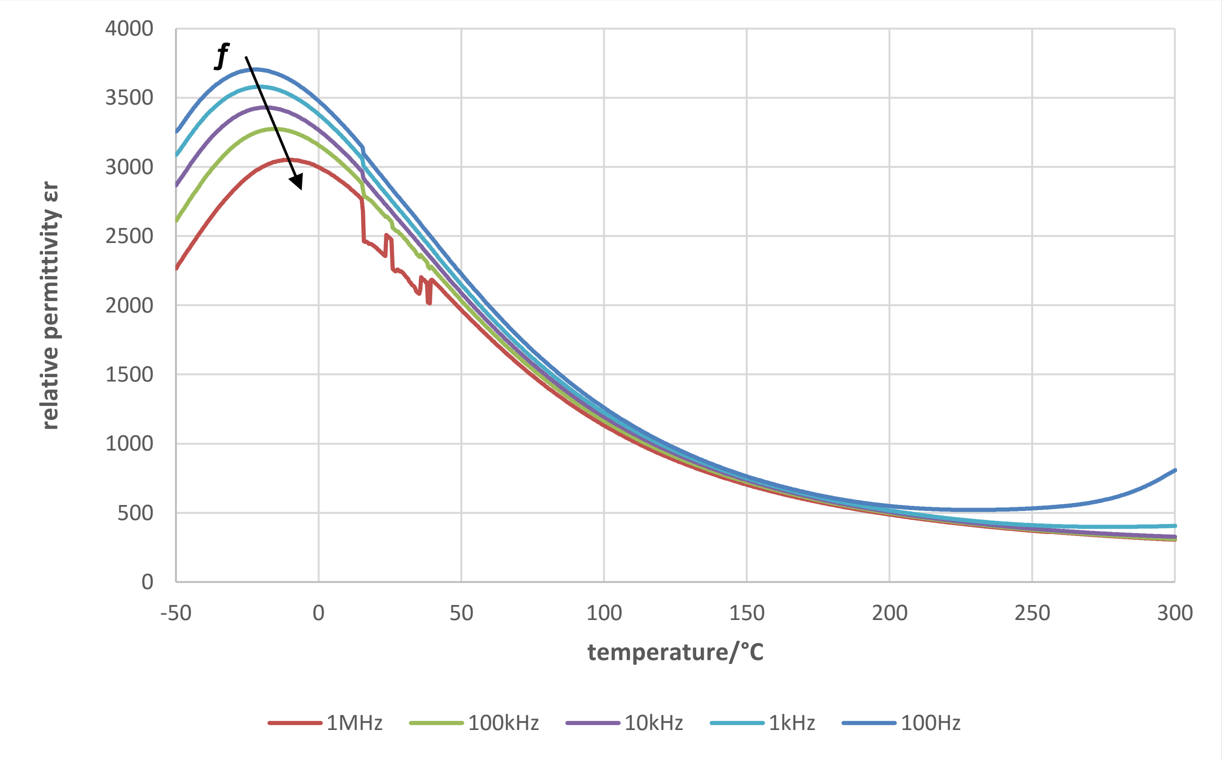

Figure 56: Variation of the relative permittivity for different temperatures for BCZT80 ceramic sintered at 1400°C for 4 hours.

BCZT80 and BCZT94 ceramics show both a ferroelectric relaxor behaviour. The characteristics are varying by the composition of the ceramic. In this kind of ceramic two types of cationic substitution take place:

1. Ca^{2+} - Ba^{2+} substitution
2. Zr^{4+} - Ti^{4+} substitution

The noise between 0°C and 50°C is most probably because of intermittent contact problems of the BCZT80 ceramic.

The main dielectric relaxor characteristic increases as the Ca^{2+}-Ba^{2+} substitution and the Zr^{4+}-Ti^{4+} substitution rate increases. It is due to the effect of heterogeneity which is also a typical case in the lead perovskite relaxor material PMN.[76]

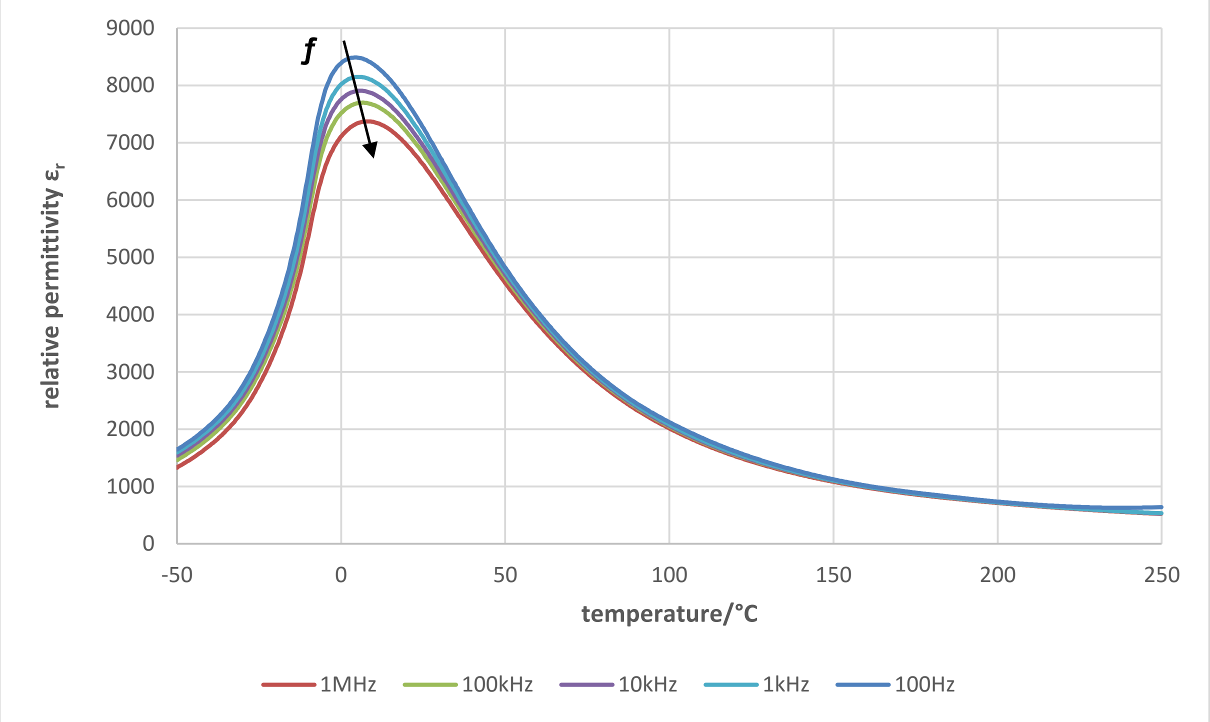

Figure 57: Variation of the relative permittivity for different temperatures for BCZT94 ceramic sintered at 1400°C for 4 hours.

BZT80 (18°C) has a higher phase transition temperature than BCZT80 (-17°C). It can be infered that Ca^{2+} substitution has deteriorated the Curie temperature in BZT ceramics. Increasing the Ca^{2+} content from 6% to 20% the transition temperature is shifted from -3°C to -17°C. This confirms that the Ca^{2+} occupies an A-site in the BZT ceramics. The calcium doping of the BZT ceramics also lead to a reduction of permittivity, which can be seen in Table 9. It can be observed that the loss factor of BCZT80 is nearly the same as in BZT80 and doping with 6% calcium leads to a lower loss factor. In the temperature range from -28°C to 195°C the loss factor is smaller than 3% which signifies a good temperature stability.[5]

In contrast to the BZT ceramics, the BCZT ceramics show a broader peak around the transition temperature because of a diffuse phase transition that is taking place in the BCZT ceramics.[40]

Table 9: Relative permittivity, loss factor and diffuseness γ for BCZT and BZT ceramics at 1kHz.

Composition	ε at RT	tanδ at RT	T_m/°C	γ
BZT80	11880	0.021	18	1.71
BCZT80	2770	0.020	-17	1.93
BCZT94	7089	0.015	-3	1.88

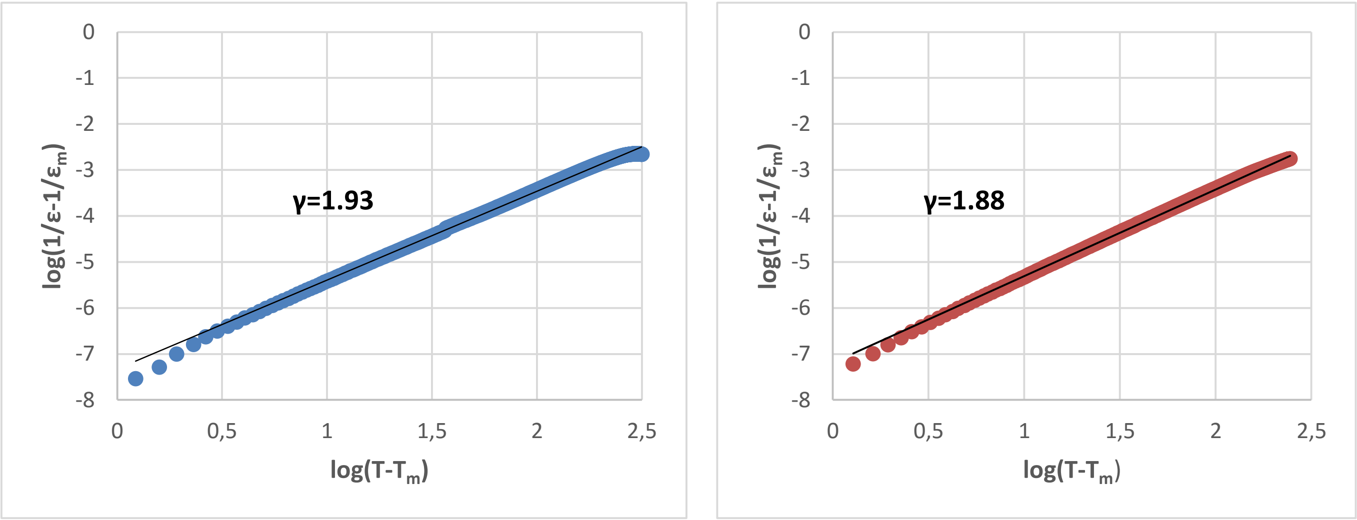

Figure 58: Plot of the diffuseness of BCZT80 (blue) and BCZT94 (red) to show the relaxor behaviour.

In Figure 58 a linear relationship is observed for all BCZT ceramics. The slope of the curve is used to determine the diffuseness constant γ. The diffuseness is increasing with increasing Ca^{2+} content. This effect is similar to changing the Zr^{4+} content of the BZT ceramics as described in chapter 4.1.5.

It can be noted that the calcium substitution of 20% at the A-site of the perovskite structure enhanced the diffuseness factor in the BZT ceramics. Furthermore, the diffuseness constant of BCZT80 is near 2 which is due to the cationic disorder and fluctuation of the simultaneous substitution of A- and B- site.

4.3 Characterization of $Ba_{0.80}Ca_{0.20}ZrO_3$

This chapter provides the $Ba_xCa_{1-x}ZrO_3$ synthesis were x=0.80 (BCZ80). The preparation is done via mixed oxide route with the same conditions as they are used in the chapters 4.1and 4.2.

$BaZrO_3$ is an ABO_3 perovskite dielectric material which is mechanically and chemically stable. Material properties are often optimized through doping and so it is important to understand the structure and the material of a doped ceramic. In that chapter the property of a Ca^{2+} doped $BaZrO_3$ is discussed. The focus is on the forming reaction mechanism, the dielectric properties and the density measurement. Furthermore, the results were compared with the BCZT80 ceramic.

4.3.1 Thermal Analysis

The starting and end temperature of the thermogravimetry is shifted to higher temperatures as seen in the figure below. Additionally, the CO_2 mass curve is shifted to lower temperatures by decreasing the heating rate from 10K/min to 3K/min.

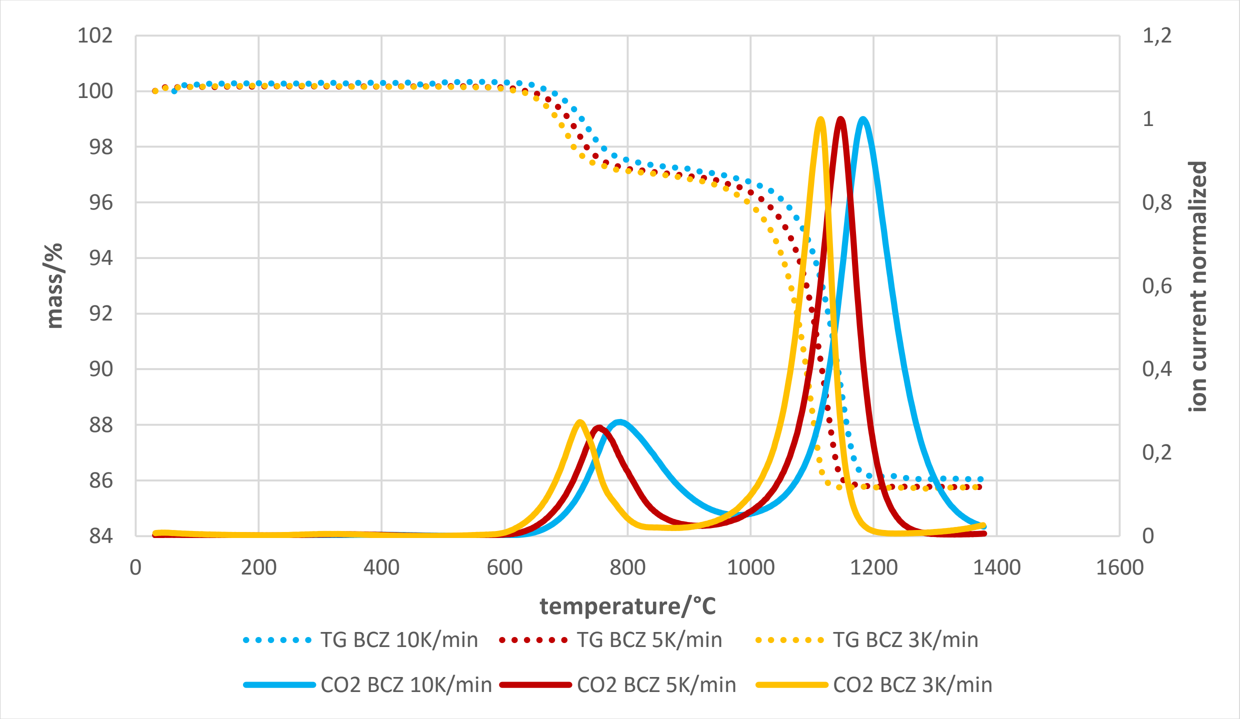

Figure 59: TG-MS with different heating rates of BCZ80. The extrapolated end temperature is calculated with 1063°C.

The TG/DSC-MS is shown in the figure below. The thermogravimetry curve (black) of BCZ80 shows a decomposition of the carbonates in two steps starting at 686.8°C and ending at 1169.3°C. The mass loss of 3.05% and 11.12% is due to the CO_2 loss. The CO_2 loss is also visualized through the mass spectrometry.

The mass spectrum of water can be neglected because the mass loss is taking place below 200°C.

Furthermore, the DSC curve (blue) shows 5 endothermic peaks, while the first at 744.2°C can indicate the formation of $CaCO_3$ which results in a further reaction. The peak at 830.2°C corresponds to the formation of $BaCO_3$ from the orthorhombic crystal structure to the trigonal one and at 983.7°C there is another formation of $BaCO_3$ due to the CO_2 mass loss The broad peak at 1150.7°C describes the formation of the perovskite structure.

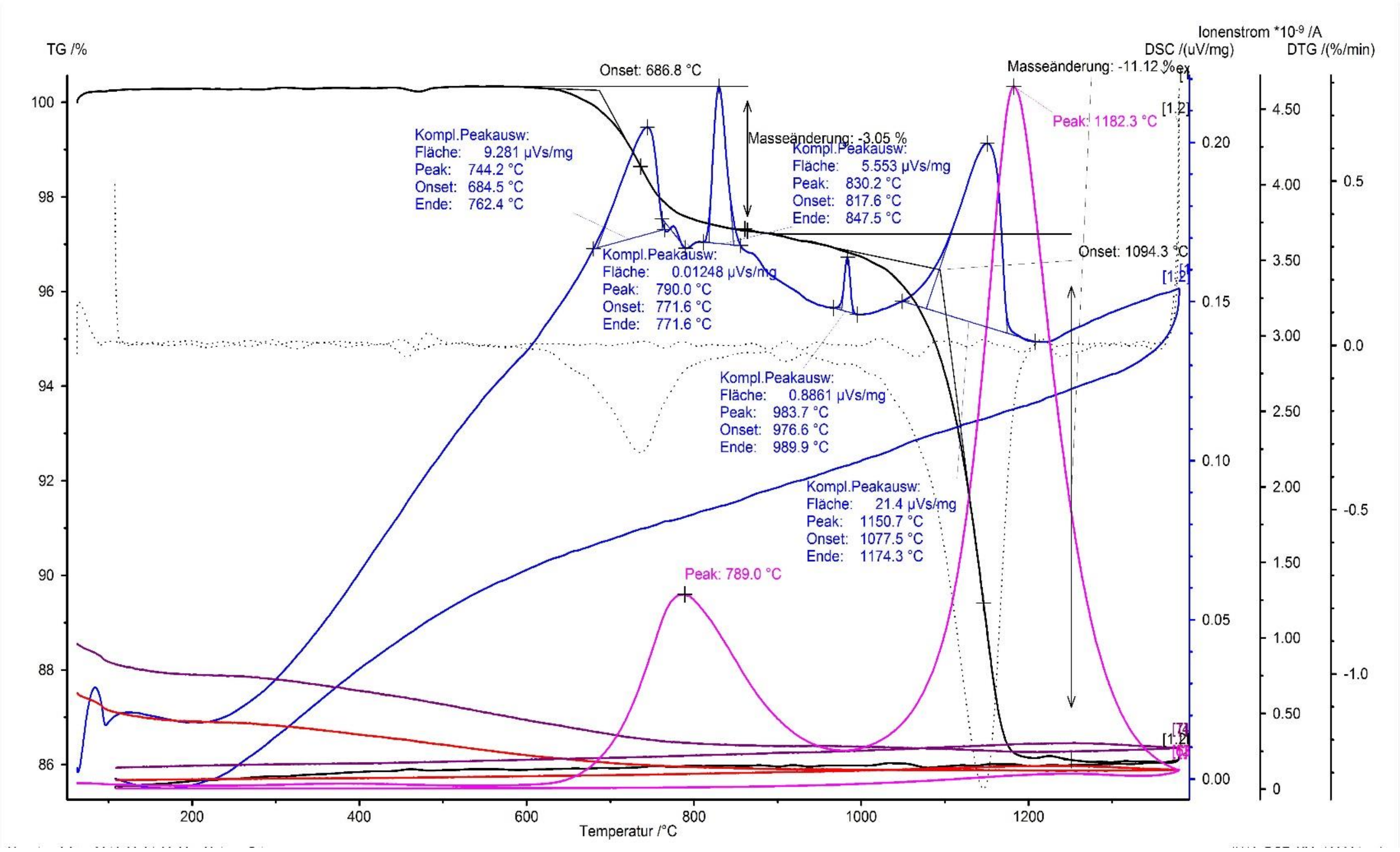

Figure 60: TG/DSC-MS of BCZ80 ceramic with a heating rate of 10K/min.

In Figure 61 and Table 10 the difference for BCZT80 and BCZ ceramics is shown. The first decomposition step around 690°C remains nearly unchanged whereas the second decomposition step is shifted by approximately 200°C. The end temperature for BCZ80 is at 1169.3°C and for BCZT80 at 1011.1°C.

This temperature shifting is due to some unreacted $BaCO_3$ which is completely reacted at higher temperatures. Also the second mass loss starts at higher temperatures.

Table 10: Temperature and mass loss differences of BCZ80 and BCZT80 ceramics with a heating rate of 10 K/min.

Composition	$T_{1,start}$/°C	$T_{2,start}$/°C	$T_{,end}$/°C	1st mass loss	2nd mass loss
BCZ80	686.8	1094.3	1169.3	3.05%	11.12%
BCZT80	699.7	912.6	1011.1	3.49%	12.75%

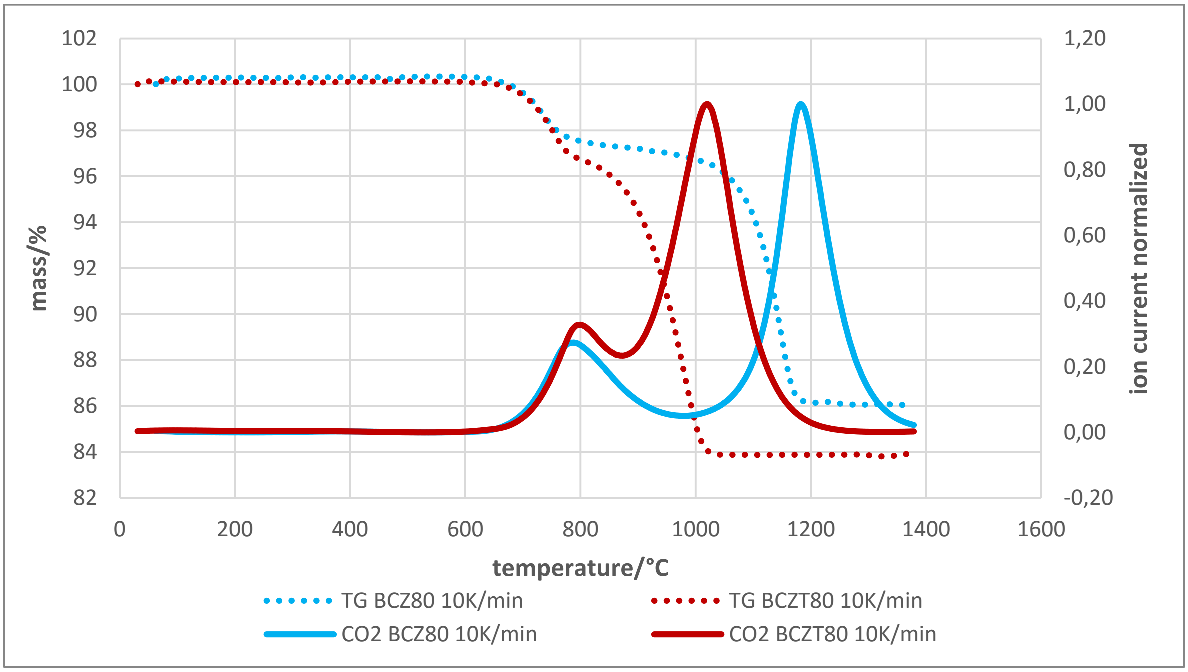

Figure 61: TG -MS curve of BCZT80 BCZ80 to show the difference of the Ti^{4+} content.

To understand the reaction better a high temperature XRD is done from room temperature to 1200°C to reveal the formation reaction which is taking place.

To control the reaction conditions a XRD at room temperature is done form the sintered (1400°C) and calcined (1250°C) sample. The XRD pattern includes the information of lattice parameter and the cell volume.

4.3.2 High Temperature X-Ray Diffraction

As also mentioned in the TG/DSC-MS the reaction starts at around 600°C which is also seen in the HT XRD (Figure 62 to Figure 65) . From room temperature to 600°C the $CaCO_3$ start to react with ZrO_2 to the secondary phase $CaZr_4O_9$ which can also be obtained from the DSC curve. That step shows a CO_2 mass loss which is visualized from the thermogravimetry.

Furthermore, at 750°C a peak formation at 2θ=33° is taking place, which indicates the formation from $CaZr_4O_9$ to $CaZrO_3$. The endothermic peak in the DSC curve at 744.2°C

visualizes the formation of the secondary phase $CaZr_4O_9$. Furthermore, that phase is reacting to $CaZrO_3$ which is shown as small peak at 790.0°C in the DSC.
The $CaZr_4O_9$ has been fully converted and a small amount of $BaZrO_3$ has been formed which is reacting slowly to 950°C.

At 850°C a formation from orthorhombic phase (space group: Pm3m) to a trigonal (space group: R3mH) phase (2θ=21.5 and 26°) of $BaCO_3$ has occurred. This reaction is also illustrated in the DSC at approximately 830°C.

At 1000°C the trigonal $BaCO_3$ peak shifts from 2θ=21° to 23° which represents the cubic (space group: Fm3m) phase of $BaCO_3$. It can be obtained from the DSC curve at 983°C. Furthermore, the $BaZrO_3$ peak increases rapidly because the amount of $BaCO_3$ decreases. $BaCO_3$ starts to react with $CaZrO_3$ under CO_2 loss which is figured in the thermogravimetry. At 1000°C the initial compounds ZrO_2 and $BaCO_3$ are still existing. Between 1000°C and 1100°C they start reacting rapidly to form $BaZrO_3$.

Finally, at 1100°C the perovskite structure has been formed which is observed as broad peak in the DSC at 1094.3C.
In comparison to the X-ray diffraction pattern it can be mentioned that a barium rich and a calcium rich zirconate is formed. Also at 1400°C the XRD shows the same result as at 1200°C. The structure does not contain any impurity phases and it can be concluded that the smaller Ca^{2+} reacts first with the ZrO_2 and then Ba^{2+}.

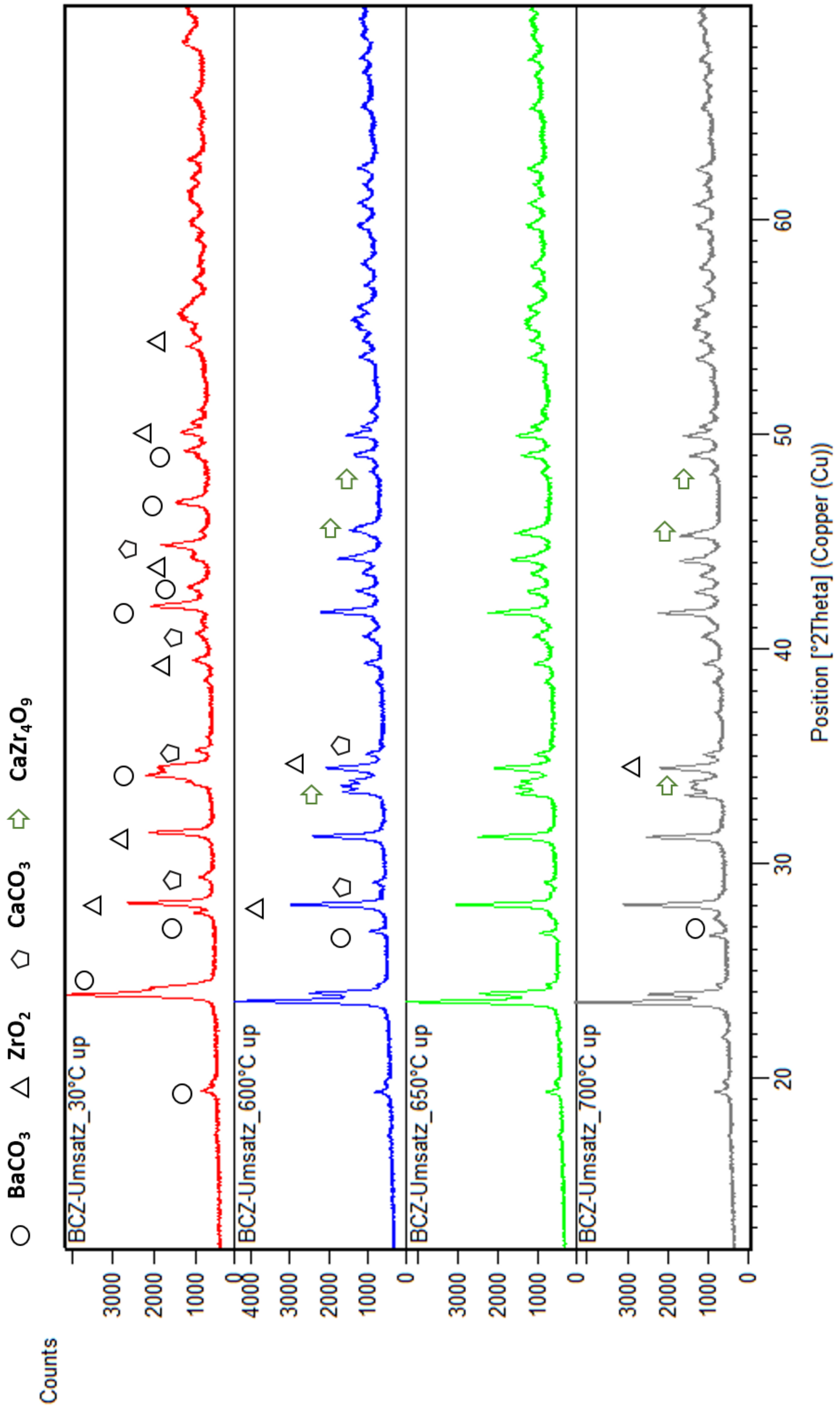

Figure 62: HT XRD for BCZ80 up to 700°C, which indicates the formation from the initial components to $CaZr_4O_9$

.

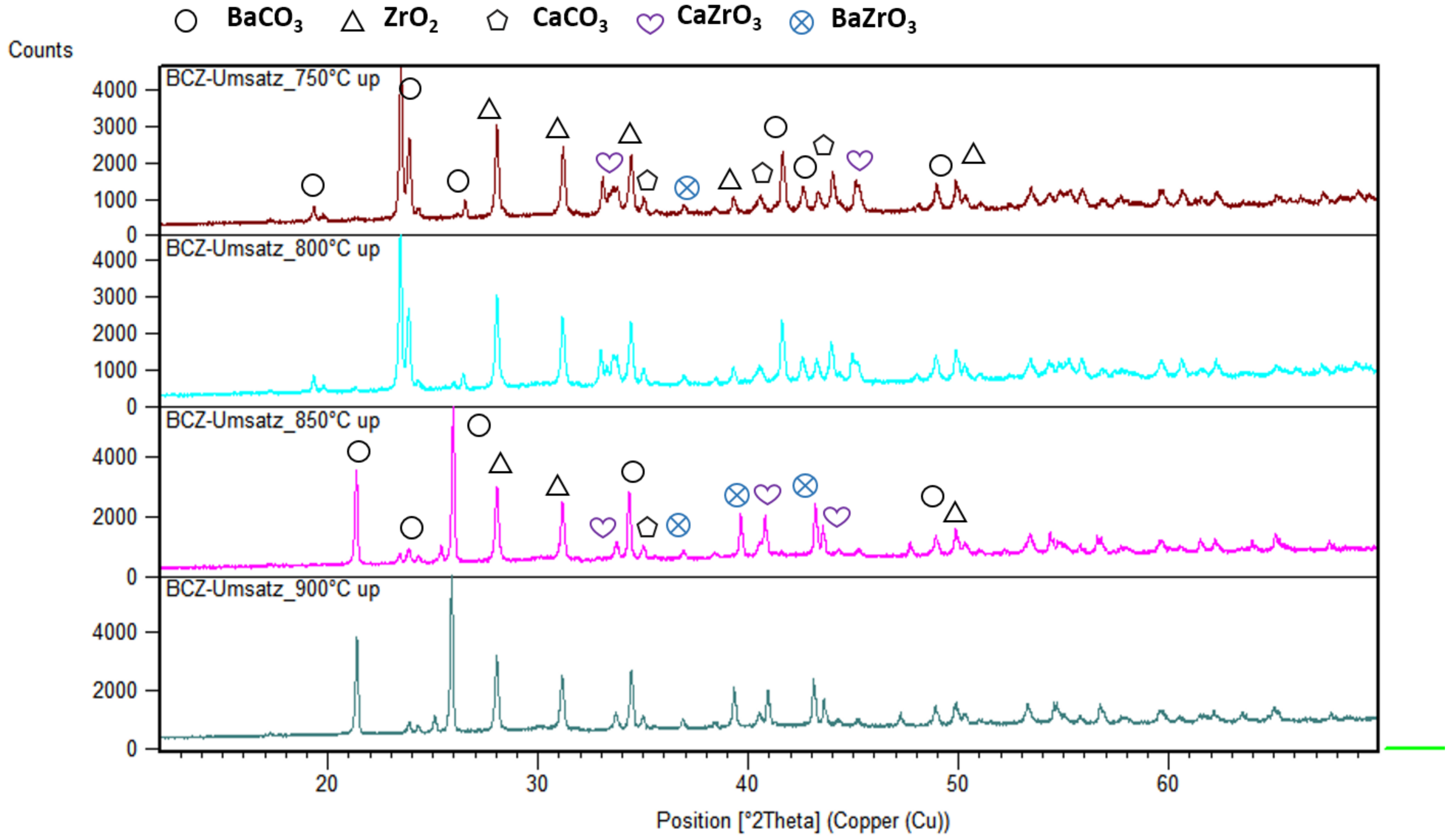

Figure 63: HT XRD for BCZ80 up to 900°C which displays the formation from $CaZr_4O_9$ to $CaZrO_3$ and reduces the $BaCO_3$. ZrO_2 content remains the same.

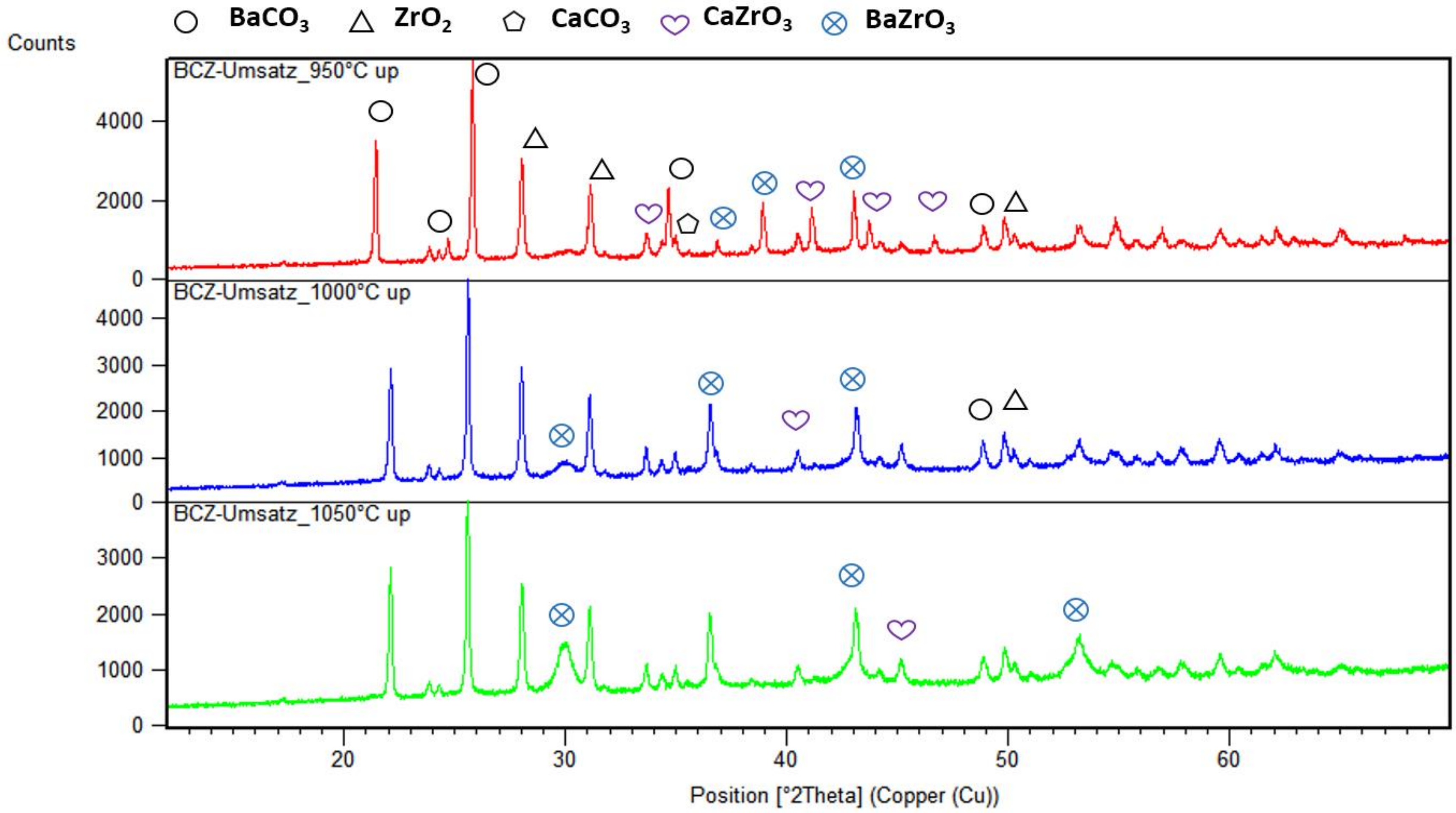

Figure 64: HT XRD for BCZ80 up to 1050°C, which shows that the secondary phase has completely reacted to $CaZrO_3$ and all initial component have reacted to the zirconates.

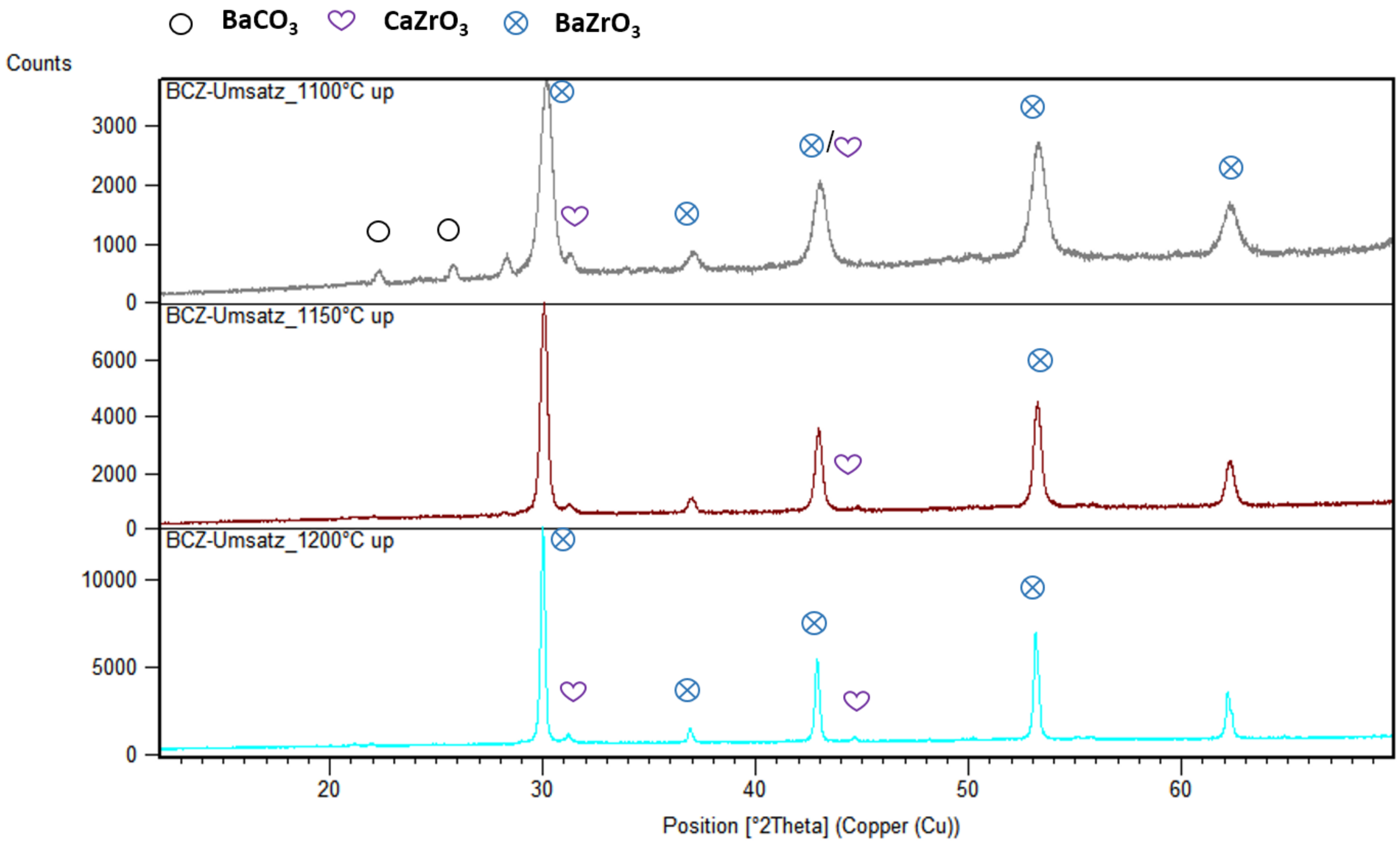

Figure 65: HT XRD for BCZ80 up to 1200°C which displaces the reaction of the perovskite structure to $BaZrO_3$ and $CaZrO_3$.

4.3.3 X-Ray Diffraction

The X-ray diffraction pattern of calcined (1250°C) and sintered (1400°C) powder is shown in Figure 66. A barium rich perovskite structure and an orthorhombic calcium rich structure is displayed.

It can be seen that the calcined and sintered X-ray diffraction pattern are similar.

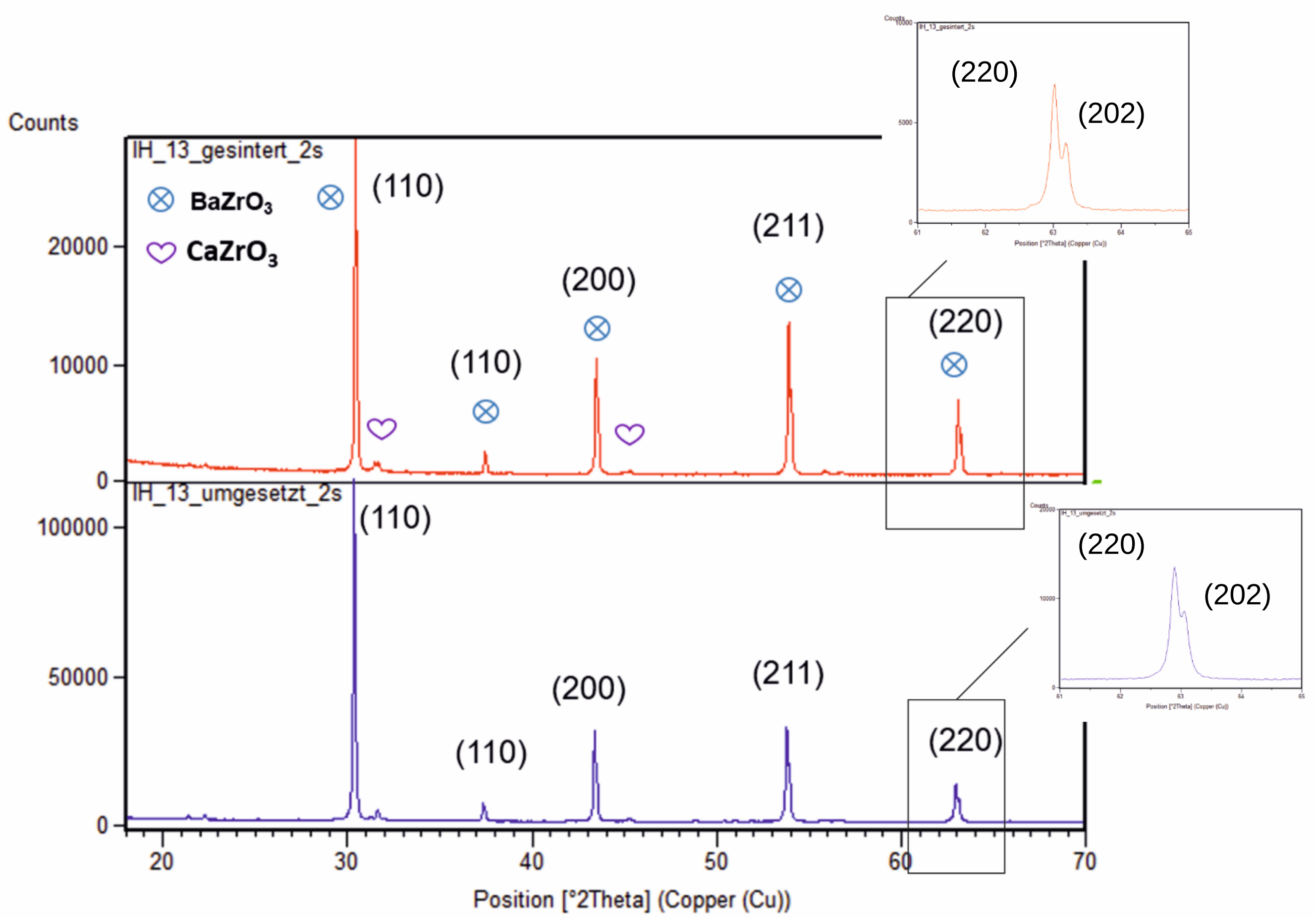

Figure 66: XRD pattern for BCZ80 ceramic and phase identification. The calcined (blue) and the sintered (red) sample show both a tetragonal phase with a calcium and a barium rich perovskite structure.

As illustrated in the XRD pattern, the barium rich perovskite, denoted as $BaZrO_3$ has a tetragonal structure and includes calcium rich perovskite, denoted as $CaZrO_3$ as impurity phase. The tetragonal structure can be identified through the diffraction peaks (202) and (220) at $2\theta=63°$ and (200) (002) at $2\theta=44°$. To determine the cell volume and therefore the theoretical/relative density, the lattice parameters were defined through rietveld refinement.

Table 11: Lattice parameters, density and cell volume for the BCZ80 ceramic.

	BCZ80
Crystal structure	Tetragonal (I4/mcm)
a/ Å	4.1653
b/ Å	4.1774
Cell volume/ Å^3	72.48
Theoretical density/ g·cm^{-3}	5.89

Additionally, the structural changes are induced by doping $BaZrO_3$ with Ca^{2+}. The Ba^{2+} in the $BaZrO_3$ has a high symmetry position in the oxygen cage, whereas Ca^{2+} atoms displace a low-symmetry position. [77]

The structural changes with increasing Ca^{2+} content can be seen in the phase diagram below, which is displayed by Levin, Amos et al. [53]

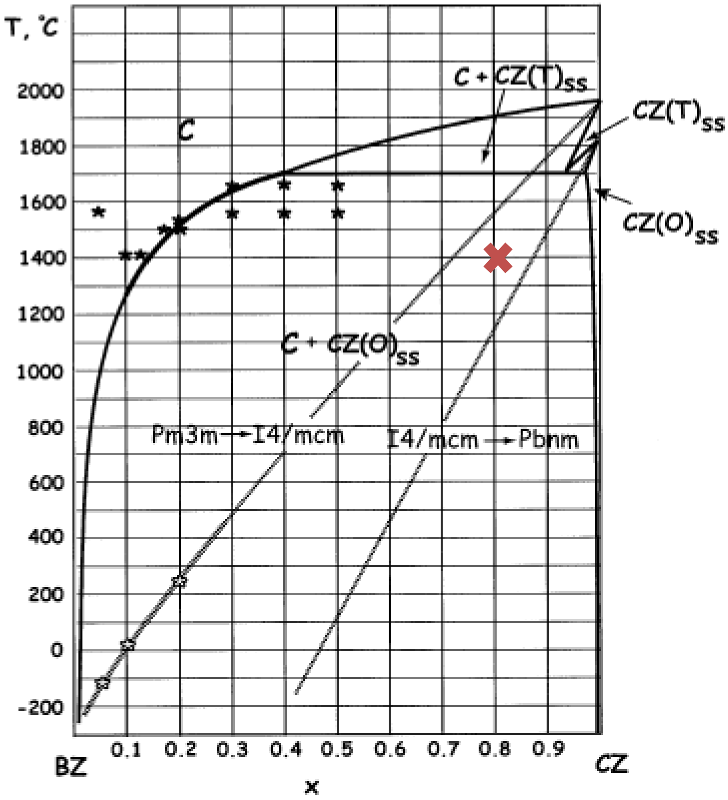

Figure 67: Phase diagram for the $Ba_{0.80}Ca_{0.20}ZrO_2$.[53]

4.3.4 Densification and Shrinkage

The BCZ80 ceramic shows similar results as the BCZT80 ceramic. The volume shrinkage is in both samples around 40%, the diameter shrinkage around 14% and the length shrinkage around 16%.

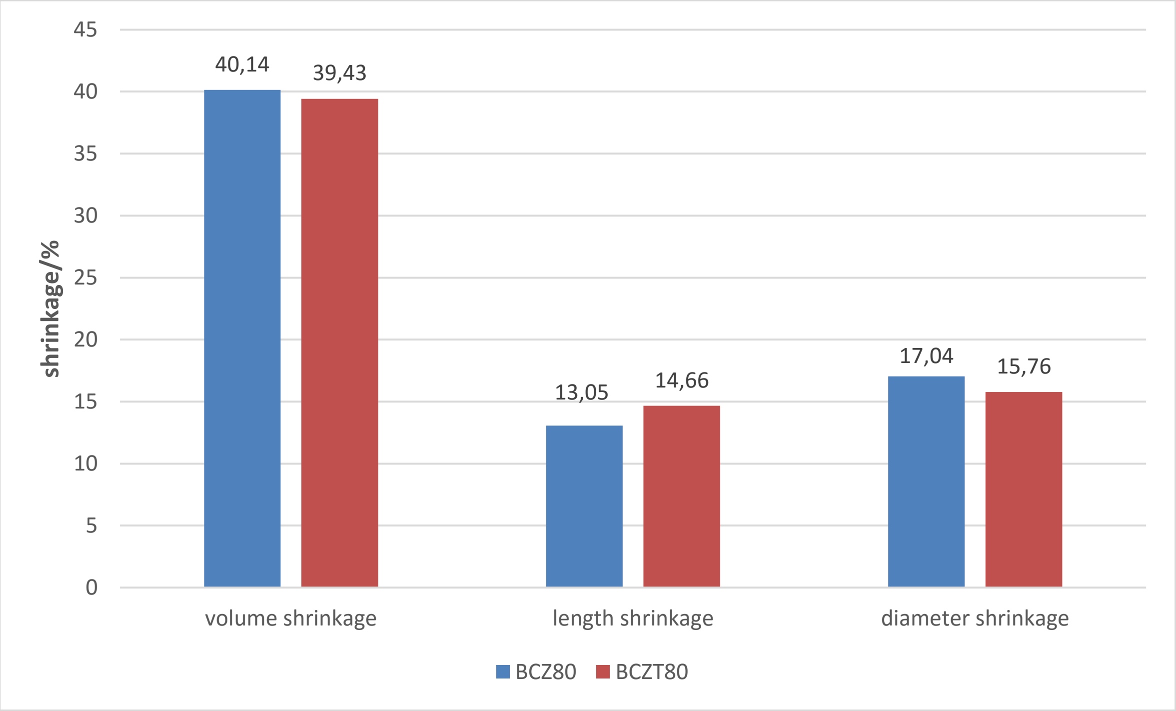

Figure 68: Difference of the shrinkage measurement of BCZ80 and BCZT80 ceramic.

As in the chapters before, also the relative density for the BCZ80 ceramic is determined, to check the sinterability of the sample. In the following table the ceramics without Ti^{4+} concentration (BCZ80) and with 80% Ti^{4+} concentration of (BCZT80) are displayed.

Table 12: Relative densities in contrast of the BCZ80 and the BCZT80 ceramic.

Composition	**Calculated density/ g·cm^{-3}**	**Theoretical density/ g·cm^{-3}**	**Relative density/ %**
BCZ80	5.23	5.85	91.86
BCZT80	5.30	5.61	94.48

With decreasing zirconium content, the relative density is getting higher whereas the theoretical density decreases.

To sum up it could be mentioned that the geometric (=calculated) and theoretical density are nearly the same and both show a value below 6.00 g·cm^{-3}, whereas the ceramics which do not include calcium have a density above 6.00 g·cm^{-3}.

4.3.5 Dielectric Properties

In the discussion of the dielectric properties of BCZ80 it might be interesting to compare the permittivities of $BaZrO_3$ and $CaZrO_3$ which are listed in Table 13.

Table 13: Relative permittivities for the ceramics of $BaZrO_3$ and $CaZrO_3$ according to reference Levin and Amos et al. [53] The relative permittivity of BCZ80 has been measured via impedance spectroscopy

	$BaZrO_3$	$Ba_{0.80}Ca_{0.20}ZrO_3$	$CaZrO_3$
Relative permittivty ε	36[53]	53[1]	30[53]

The dielectric constant of BCZ80 can be increased up to 47% by doping with a small amount of calcium. As seen in Table 13 the relative permittivity of $CaZrO_3$ is much smaller than that of BCZ80 due to the difference of ionic radii of Ca^{2+} (1.12Å) and Ba^{2+} (1.42Å). Additionally, the unit cell volume of $BaZrO_3$ is larger than that of $CaZrO_3$.

As Bennett, Grinberg et al reported, doping $BaZrO_3$ with Ca^{2+} the volume increases and at a defined Ca^{2+} to Ba^{2+} ratio the volume starts decreasing. Furthermore, the Ba^{2+} atom in the $BaZrO_3$ has a high symmetry position in the center and if Ca^{2+} is induced, a low symmetry position is formed. [77]

The result of the dielectric measurement at different frequencies for $Ba_{0.80}Ca_{0.20}ZrO_3$ are shown in Figure 69 in a temperature range from -50°C to 300°C.

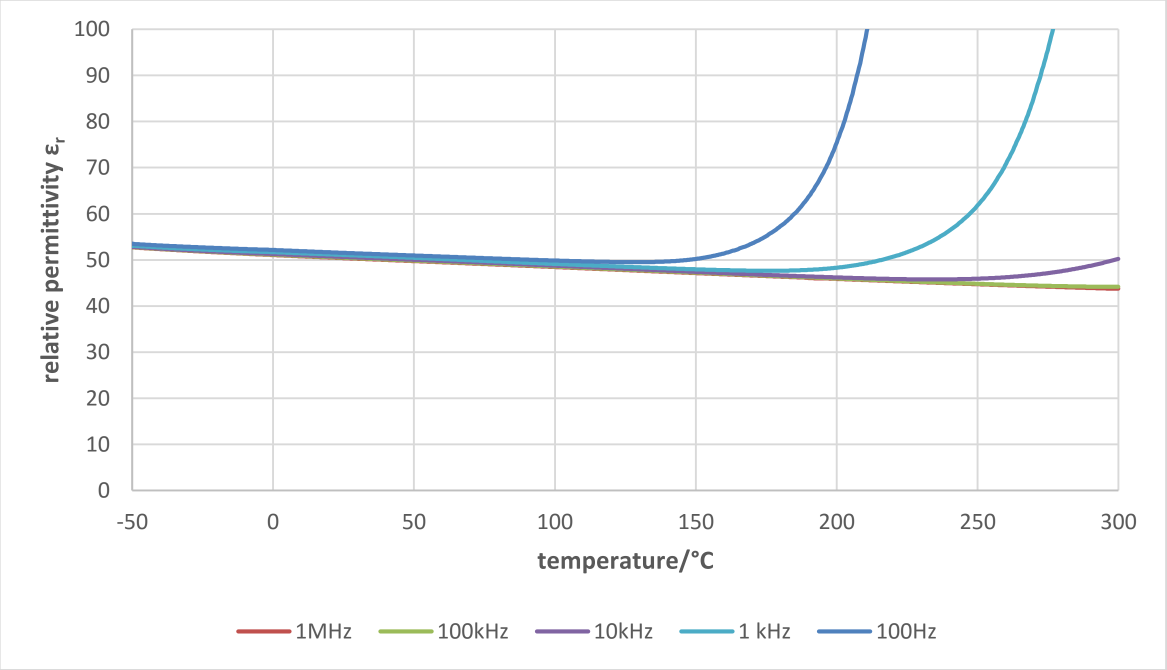

Figure 69: Variation of the relative permittivity for different temperatures for BCZ80 ceramic sintered at 1400°C for 4 hours.

---

[1] Relative permittivity from our work

In contrast to the other ceramics, the relative permittivity decreases to 53. It can be assumed that the BCZ80 gets lossy in the region above 150°C, which is also supported by the temperature dependence of the loss factor shown in Figure 70. In such samples no features are revealed due to the titling phase transition. That behaviors may occur because of heterogeneities in the sample. It can be noted that the solubility of Ba^{2+} in $CaZrO_3$ is limited and the solubility of Ca^{2+} in $BaZrO_3$ goes on faster. [53]

The dielectric losses versus temperature are shown in Figure 70 at constant frequencies (1MHz, 100kHz, 10kHz, 1kHz and 100Hz). The maximum temperature is shifted to higher temperatures while the frequency increases. At 100 Hz a temperature maxiumum of 225°C is shown which is due to the transition from the cubic to tetragonal phase with octahedral tilting transition as Levin, Amos et al reported.[53] With increasing frequency to 1 kHz the maximum is shifted to 273°C.

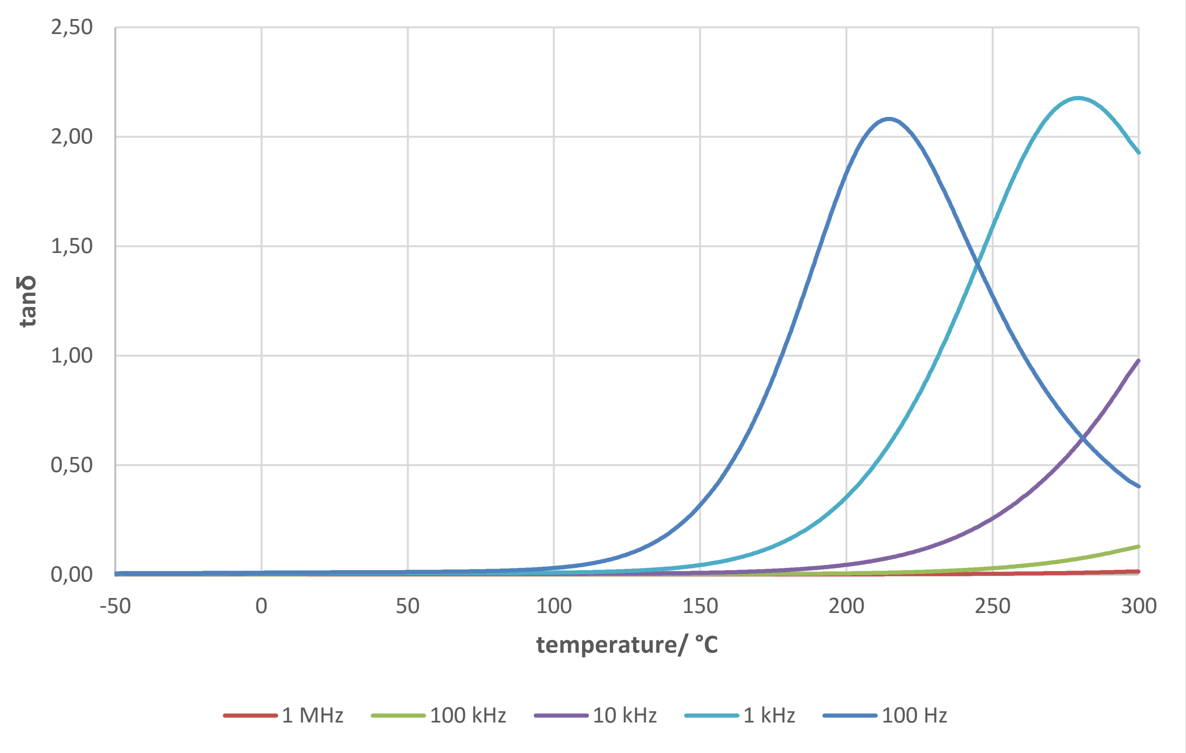

Figure 70: Dielectric losses for BCZ80 with different frequencies from -50°C to 300°C.

5 Conclusion

The Ba(Zr_xTi_{1-x})O_3 ceramics with x=0.20 and x=0.25 were prepared successfully via mixed oxide route. Their structure, densities, shrinkage and dielectric properties have been studied. It was found that BZT80 and BZT75 ceramics have been fully reacted at 1007.1°C and 1008.2°C. The decomposition of $BaCO_3$ is going on in two steps which is shown with simultaneous theromanalysis coupled with mass spectrometry (TG/DSC-MS). Both calcined (1250°C) and sintered (1400°C) samples of BZT80 and BZT75 possess a single phase perovskite structure with no impurities. The samples can be sintered to more than 85% of the theoretical density at 1400°C which is a quite good compared to literature reports 39. [40]

With increasing Zr^{4+} content the XRD peaks are shifted to lower angles with indicates an increase in cell volume due to the larger radius of Zr^{4+} compared to Ti^{4+}. Both ceramics show a tetragonal structure after sintering at 1400°C for 4 hours.

Additionally, the high temperature XRD reveals the formation reaction of the BZT80 ceramic. It can be noticed that the intermediate phase Ba_2TiO_4 is formed which is observed between 950°C and 1150°C. Also a transition of unreacted $BaCO_3$ from orthorhombic phase to trigonal phase is taking place at 850°C. At 1200°C a BZT with perovskite structure is formed with a small amount of $BaZrO_3$ as impurity phase.

To sum up, the $BaCO_3$ reacts first with the more acidic Ti^{4+} to $BaTiO_3$. Subsequently the secondary phase reacts with ZrO_2 to form Ba(Zr,Ti)O_3. Two perovskite phases are formed with different Zr/Ti ratio (BZT and $BaZrO_3$).

The dielectric constant decreases with increasing zirconium content. The loss factor of BZT75 and BZT80 between -50°C and 165°C is lower than 3%.

Furthermore, the temperature maximum T_m is shifted to higher temperatures with increasing frequency and the relative permittivity is decreasing with increasing frequency. As seen in Figure 40 and Figure 41 this effect is only seen for BZT75. It is known as the ferroelectric relaxor behavior. The diffuseness constant increases with the Zr^{4+} content which confirms the relaxor behavior of BZT75. The lower diffuseness constant of BZT80 also indicates a relaxor behavior.

The (Ba_xCa_{1-x}),($Zr_{0.20}Ti_{0.80}$)O_3 ceramics with x=0.80 and x=0.94 are prepared via mixed oxide route.

As seen in the TG/DSC-MS the reaction for BCZT80 finishes at 1011.1°C with 10 K/min. The decomposition of $BaCO_3$ is going on in two steps, The BCZT94 ceramic has reacted faster which results in a smaller mass loss. To sum up the mass loss is getting smaller with decreasing Ca^{2+} content.

These powders can be sintered at 1400°C with a sinter density between 91% and 95% of the theoretical density.

The calcined powder shows a perovskite structure with $BaZrO_3$ and $CaTiO_3$ as impurity phase. Furthermore, the sintered powder shows two perovskite structures, the one of the BCZT80 ceramic and the other of $CaTiO_3$. Including a lower Ca^{2+} content a small amount of unreacted $BaZrO_3$ is observed but no $CaTiO_3$ as seen in the BCZT80 ceramic.

Additionally, it can be assumed that Ca^{2+} and Zr^{4+} diffuse into the $BaTiO_3$ lattice and with increasing Ba^{2+} content the cell volume decreases from 65.98Å^3 to 65.64Å^3. The XRD pattern shows that the BCZT80 ceramic has a pseudocubic structure whereas the BCZT94 ceramic has a tetragonal structure.

The high temperature XRD shows the forming reaction of BCZT80 through the secondary phases of $CaZr_4O_9$, Ba_2ZrO_4 and $Ba_3Ca_2Ti_2O_9$. Also the reaction to $CaTiO_3$, $BaTiO_3$, $CaZrO_3$ and $BaZrO_3$ are identified as side reaction.

The $BaCO_3$ undergoes a formation from orthorhombic to trigonal phase at 850°C as well as in the BZT ceramic.

At 1200°C the perovskite structure of $Ba(Zr,Ti)O_3$ and $CaTiO_3$ have been formed and not that of BCZT. The $Ba(Zr,Ti)O_3$ and the $BaZrO_3$ transform at higher temperatures in the (110) BCZT which form the single phase component.

The Ba^{2+} content increases and also the relative permittivity is getting higher. In comparison to the BZT80 ceramic the phase transition temperature decreases and the broadness of the peak increases significantly.

These ceramics show a ferroelectric relaxor behavior with a diffuseness constant of 1.93 (BCZT80) and 1.88 (BCZT94).

Finally, the $Ba_{0.80}Ca_{0.20}ZrO_3$ ceramic was prepared. The thermoanalysis show that the reaction ends at 1169.3°C within a mass loss of CO_2 in two steps. In comparison with BCZT one can see that the second step of the decomposition of carbonates is shifted to higher temperatures. The sample was sintered at 1400°C achieving 92% of theoretical density. The sintered sample shows two perovskite structures with different Ba/Ca ratio. The tetragonal structure is obtained from the XRD pattern at room temperature.

Additionally, the high temperature XRD shows the forming reaction through the side reaction of $CaZr_4O_9$ to $CaZrO_3$ and $BaZrO_3$. It has to be noticed that $BaCO_3$ undergoes a phase formation from orthorhombic to trigonal phase at 850°C and furthermore at 1000°C a formation from trigonal to cubic phase. At 1100°C the amount of initial components $BaCO_3$ and ZrO_2 has been fully reacted to the products. As already mentioned, a Ba^{2+} rich and a Ca^{2+} rich zirconate is formed at 1200°C.

In contrast to the other ceramics the BCZ80 ceramic shows a relative permittivity of only 53, which is higher than that of $BaZrO_3$ and $CaZrO_3$. The Ba^{2+} atom in the $BaZrO_3$ has a high symmetry position in the center and if Ca^{2+} is induced, a low symmetry position is formed. Furthermore, Ca^{2+} doped $BaZrO_3$ shows an increasing volume and at a defined Ca^{2+} to Ba^{2+} ratio the volume starts declining.

To sum up, this work illustrates the complexity of the forming reactions and provides the basis for the development of ferroelectric relaxors with high permittivity.

List of Figures

List of Tables

List of Equations

List of Abbreviation

TG/DSC-MS[2]	Thermogravimetry/Differential Scanning Calorimetrie - Mass Spectrometry
STA-MS[2]	Simultaneous thermoanalysis – Mass Spectrometry
XRD.	X-ray diffraction
HT-XRD	High temperature X-ray diffraction
ICSD	Inorganic Crystal Structure Database
BZT80	$BaZr_{0.20}Ti_{0.80}O_3$
BZT75	$BaZr_{0.25}Ti_{0.75}O_3$
BZT45	$BaZr_{0.55}Ti_{0.45}O_3$
BCZT80	$Ba_{0.80}Ca_{0.20}Zr_{0.20}Ti_{0.80}O_3$
BCZT94	$Ba_{0.94}Ca_{0.06}Zr_{0.20}Ti_{0.80}O_3$
BCZ80	$Ba_{0.80}Ca_{0.20}ZrO_3$
MID	multiple ion detector
MPB	morphotropic phase boundary
MLCC	Mulilayer ceramic capacitor
PMN	$Pb(Mg_{1/3}Nb_{2/3})O_3$
PTC	Positive temperature coefficient transducers

---

[2] TG/DSC-MS = STA-MS

References

(1) Badapanda, T.; Rout, S. K.; Cavalcante, L. S.; Sczancoski, J. C.; Panigrahi, S.; Longo, E.; Li, M. S. Optical and dielectric relaxor behaviour of Ba(Zr 0.25 Ti 0.75)O 3 ceramic explained by means of distorted clusters, *J. Phys. D: Appl. Phys.* **2009**, *42,* p. 175414.

(2) Gene H.Haertling Ferroelectric Ceramics: History and Technology, *J American Ceramic Society.* **1999,** pp. 797–818.

(3) Cai, W.; FU, C.; GAO, J.; Chen, H. Effects of grain size on domain structure and ferroelectric properties of barium zirconate titanate ceramics, *Journal of Alloys and Compounds.* **2009**, *480,* pp. 870–873.

(4) Takenaka, T.; Nagata, H. Current status and prospects of lead-free piezoelectric ceramics, *Journal of the European Ceramic Society.* **2005**, *25,* pp. 2693–2700.

(5) Puli, V. S.; Pradhan, D. K.; Chrisey, D. B.; Tomozawa, M.; Sharma, G. L.; Scott, J. F.; Katiyar, R. S. Structure, dielectric, ferroelectric, and energy density properties of (1 − x)BZT–xBCT ceramic capacitors for energy storage applications, *J Mater Sci.* **2013**, *48,* pp. 2151–2157.

(6) J. Bera and S.K. Rout On The Formation Of BaTiO3- BaZrO3 Solid Solution Through Solid-Oxide Reaction, *Materials Letters.* **2004,** pp. 135–138.

(7) Shrout, T. R.; Zhang, S. J. Lead-free piezoelectric ceramics. Alternatives for PZT?, *J Electroceram.* **2007**, *19,* pp. 113–126.

(8) Rainer Waser, Ulrich Böttger, Stephan Tiedke, Ed. *Polar Oxides: Properties, Characterization, and Imaging*.

(9) Moore,Elaine_A.Smart,Lesley, Ed. *Solid state chemistry;* Taylor & Francis Group: New York, 2012.

(10) Wenwu Cao and L. E. Cross Theory of tetragonal twin structures in ferroelectric perovskites with a first-order phase transition.

(11) M. Johnsonn, P. L. Crystallography and Chemistry of Perovskites, *Journal of Physics: Condensed Matter.* **2008,** pp. 1–6.

(12) Schaumburg, H., Ed. *Werkstoffe und Bauelemente der Elektrotechnik (5th ed.);* Hamburg-Hamburg: Stuttgard, 1994.

(13) Neil W. Ashcroft, N.David Mermin, Ed. *The Drude Theory of Metals,* 1976.

(14) C.Kittel, Ed. *Introduction to Solid State Physics;* Wiley, New York, 1996.

(15) M.E.Lines and A.M.Glass, Ed. *Principles and Applications of Ferroelectrics and Related Materials;* Oxford Scholar Ship: Oxford, 2001.

(16) C.A. Randall, R.E. Newnham, L.E. Cross History of the First Ferroelectric Oxide, BaTiO3.

(17) H.Thurnaurer and J.Deaderick A Short History of Ferroelectricity. **1947**.

(18) B.M. Vul and J.M. Goldmann Dielectric Constants of Titanates of Metals of the Second Group, *Compt. Rend.Acad. Sci. U.S.S.R.* **1945,** pp. 139–142.

(19) H.D.Megaw Crystal Structure of Barium Titanate, *Nature.* **1945,** p. 155.

(20) A. von Hippel Ferroelectricity, Domain Structures, and Phase Transitions of Barium Titanate, *Revs. Mod. Phys.* **1950,** pp. 221–237.

(21) H. F. Kay and P. Vousden Symmetry Changes in Barium Titanate at Low Temperatures and Their Relation to Its Ferroelectric Properties, *Philosophical Magazine.* **1949,** pp. 1019–1040.

(22) Yu, Z.; Ang, C.; Guo, R.; Bhalla, A. S. Piezoelectric and strain properties of Ba(Ti[sub 1−x]Zr[sub x])O[sub 3] ceramics, *J. Appl. Phys.* **2002**, *92,* p. 1489.

(23) Pandey, R. K., Ed. *Proceedings of the Ninth IEEE International Symposium on Applications of Ferroelectrics. University Park, Pennsylvania, USA, August 7 - August 10, 1994;* IEEE Service Center: Piscataway, NJ, 1994.

(24) A.J. Moulson, J. H., Ed. *Electroceramics 2nd Edition,* 2003.

(25) Rigoberto López-Juárez, Federico González and María-Elena Villafuerte-Castrejón Lead-Free Ferroelectric Ceramics with Perovskite Structure.

(26) Cheong, S.-W.; Mostovoy, M. Multiferroics: a magnetic twist for ferroelectricity, *Nature materials.* **2007**, *6,* pp. 13–20.

(27) Jin, L.; Li, F.; Zhang, S.; Green, D. J. Decoding the Fingerprint of Ferroelectric Loops. Comprehension of the Material Properties and Structures, *J. Am. Ceram. Soc.* **2014**, *97,* pp. 1–27.

(28) Stemmer, S.; Streiffer, S. K.; Ernst, F.; Rüuhle, M. Atomistic structure of 90° domain walls in ferroelectric PbTiO 3 thin films, *Philosophical Magazine A.* **1995**, *71,* pp. 713–724.

(29) Isupov, V. A.; Pronin, I. P.; Sizykh, V. I. Investigation of the diffuse ferroelectric phase transition in leadmagnesium niobate, *Ferroelectrics.* **1989**, *90,* pp. 147–150.

(30) Xu, Y. *Ferroelectric materials and their applications;* North-Holland; Sole distributors for the USA and Canada, Elsevier Science Pub. Co: Amsterdam, New York, New York, NY, USA, 1991.

(31) Spanier, J. E.; Kolpak, A. M.; Urban, J. J.; Grinberg, I.; Ouyang, L.; Yun, W. S.; Rappe, A. M.; Park, H. Ferroelectric phase transition in individual single-crystalline BaTiO3 nanowires, *Nano letters.* **2006**, *6,* pp. 735–739.

(32) Ishikawa, K.; Yoshikawa, K.; Okada, N. Size effect on the ferroelectric phase transition in PbTiO3 ultrafine particles, *Phys. Rev. B.* **1988**, *37,* pp. 5852–5855.

(33) Dragan Damjanovic Ferroelectric, dielectric and piezoelectric properties of ferroelectric thin films and ceramics, *Rep. Prog. Phys.* **1998,** pp. 1267–1324.

(34) G.A.Smolenskii, *J. Phys. Soc. Jpn.* **1970,** p. 26.

(35) Bing, Y.-H.; Bokov, A. A.; Ye, Z.-G. Diffuse and sharp ferroelectric phase transitions in relaxors, *Current Applied Physics.* **2011**, *11,* S14-S21.

(36) Setter, N.; Cross, L. E. The role of B-site cation disorder in diffuse phase transition behavior of perovskite ferroelectrics, *J. Appl. Phys.* **1980**, *51,* p. 4356.

(37) Fundora, A.; Vázquez, A.; Portelles, J.; Calderón, F.; Siqueiros, J. M. Diffuse phase transitions in ferroelectric ceramics, *Journal of Non-Crystalline Solids.* **1998**, *235-237,* pp. 567–569.

(38) CHOI, Y. K.; HOSHINA, T.; TAKEDA, H.; TSURUMI, T. Effects of Ca and Zr additions and stoichiometry on the electrical properties of barium titanate-based ceramics, *J. Ceram. Soc. Japan.* **2010**, *118,* pp. 881–886.

(39) Bokov, A. A.; Ye, Z.-G. Recent progress in relaxor ferroelectrics with perovskite structure, *J Mater Sci.* **2006**, *41,* pp. 31–52.

(40) Benabdallah, F.; Simon, A.; Khemakhem, H.; Elissalde, C.; Maglione, M. Linking large piezoelectric coefficients to highly flexible polarization of lead free BaTiO3-CaTiO3-BaZrO3 ceramics, *J. Appl. Phys.* **2011**, *109,* p. 124116.

(41) Suslov, A. N.; Durilin, D. A.; Ovchar, O. V.; Belous, A. G.; Jancar, B.; Spreitzer, M. Synthesis and dielectric and nonlinear properties of BaTi1 − x Zr x O3 ceramics, *Inorg Mater.* **2014**, *50,* pp. 1125–1130.

(42) Zhang, L.; Wang, X.; Yang, W.; Liu, H.; Yao, X. Structure and relaxor behavior of BaTiO[sub 3]–CaTiO[sub 3]–SrTiO[sub 3] ternary system ceramics, *J. Appl. Phys.* **2008**, *104,* p. 14104.

(43) Hirota, K.; Wakimoto, S.; E. Cox, D. Neutron and X-ray Scattering Studies of Relaxors, *J. Phys. Soc. Jpn.* **2006**, *75,* p. 111006.

(44) V. Westphal; W. Kleemann; and M. D. Glinchuk Diffuse phase transitions and random-field-induced domain states of the "relaxor" ferroelectric PbMg_{1/3}Nb_{2/3}O_{3}.

(45) Yoseph Imry and Shang-keng Ma Random-Field Instability of the Ordered State of Continuous Symmetry.

(46) M D Glinchuk and R Farhi A random field theory based model for ferroelectric relaxors, *J. Phys. Condens. Matter.* **1996,** pp. 6985–6996.

(47) Egami, T. Atomistic Mechanism of Relaxor Ferroelectricity, *Ferroelectrics.* **2002**, *267,* pp. 101–111.

(48) Hennings, D. F. K.; Schreinemacher, B. S.; Schreinemacher, H. Solid-State Preparation of BaTiO 3 -Based Dielectrics, Using Ultrafine Raw Materials, *Journal of the American Ceramic Society.* **2001**, *84,* pp. 2777–2782.

(49) Beauger, A.; Mutin, J. C.; Niepce, J. C. Synthesis reaction of metatitanate BaTiO3, *J Mater Sci.* **1983**, *18,* pp. 3543–3550.

(50) Carter, R. E. Kinetic Model for Solid-State Reactions, *J. Chem. Phys.* **1961**, *34,* p. 2010.

(51) Materials Production and Processing - Ceramics. https://online.tugraz.at/tug_online/LV_TX.wbLvInfoTypen?pStpSpNr=192215. Monday, August 1, 2016.

(52) lee, s. i., Ed. *DEFECT-PHASE EQUILIBRIUM AND FERROELECTRIC PHASE TRANSITION BEHAVIOR IN NON-STOICHIOMETRIC BaTiO3 UNDER VARIOUS EQUILIBRIUM CONDITIONS,* 2006.

(53) Levin, I.; Amos, T. G.; Bell, S. M.; Farber, L.; Vanderah, T. A.; Roth, R. S.; Toby, B. H. Phase equilibria, crystal structures, and dielectric anomaly in the BaZrO3–CaZrO3 system, *Journal of Solid State Chemistry.* **2003**, *175,* pp. 170–181.

(54) Maiti, T.; Guo, R.; Bhalla, A. S. Structure-Property Phase Diagram of BaZr x Ti 1−x O 3 System, *J American Ceramic Society.* **2008**, *91,* pp. 1769–1780.

(55) Yu, Z.; Guo, R.; Bhalla, A. S. Dielectric behavior of Ba(Ti[sub 1−x]Zr[sub x])O[sub 3] single crystals, *J. Appl. Phys.* **2000**, *88,* p. 410.

(56) C. Vasilescu, L.P. Curecheriu, L. Mitoseriu PHASE FORMATION, MICROSTRUCTURE AND FUNCTIONAL PROPERTIES OF SOME BZT CERAMICS, *U.P.B. Sci. Bull.* **2015**.

(57) Tang, X. G.; Chew, K.-H.; Chan, H. Diffuse phase transition and dielectric tunability of Ba(ZryTi1−y)O3 relaxor ferroelectric ceramics, *Acta Materialia.* **2004**, *52,* pp. 5177–5183.

(58) Rehrig, P. W.; Park, S.-E.; Trolier-McKinstry, S.; Messing, G. L.; Jones, B.; Shrout, T. R. Piezoelectric properties of zirconium-doped barium titanate single crystals grown by templated grain growth, *J. Appl. Phys.* **1999**, *86,* p. 1657.

(59) Dobal, P. S.; Dixit, A.; Katiyar, R. S.; Yu, Z.; Guo, R.; Bhalla, A. S. Micro-Raman scattering and dielectric investigations of phase transition behavior in the BaTiO[sub 3]–BaZrO[sub 3] system, *J. Appl. Phys.* **2001**, *89,* p. 8085.

(60) Yang, L.-J.; Wu, L.-Z.; Dong, S. First-principles study of the relaxor ferroelectricity of Ba(Zr, Ti)O 3, *Chinese Phys. B.* **2015**, *24,* p. 127702.

(61) Ciomaga, C.; Viviani, M.; Buscaglia, M. T.; Buscaglia, V.; Mitoseriu, L.; Stancu, A.; Nanni, P. Preparation and characterisation of the Ba(Zr,Ti)O3 ceramics with relaxor properties, *Journal of the European Ceramic Society.* **2007**, *27,* pp. 4061–4064.

(62) Dong, L.; Stone, D. S.; Lakes, R. S. Enhanced dielectric and piezoelectric properties of xBaZrO3-(1−x)BaTiO3 ceramics, *J. Appl. Phys.* **2012**, *111,* p. 84107.

(63) Moura, F.; Simões, A. Z.; Stojanovic, B. D.; Zaghete, M. A.; Longo, E.; Varela, J. A. Dielectric and ferroelectric characteristics of barium zirconate titanate ceramics prepared from mixed oxide method, *Journal of Alloys and Compounds.* **2008**, *462,* pp. 129–134.

(64) Bernardi, M. I. B.; Antonelli, E.; Lourenço, A. B.; Feitosa, C. A. C.; Maia, L. J. Q.; Hernandes, A. C. BaTi1–xZrxO3 nanopowders prepared by the modified Pechini method, *J Therm Anal Calorim.* **2007**, *87,* pp. 725–730.

(65) Jain, T. A.; Fung, K. Z.; Chan, J. Effect of the A/B ratio on the microstructures and electrical properties of (Ba0.95±xCa0.05)(Ti0.82Zr0.18)O3 for multilayer ceramic capacitors with nickel electrodes, *Journal of Alloys and Compounds.* **2009**, *468,* pp. 370–374.

(66) Liu, W.; Ren, X. Large piezoelectric effect in Pb-free ceramics, *Physical review letters.* **2009**, *103,* p. 257602.

(67) Keeble, D. S.; Benabdallah, F.; Thomas, P. A.; Maglione, M.; Kreisel, J. Revised structural phase diagram of (Ba0.7Ca0.3TiO3)-(BaZr0.2Ti0.8O3), *Appl. Phys. Lett.* **2013**, *102,* p. 92903.

(68) Xue, D.; Zhou, Y.; Bao, H.; Zhou, C.; Gao, J.; Ren, X. Elastic, piezoelectric, and dielectric properties of Ba(Zr0.2Ti0.8)O3-50(Ba0.7Ca0.3)TiO3 Pb-free ceramic at the morphotropic phase boundary, *J. Appl. Phys.* **2011**, *109,* p. 54110.

(69) Li, W.; Xu, Z.; Chu, R.; Fu, P.; Zang, G. Polymorphic phase transition and piezoelectric properties of (Ba1−xCax)(Ti0.9Zr0.1)O3 lead-free ceramics, *Physica B: Condensed Matter.* **2010**, *405,* pp. 4513–4516.

(70) Zhang, S.-W.; Zhang, H.; Zhang, B.-P.; Yang, S. Phase-transition behavior and piezoelectric properties of lead-free (Ba0.95Ca0.05)(Ti1−xZrx)O3 ceramics, *Journal of Alloys and Compounds.* **2010**, *506,* pp. 131–135.

(71) Hiroshi Kishi; Youichi Mizuno and Hirokazu Chazono Base-Metal Electrode-Multilayer Ceramic Capacitors: Past, Present and Future Perspectives.

(72) Moura, F.; Simões, A. Z.; Stojanovic, B. D.; Zaghete, M. A.; Longo, E.; Varela, J. A. Dielectric and ferroelectric characteristics of barium zirconate titanate ceramics prepared from mixed oxide method, *Journal of Alloys and Compounds.* **2008**, *462,* pp. 129–134.

(73) Chen, H.; Yang, C.; FU, C.; Shi, J.; Zhang, J.; Leng, W. Microstructure and dielectric properties of BaZr x Ti1−x O3 ceramics, *J Mater Sci: Mater Electron.* **2008**, *19,* pp. 379–382.

(74) Chen, H.; Yang, C.; FU, C.; Shi, J.; Zhang, J.; Leng, W. Microstructure and dielectric properties of BaZr x Ti1−x O3 ceramics, *J Mater Sci: Mater Electron.* **2008**, *19,* pp. 379–382.

(75) Frattini, A.; Di Loreto, A.; Sanctis, O. de; Benavidez, E. BCZT Ceramics Prepared from Activated Powders, *Procedia Materials Science.* **2012**, *1,* pp. 359–365.

(76) Ravez, J.; Broustera, C.; Simon, A. Lead-free ferroelectric relaxor ceramics in the BaTiO3-BaZrO3-CaTiO3 system, *J. Mater. Chem.* **1999**, *9,* pp. 1609–1613.

(77) Bennett, J. W.; Grinberg, I.; Rappe, A. M. Nonmonotonic Composition Dependence of the Dielectric Response of Ba 1− x Ca x ZrO 3, *Chem. Mater.* **2008**, *20,* pp. 5134–5138.